UNIVERSIDADE ESTADUAL DE CAMPINAS
Faculdade de Engenharia Mecânica

GIÁCOMO ANTONIO DOLLEVEDO

Design and construction of an improved closed-loop Interferometric Fiber Optic Gyroscope

Projeto e construção de um giroscópio interferométrico de fibra óptica de malha-fechada melhorado

Campinas

2023

GIÁCOMO ANTONIO DOLLEVEDO

Design and construction of an improved closed-loop Interferometric Fiber Optic Gyroscope

Projeto e construção de um giroscópio interferométrico de fibra óptica de malha-fechada melhorado

Dissertação de Mestrado Acadêmico apresentada à Faculdade de Engenharia Mecânica da Universidade Estadual de Campinas como parte dos requisitos exigidos para a obtenção do título de Mestre em Engenharia Mecânica, na Área de Mecatrônica

Orientador: Prof. Dr. Rodrigo Moreira Bacurau

Coorientador: Prof. Dr. Alex Dante

ESTE TRABALHO CORRESPONDE À VERSÃO FINAL DA DISSERTAÇÃO DE MESTRADO ACADÊMICO DEFENDIDA PELO ALUNO GIÁCOMO ANTONIO DOLLEVEDO, E ORIENTADA PELO PROF. DR. RODRIGO MOREIRA BACURAU.

Campinas

2023

Ficha catalográfica
Universidade Estadual de Campinas
Biblioteca da Área de Engenharia e Arquitetura
Rose Meire da Silva - CRB 8/5974

D691d

Dollevedo, Giácomo Antonio, 1997-
Design and construction of an improved closed-loop interferometric fiber optic gyroscope / Giácomo Antonio Dollevedo. – Campinas, SP : [s.n.], 2023.

Orientador: Rodrigo Moreira Bacurau.
Coorientador: Alex Dante.
Dissertação (mestrado) – Universidade Estadual de Campinas, Faculdade de Engenharia Mecânica.

1. Giroscópio. 2. Eletrônica. 3. Ruído. I. Bacurau, Rodrigo Moreira, 1988-. II. Dante, Alex, 1979-. III. Universidade Estadual de Campinas. Faculdade de Engenharia Mecânica. IV. Título.

<u>Informações Complementares</u>

Título em outro idioma: Projeto e construção de um giroscópio interferométrico de fibra óptica de malha-fechada melhorado
Palavras-chave em inglês:
Gyroscope
Electronics
Noise
Área de concentração: Mecatrônica
Titulação: Mestre em Engenharia Mecânica
Banca examinadora:
Rodrigo Moreira Bacurau [Orientador]
Elnatan Chagas Ferreira
Hugo Leonardo Rocha de Lira
Data de defesa: 15-12-2023
Programa de Pós-Graduação: Engenharia Mecânica

Identificação e informações acadêmicas do(a) aluno(a)
- ORCID do autor: https://orcid.org/0000-0002-5050-7016
- Currículo Lattes do autor: https://lattes.cnpq.br/3357698197385671

UNIVERSIDADE ESTADUAL DE CAMPINAS
FACULDADE DE ENGENHARIA MECÂNICA

DISSERTAÇÃO DE MESTRADO ACADÊMICO

Design and construction of an improved closed-loop Interferometric Fiber Optic Gyroscope

Projeto e construção de um giroscópio interferométrico de fibra óptica de malha-fechada melhorado

Autor: Giácomo Antonio Dollevedo

Orientador: Prof. Dr. Rodrigo Moreira Bacurau
Coorientador: Prof. Dr. Alex Dante

A Banca Examinadora composta pelos membros abaixo aprovou esta Dissertação:

Prof. Dr. Rodrigo Moreira Bacurau
DMC / FEM / UNICAMP

Prof. Dr. Elnatan Chagas Ferreira
FEEC / UNICAMP

Dr. Hugo Leonardo Rocha de Lira
DCTA / IEAv

A Ata de Defesa com as respectivas assinaturas dos membros encontra-se no SIGA/Sistema de Fluxo de Dissertação/Tese e na Secretaria do Programa da Unidade.

Campinas, 15 de Dezembro de 2023

AGRADECIMENTOS

Nunca fui bom com palavras, muito menos quando preciso delas para expressar sentimentos, e talvez uma das tarefas mais difíceis deste trabalho seja agradecer de maneira justa a todos aqueles que, de alguma forma, contribuíram tanto para sua realização, quanto para minha formação (pessoal e acadêmica). Por isso, digo ser inevitável que eu não esqueça alguns nomes, o que não quer dizer que eu não tenha algo a lhes agradecer.

Primeiramente, começo agradecendo minha família por sempre ter me oferecido apoio incondicional, motivação, e condições para que a minha educação fosse a melhor possível. Meus pais, Stefano e Celi, e meu irmão, Teo, são a base de quem eu sou, e o amor e gratidão que tenho por vocês é eterno.

Agradeço aos meus amigos de infância, que hoje também os considero como família, Mereb, Rods, Henrique, Luiz e Giovanni. Ter o companheirismo de vocês é muito mais do que eu poderia sonhar. Saibam que me espelho em cada um de vocês.

Ao meu amigo Gustavo Fernandes, por todos os momentos que vivenciamos nesta faculdade durante o periodo de graduação. Todas as discussões, caronas, festas, alegrias e desesperos compartilhados fizeram deste período uma experiência muito mais completa e brilhante do que eu esperava.

Aos colegas de laboratório que tive a breve e, mesmo assim, grande oportunidade de compartilhar experiências durante estes dois anos de mestrado. O suporte e as discussões com os colegas do DEMIC e do GD3, somado ao inestimável valor das pausas para café, também foram fundamentais para mim. Bacurau, Dannylo, Luan, Erick, Matheus, Kenji, Leozão, Lucas e Fernando, vocês todos foram parte da minha jornada, e gostaria de ter tido mais tempo para compartilhar com vocês.

Bacurau, desde o primeiro momento em que você começou a me orientar, num simples trabalho de conclusão de curso, obrigado por sempre me incentivar a ser o melhor eu possível. Obrigado pela paciência, orientação e amizade durante todos esses anos. Você é responsável por uma enorme parte do meu desenvolvimento profissional e pessoal. Você é um exemplo pra mim, conversar e trabalhar com você foi um dos grandes privilégios do meu tempo na UNICAMP.

Aos colegas do IEAv, obrigado por estarem sempre presentes e por todo suporte durante o projeto. Nossas reuniões e discussões semanais foram, sem dúvidas, parte importante da minha formação.

Aos membros da banca examinadora: Dr. Elnatan Chagas e Dr. Hugo Lira, agradeço a disponibilidade e suas valiosas contribuições ao projeto.

Por último, mas não menos importante, gostaria de agradecer ao pessoal que me aguentou por todos os dias nesses dois últimos anos: Lucas, Kairé, Guilherme, Giovanni e Lucas (novo), obrigado pela convivência e apoio, pelas risadas, pelos lanches, pizzas e conversas aleatórias de madrugada.

O presente trabalho foi realizado com apoio da Coordenação de Aperfeiçoamento de Pessoal de Nível Superior – Brasil (CAPES) – Código de Financiamento 001.

E pur si muove! (Galileo Galilei)

RESUMO

Giroscópios interferométricos a fibra óptica (IFOGs) são componentes fundamentais em sistemas de navegação inercial (INS) de alta performance, aplicados majoritariamente em setores militares e aeroespaciais. Em particular, a tecnologia dos IFOGs é reconhecida na literatura por ser a única que, na prática, ainda não é limitada por algum fenômeno físico, sendo assim a mais promissora dentre as disponíveis. A busca contínua por melhorias de desempenho deste tipo de sensor é imperativa e o domínio de sua fabricação é essencial, principalmente no caso do Brasil, para garantir independência em relação a tecnologia para acesso ao espaço. Dito isso, neste trabalho é apresentado um projeto para um novo sistema embarcado para IFOGs, o qual tem capacidade de permitir o monitoramento de múltiplos eixos, como requerido pelos INS, com flexibilidade para o uso de interferômetros menores e, consequentemente, com maiores banda e fundo de escala. Este novo projeto apresentou um ARW de $7,0 \cdot 10^{-4}\ ^{\circ}/\sqrt{\mathrm{h}}$. Também é discutido neste trabalho uma nova abordagem para minimizar os efeitos da *modulação de intensidade* dos moduladores baseados em $LiNbO_3$ (MIOC) em IFOGs de malha fechada. Um método de auto-calibração e compensação por software deste fenômeno através do próprio sistema embarcado é proposto e validado via simulação. Também é contribuição deste trabalho a melhoria de uma modelagem teórica de ruído, que permite a avaliação do ARW (*angle random walk*) de IFOGs com modulação digital. Este modelo é validado experimentalmente em relação aos principais contribuintes de ruído eletrônico e óptico no sistema de aquisição, comparando seus valores de densidade espectral de ruído absoluto medidos com os calculados teoricamente. Também é apresentada uma investigação sobre a contribuição do ruído eletrônico do sistema de modulação. Este modelo de ruído é uma ferramenta necessária para a identificação de gargalos do sistema, servindo de base para futuras melhorias no projeto de IFOGs.

Palavras–chave: Giroscópio, Eletrônica, IFOG, Ruído, Modulação de Intensidade, MIOC

ABSTRACT

Interferometric Fiber Optic Gyroscopes (IFOGs) are key components in high-performance inertial navigation systems (INS), mostly applied in military and aerospace sectors. In particular, the IFOG technology is recognized in the literature for being the only one that, in practice, is not yet limited by some physical phenomenon, thus being the most promising among the others available. The continuous pursuit for performance improvements of this type of sensor is imperative and mastery of its manufacture is essential, especially in the case of Brazil, to guarantee independence in relation to technology for access to space. In this context, this work presents a project for a new embedded system for IFOGs, which is capable of allowing multi-axis monitoring, as required by INS, with flexibility that allows for smaller interferometer assessment and, consequently, higher bandwidth and full-scale range. This new design achieved an ARW of $7.0 \cdot 10^{-4}\ ^{\circ}/\sqrt{\mathrm{h}}$. This work also discusses a new approach to minimize the *intensity modulation* effects $LiNbO_3$ based phase modulators (MIOC) over closed-loop IFOGs. A self-calibration and software compensation of this phenomenon through the available embedded system is proposed and validated via simulation. This work also contributes to the improvement of theoretical noise modeling, which allows the evaluation of the ARW (angle random walk) of IFOGs with digital modulation. This model is experimentally validated with respect to the major electronic and optical noise contributors in the acquisition system by comparing their measured absolute noise spectral density values with the theoretically computed ones. It also presents an investigation of the modulation system's electronic noise contribution. This noise model is a mandatory tool for a better understanding of system bottlenecks, supporting future IFOG design improvements.

Keywords: Gyroscope, Electronics, IFOG, Noise, Intensity Modulation, MIOC

LIST OF FIGURES

LIST OF TABLES

LIST OF ABBREVIATIONS AND ACRONYMS

ADC	Analog-to-Digital Converter
ARW	Angle Random Walk
CS	Chip Select
CCW	Counterclockwise
CW	Clockwise
DAC	Digital-to-Analog Converter
DDS	Direct Digital Synthesizer
IEAv	Institute of Advanced Studies
IFOG	Interferometric Fiber Optic Gyroscope
IMU	Inertial Measurement Unit
INS	Inertial Navigation System
MIOC	Multi-Functional Integrated Optical Chip
RAM	Residual Amplitude Modulation
RIM	Residual Intensity Modulation
RIN	Relative Intensity Noise
PCB	Printed Circuit Board
PWM	Pulse Width Modulation
PZT	PbZxTi1-xO3 (lead zirconate titanate)
SLED	Superluminescent Diode
SNR	Signal-to-noise ratio
SPI	Serial Peripheral Interface

TIA	Transimpedance Amplifier
UNICAMP	Universidade Estadual de Campinas

CONTENTS

1 INTRODUCTION

In this chapter, we will present an introduction to navigation and orientation importance, and the role of interferometric fiber optic gyroscope sensors in high-end applications. Following, we present the efforts of our research group in contributing towards this kind of sensor development and performance improvements. Lastly, the objectives and expected contributions of this work are presented.

1.1 Contextualization

Navigation, a fundamental aspect of human civilization, has always played a pivotal role in our ability to explore and understand the world around us. Throughout history, humanity continuously sought innovative methods to improve their navigation and orientation techniques: the Phoenicians pioneered in using astronomy to guide their routes [1], while the Vikings are credited to have unknowingly employed light polarization to navigate on cloudy weather through the use of a "sunstone" [2]. Today, scientific and technological advancements allow for more accurate and precise tools to ensure reliable navigation and orientation.

In the realm of modern navigation, there is great interest in inertial navigation systems (INS), as they offer a self-contained and reliable orientation and position estimation, meaning it does not rely on external signals, such as those originating from GPS (Global Positional System). INSs combine accelerometers and gyroscope sensors to provide accurate information about acceleration, rotation, and changes in position, being employed from low, consumer-grade, to high-end applications [3, 4]. The latter consists mostly of the military and aerospace industry, which have strict requirements for gyroscope sensors' performance, as the position is computed through mathematical integration of the rate output, making it prone to accumulate large errors [5].

Foreshadowed by the Vikings' utilization of light, the advancements in navigation technology led to a high-performing light-based sensor: the Interferometric Fiber Optic Gyroscope (IFOG). By taking advantage of the Sagnac Effect, this sensor is capable of measuring the rotational speed through the phase shift between two counter-propagating interfering light waves on an optical fiber coil. Characteristics such as being low-maintenance, compact, and resistant to mechanical impacts and vibration devices while having great durability and performance [5] have made this kind of sensor one of the main choices over other technologies for high-end applications.

Figure 1.1 shows a performance comparison between the main commercial gyroscope technologies: MEMS (Microelectromechanical systems), HRG (Hemispherical Resonant Gyro), RLG (Ring Laser Gyro), SMG (Spinning Mass Gyro) and IFOG. It is clear how IFOGs are suited for a wider range of applications while still being capable of outperforming other technologies.

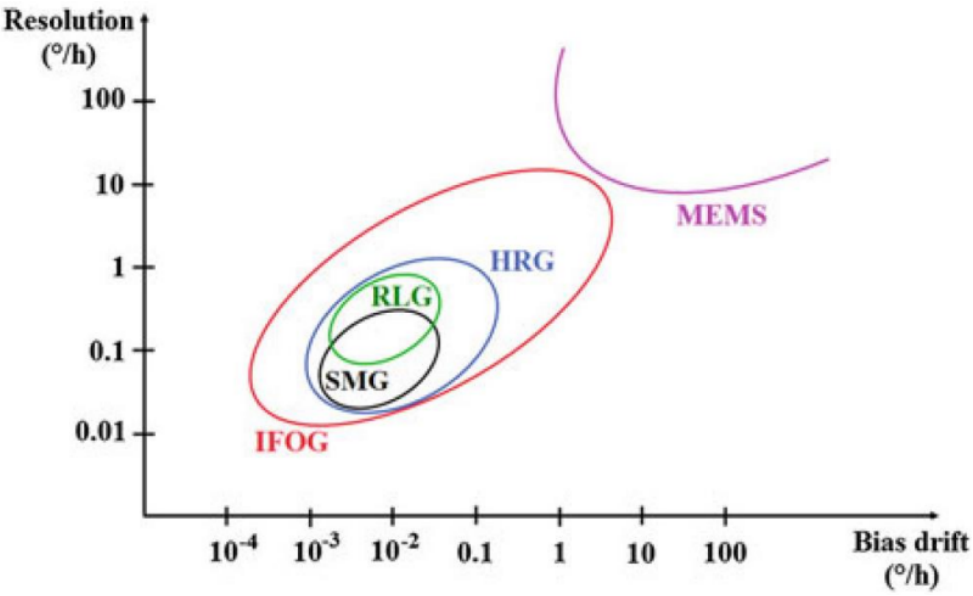

Figure 1.1 – Different gyroscope technologies performance comparison (2012). [6].

In Brazil, interferometric fiber optic gyroscopes research and development started in early 1980, within the Institute for Advanced Studies (IEAv). Later, a research group was formed along with the Aeronautics Institute of Technology (ITA), the National Institute of Space Research (INPE), and the University of Campinas (UNICAMP). The Brazilian space program has pushed the development by establishing an inertial navigation system project for aerospace applications (Project SIA) in 2006, funded by FINEP (Funding Authority for Studies and Projects) with an investment of around $R\$$ 40.000.000 ($\approx$ $R\$$ 100.000.000 for 2023 inflation-adjustment) [7], aiming to reach national independence in respect to aerospace and navigation technology. Denoting this importance, a 2009 report on Latin American space programs stated "A country that does not have independent access to space cannot pretend to the ranks of greatness" when noting Brazil's regional leadership, but ranking last place among the emerging countries group BRIC (Brazil, Russia, India, and China) [8].

University of Campinas (UNICAMP) joined this research group in 1997, and, to this date, 4 master's theses along with 3 PhD dissertations have been published [9, 10, 11, 12, 13, 14, 15]. There are contributions towards theoretical and practical IFOG implementations, that resulted in a gyroscope system with performance that matches the top sensors presented in the literature [15].

Currently, UNICAMP's research group is still contributing with IEAv members towards IFOG development, on a project named *Project IFO*. This project's final goal is to develop an Inertial Measurement Unit (IMU) that employs optical accelerometers and gyroscopes in order to provide triaxial acceleration and angular speed assessment without the need for external reference information (e.g. GPS signals). Project IFO is a five-year project that seeks to provide autonomy to Brazil in the technological and commercial field of IMUs, increasing the operating capacity of Brazilian civil and military vehicles, and space vehicles, as well as applications of interest to the areas of Defense, Military, and Space. It is also funded by FINEP with an investment of $R\$ \, 20.000.000$.

In view of the importance of dominating this kind of technology, the present work focuses on an IFOG embedded system design and application. Starting from a technical point of view, we aim to propose and design a new and updated electronic hardware project that is easier to maintain and more suitable for different applications. This design should enable multi-axis monitoring at ease, as required by modern INS systems.

In addition to technical contributions, this work also offers important scientific contributions. Firstly, it proposes a new approach to a problem known as MIOC Intensity Modulation, which has received little attention in the literature. This approach could potentially pave the way for future research in this area. Secondly, it includes improvements and experimental validation to a theoretical noise model of the IFOG, which could help with the design and optimization of future systems to achieve better performance.

Lastly, an additional goal of this dissertation is to provide an easy-to-understand, yet detailed explanation of the working principle of the system. This is important as the topic can be complex and we are aiming to reduce this complexity as it can be a barrier for future researchers in this field. Overall, there are contributions to both the technical and scientific understanding of the all-digital IFOG system and it has the potential to impact future research and development in this area.

1.2 Objectives and Contribution of the Work

The goals of this work are:

- To build a multi-axis, modular IFOG embedded system design, with improved modulation range and ability to assess smaller interferometers data;
- To study the MIOC intensity modulation and propose techniques to mitigate its effect in order to improve the sensor performance;
- To enhance the IFOG noise model with modulation circuit noise and provide experimental validation to it.

1.3 Work Structure and Organization

In view of the background, motivation, and objectives of this work, the following text is structured as follows: Chapter 2 will present the theory that leads to the IFOG design. A brief explanation of the physical phenomenon is given, followed by a description of the techniques employed in an all-digital IFOG design. Finally, a brief review of the latest developments inside our research group and of the relevant topics that are being addressed in this work is presented.

Chapter 3 discusses how the IFOG embedded system was previously implemented, along with improvements and upgrades on both electronics and board design. This chapter also highlights relevant aspects of the electronics that are used as a basis for Chapter 4 discussions.

Chapter 4 makes use of all the knowledge gathered throughout Chapters 2 and 3 to present this work's investigations and contributions to the scientific community. A new MIOC intensity modulation model, along with additions and a start on experimental validations to a gyroscope noise model are discussed.

Finally, conclusions about this work can be found in Chapter 5. In addition, prospects for future work involving IFOGs are presented.

2 FUNDAMENTALS OF THE INTERFEROMETRIC FIBER OPTIC GYROSCOPE

Moving on from the context we established in the previous chapter, this chapter will provide the physical foundation and core structure of an optical gyroscope, in particular, the Interferometric Fiber Optic Gyroscope (IFOG). We will investigate how angular speed can be sensed through light interferometry. To this goal, the main physical phenomenon that enables the building of such a kind of sensor, along with its basic design, will be discussed. Then, some of the key aspects of the technical implementation around the system that are commonly used to improve its performance will be presented. The knowledge and physical intuition gained from this first investigation will be further used as the foundation to describe our IFOG instrumentation and studies.

2.1 The Sagnac Effect

The basis of any modern optical rotation sensor is the Sagnac Effect (or Sagnac-Laue effect), demonstrated by Georges Sagnac in 1913 [16], that ultimately shows how two counter-propagating light waves in an interferometric path produce, upon recombination, an interference pattern proportional to the paths angular speed. This section will provide a brief explanation of this effect, as well as its mathematical description, which will be necessary throughout the rest of this chapter. A more historical approach and in-depth explanation of the physics behind the Sagnac Effect can be found in Lefèvre's work [5].

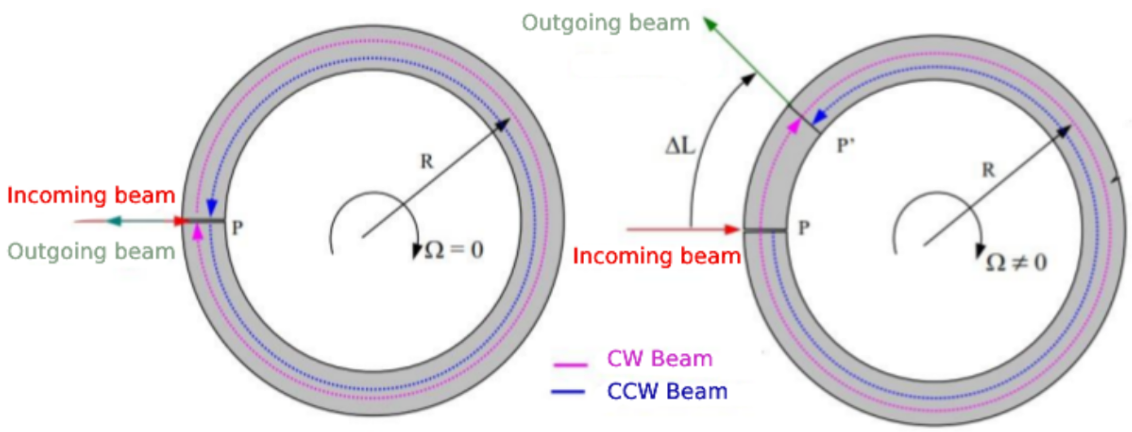

Figure 2.1 – Sagnac Effect on a circular interferometer path. Left: no rotation over the path; Right: non-zero rotation over the path. Adapted from [11] and [4].

Figure 2.1 represents an ideal, single loop, circular interferometer path, in which light is split at the entry point P, traversing both a clockwise (CW) and counter-clockwise (CCW) path. When the loop is at rest (2.1 - left), both light waves travel the same path and are recombined after the same travel time $\tau = 2\pi R/c$, resulting in totally constructive interference, therefore outputting the same optical power that was emitted at the input. When the loop is rotating (2.1 - right), the waves experience a slightly different optical path, and are recombined at a different point (P') slightly out of phase, resulting in a partially destructive interference that is proportional to the angular speed Ω. Equation 2.1 computes the time difference between both waves' travel time with respect to Ω.

$$\Delta\tau = \frac{(2\pi + \Omega\tau)R}{c} - \frac{(2\pi - \Omega\tau)R}{c} = \frac{2\Omega\tau R}{c}, \tag{2.1}$$

where Ω is the angular speed experienced by the interferometer, R is the loop radius, c is light speed in vacuum, and τ is the light propagation time inside the interferometer. The *propagation time* τ is a very important interferometer parameter that is related to its construction, given by:

$$\tau = \frac{2\pi R}{c}. \tag{2.2}$$

Combining equations 2.1 and 2.2, we have:

$$\Delta\tau = \frac{4A\Omega}{c^2}, \tag{2.3}$$

where A is the interferometer loop area - which is a circular, optical fiber path in this case. We can then translate this time difference into a phase difference, as the following:

$$\Delta\phi = \omega\Delta\tau = \frac{4A\omega\Omega}{c^2}, \tag{2.4}$$

where ω is the light angular frequency.

Finally, we can rewrite Equation 2.4 in terms of the interferometer constructive parameters, such as whole loop length L and diameter D, and an optical parameter of light wavelength λ, resulting in:

$$\Delta\phi = \frac{2\pi LD}{\lambda c}\Omega = F_s\,\Omega, \tag{2.5}$$

where F_s is known as *optical scale factor*, the optical sensitivity of the gyroscope. This factor is used to convert angular speed to Sagnac phase shift and is only related to the interferometer construction parameters.

In 1976, Vali and Shorthill [17] demonstrated that this interferometer sensitivity could be increased by employing a multiturn fiber coil design, which leads to a final sensitivity multiplied by N: the number of coil turns. The Sagnac phase shift can still be expressed by Equation 2.5, as the parameters L and D represent the total interferometer area. As a result, this kind of interferometer is able to achieve higher sensitivity while keeping a relatively small size when compared to those employed in the past [18].

Note that we have described this effect considering that light is traveling in an ideal medium, therefore with speed equal to c, the speed of light in a vacuum. The propagation of light in a moving medium with refractive index n analysis is found in [5]. One should note that the mathematical results of interest remain the same in both cases, regardless of the medium.

2.2 IFOG Configuration

Typically, the optical response of an IFOG is converted into an electrical current signal through a photodetector. Figure 2.2 shows the electrical response in respect to the Sagnac phase shift caused by a sensed rotation. Equation 2.6 describes this response.

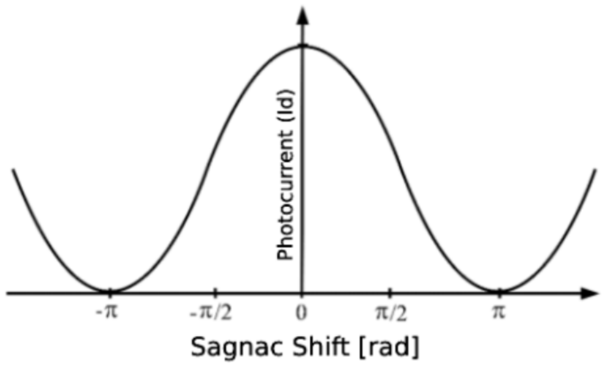

Figure 2.2 – Typical IFOG response seen on the photodetector.

$$I_d = \frac{I_0}{2}(1 + \cos(\Delta\phi_s)), \tag{2.6}$$

where I_d is the output photocurrent at the detector, I_0 is the maximum output current (when no rotation is sensed), and $\Delta\phi_s$ is the Sagnac phase shift due to rotation.

2.2.1 Dynamic Modulation and Closed-Loop Control

Analyzing Figure 2.2 and Equation 2.6 makes it clear that an interferometer with no optical modulation has a cosenoidal response. This leads to two major problems with this kind of design: (1) the gyroscope will have poor sensitivity to low- and high-speed rotations; (2) rotation sensed in any direction along the sensible axis yields the same output, being indistinguishable.

To address both of these problems, a modulating device capable of producing a controllable phase shift between the counter-propagating light waves is installed on the optical path of the IFOG. Two kinds of modulating devices are commonly used in this kind of application: (1) a piezoelectric modulator (PZT); (2) a $LiNbO_3$ multi-functional integrated optics chip (MIOC).

The PZT consists of a cylinder made with a piezoelectric material (that expands proportionally to an applied voltage) with optical fiber looped around it. This device is installed on one end of the interferometer coil, and when voltage is applied to it, the cylinder expansion produces an increase in the optical path length. This increase generates a phase difference between the counter-propagating light waves.

Figure 2.3 represents a modulation timing diagram considering a PZT modulator. This scheme depicts an easy-to-follow dynamic modulation scenario and should be helpful in understanding the IFOG system state during operation. A brief explanation of the diagram reading is provided below.

Incident beam on $t = \tau_1$		
CW Path	L	L
CCW Path	$L + \Delta L$	$L + \Delta L$
PZT Voltage Level	V_M	0
Timestep (τ)	τ_1	τ_2

Incident beam on $t = \tau_2$		
CW Path	L	$L + \Delta L$
CCW Path	L	L
PZT Voltage Level	0	V_M
Timestep (τ)	τ_2	τ_3

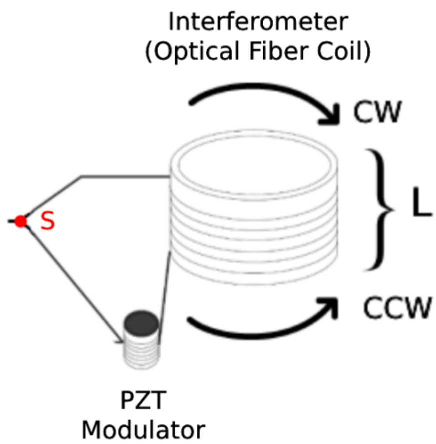

Figure 2.3 – Dynamic modulation timing diagram using a PZT as phase modulator.

Figure 2.3 shows an interferometer coil of propagation time equal to τ, and with a PZT modulator installed at its CCW input. The whole path length, when the PZT is not being driven by any voltage, is equal to L. When the PZT is driven, there is a small change of $+\Delta L$ over the PZT path, resulting in a total path length of $L + \Delta L$. Light is split at point S into two beams that will travel in opposite directions (CW and CCW). In practice, PZT modulators are not suitable for the implementation of digitally modulated IFOG, due to the required high frequency response. Usually, for digitally modulated IFOGs, MIOCs are used for modulation, as explained below. However, to facilitate the understanding of the dynamic behavior of the modulated gyroscope, we are considering the PZT represented in Figure 2.3 ideal, with infinite response frequency.

First, we will take a look at the initial timestep of τ_1, assuming that a voltage (V_M) is being applied to the PZT. In this case, the CCW beam will travel a path of $L + \Delta L$ during τ, while the CW beam will travel along L. At the start of timestep τ_2, PZT voltage is set to zero (0), meaning that the outgoing CW beam will not be affected by the ΔL change. Therefore, the outgoing beams will meet after traveling different path lengths, resulting in different times of flights and, ultimately, phase interference.

Now, starting from timestep τ_2, PZT voltage is already set to 0, meaning both CW and CCW beams will travel along a path of L. After the propagation time τ, the PZT is driven, and the outgoing CW beam will now have an increased distance to travel, resulting in a total path of $L + \Delta L$. Again, the same time of flight difference is seen due to different path lengths, resulting in phase interference.

Note that if the voltage over the modulator is always constant, both beams would travel the same path of $L + \Delta L$ (or L), resulting in no travel time difference, neither phase difference. So, in order to have modulation over the optical signal, a continuous voltage shifting over the modulator is needed. Hence the name, *dynamic modulation*.

The same effect can be produced by employing the other kind of phase modulator, the MIOC. Apart from being able to apply phase modulation, this device also consists of a Y-waveguide, meaning it is installed before the interferometer coil, as it will split the incoming light wave. When voltage is applied to the MIOC terminals, an electric field is produced between its branches, resulting in a small change of the refractive index of the waveguides that is linearly proportional to the applied voltage (Pockels Effect [19]), phase-shifting both waves.

For the sake of simplicity, we can still use Figure 2.3, along with the explanation provided above, to understand dynamic modulation when employing the MIOC. One can picture the modulating effect of the MIOC as two PZTs, one on each end of the interferometer coil, that will be driven at the same time, one producing a change of $+\Delta L/2$ and the other $-\Delta L/2$. The resulting phase difference is the same as the single PZT scenario depicted before.

MIOCs have been the usual choice of phase modulator on IFOG designs since the 1990s [5]. PZTs modulators are usually easier to manufacture and less expensive than MIOCs, but limit scale factor accuracy [20], degrading the gyroscope performance. Whereas, the latter is capable of operating on a much higher bandwidth than PZTs (around 300 MHz) and does not affect scale factor accuracy.

The modulation scheme that is still used as a basis for all-digital IFOGs implementation was introduced by [21]. A two-level, square-wave modulation of frequency $1/2\tau$ and amplitude $\pi/2$, depicted in Figure 2.4, in which the phase shift is computed through the difference between two consecutive phase samples.

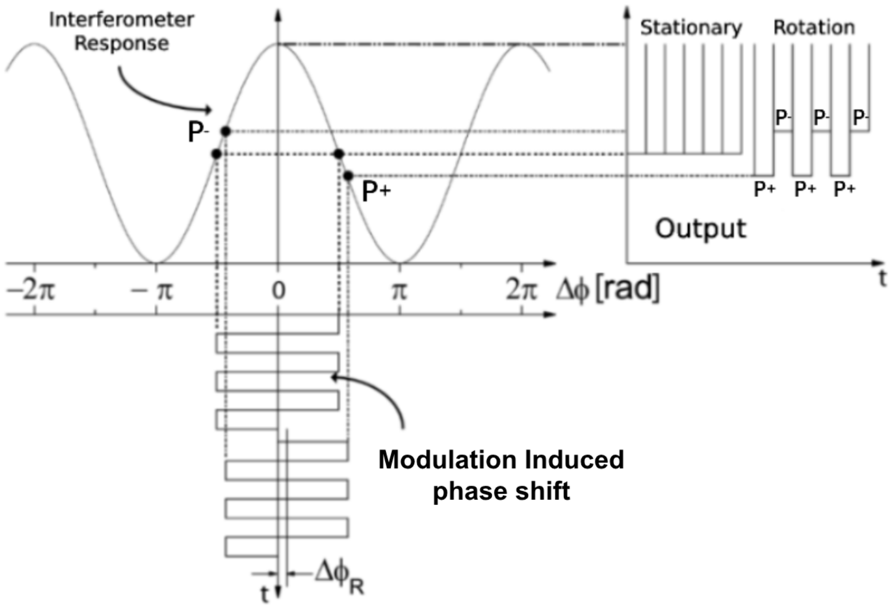

Figure 2.4 – Two-level square-wave modulation scheme. Adapted from [5].

It can be seen in Figure 2.4 that each modulation level transition causes the output signal to spike. This happens because, while transitioning, the optical signal swings between an output that corresponds to $+\phi_M$ and $-\phi_M$, passing through the "zero phase output", where there is totally constructive interference. That corresponds to the maximum output power, causing a peak at the detected signal. Note that this transition is observable because the modulation signal has a finite slew-rate and, thus, is not instantaneous. Equation 2.7 shows the expected photocurrent at the detector.

$$I_{d[M]} = \frac{I_0}{2}(1 + \cos(\Delta\phi_s + \Delta\phi_M)), \tag{2.7}$$

where $I_{d[M]}$ is the current output from the photodetector for a modulated input, $\Delta\phi_M$ is the phase difference induced by the modulation signal to set the modulation depth.

This type of modulation addresses both problems stated at the beginning of this section, meaning that it is now possible to determine the rotation direction and, by changing the modulation depth (amplitude), choose an operation point over the interferometer characteristic response. However, it should be noted that this response is not linear with increasing sensed velocities. This is called *open-loop* operation mode in an IFOG.

A *closed-loop* operation was also implemented by [21]. A digital ramp signal can be added to the square-wave modulation in order to cancel out the Sagnac phase shift sensed by the interferometer, keeping the response fixed at the operation point as if there is no rotation being sensed. Therefore, the desired rotation can be measured through the ramp's slope. Figure 2.5 and Equation 2.8 show the modulation ramp signal and expected photocurrent response, respectively.

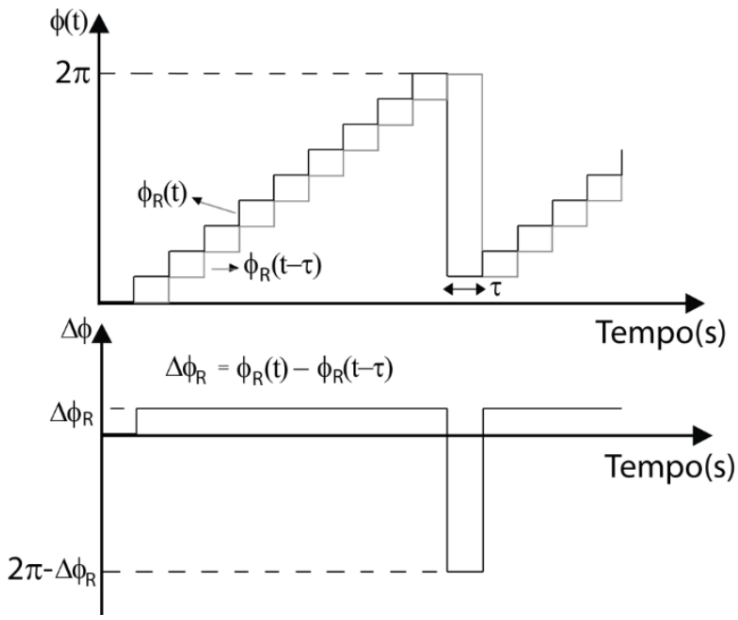

Figure 2.5 – Ramp signal employed to close the modulation loop (above). Equivalent phase shift induced by the ramp (below) [5].

$$I_{d[M]} = \frac{I_0}{2}(1 + \cos(\Delta\phi_s + \Delta\phi_M + \Delta\phi_R)), \tag{2.8}$$

where $\Delta\phi_R$ is the phase difference induced by the modulator to generate the ramp signal. Since the modulation signal, including the ramp, is produced by the IFOG embedded system as a modulator driving voltage, its span is limited to a maximum output. It can be seen in Figure 2.5 that the ramp signal is being reset after reaching this threshold, with an equivalent amplitude of 2π. Lastly, secondary closed-loop control is also necessary to ensure proper modulation depth at the driver output, as both the modulator (MIOC) and the driver are sensible to temperature changes [22, 23, 24]. This control loop is known as 2π *control*, or *scale-factor control*.

Finally, the gyroscope implemented by [15], used as the basis for this work, accounts for all of the aforementioned techniques in its design. Figure 2.6 shows an overview of an All-digital IFOG system hardware. It should be noted that the IFOG used in this work follows this schematic.

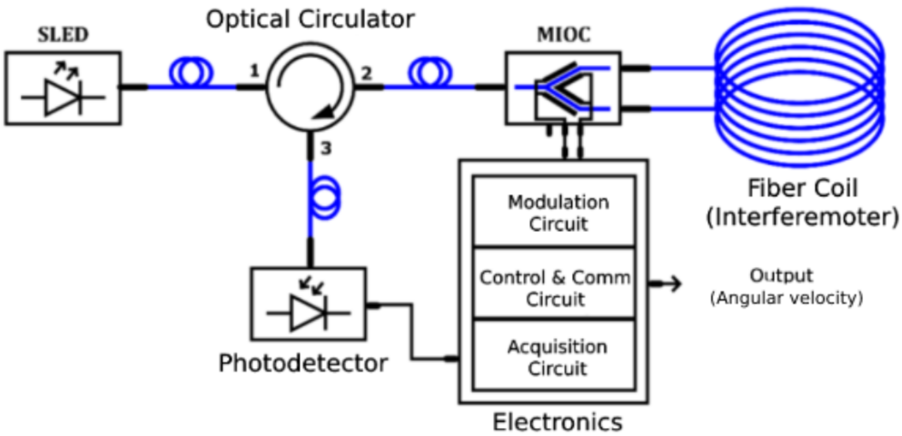

Figure 2.6 – All-digital IFOG schematic. Adapted from [15].

2.3 IFOG Performance Parameters

In order to be able to evaluate the effectiveness of any instrumentation design, it is important to understand the relevant parameters we need to look out for. Gyroscopes are rotational sensors, mainly used for navigation and position control to achieve an indirect measurement of position through mathematical integration of the sensed angular velocity. Therefore, even though it is essentially a rate sensor, its performance specifications are expressed in relation to the integrated variable: angle.

Gyroscopes' performance is typically classified through their Angle-Random-Walk (ARW), bias instability (or bias drift), and scale factor accuracy specifications. ARW has dominant effects, especially in short-term accuracy, where fast response is necessary, while bias drift dictates long-term stability [5]. As the scale factor multiplies the sensed signal, its accuracy is mostly important for high-speed sensing applications.

Angle-Random-Walk is a measurement of how rate noise affects the integrated signal. If we integrate a noisy signal from any gyroscope, the noise will accumulate between each integration step, meaning that the output angular error builds up over time. Consequently, each angle computation will have an increasing deviation from the past one, and the angle output will appear to be taking "random steps" from one sample to the next.

Therefore, ARW is a noise parameter represented in $^\circ/\sqrt{\mathrm{h}}$, indicating how precise the angle measurement is over time. Its value is related to both optical and electronic noise sources and how they affect the final measurement, and it is often referred to as "white rate noise" or "bias noise" [5].

Bias instability quantifies the extent to which the bias of a sensor deviates over time during its operation in constant temperature. This parameter is typically expressed in $^\circ/\mathrm{h}$. It is important to note that bias instability differs from angular random walk (ARW) calculations, as the latter mathematically averages out the effect of white noise during the integration of the output rate signal in comparison to bias instability. This means that the predominant effect over extended periods of operations is given by bias drift, rather than ARW.

Both of these parameters can be assessed through the Allan variance method, which is the standard procedure for gyroscope characterization recommended in IEEE-STD-952-1997 [25]. The Allan variance is intended to estimate stability due to noise processes and not that of systematic errors, primarily developed to measure frequency stability of clocks oscillators [26].

Table 2.1 depicts how gyroscopes are typically classified over these parameters, including the most common sensor technology employed to meet the requirements of commercial systems. It is clear that the fiber optic gyroscope is one of the most relevant technologies for high-end applications.

Table 2.1 – Gyroscope technology comparison in terms of its performance parameters. Data from [5, 3, 4].

Performance Grade	**ARW** [$^\circ/\sqrt{\mathrm{h}}$]	**Bias Instability** [$^\circ/\mathrm{h}$]	**Gyro Technology**
Rate Grade	> 0.5	1 to 1000	MEMS
Tactical Grade	0.5 to 0.05	1 to 10	MEMS
Intermediate Grade	0.05 to 0.005	to 1	RLG/FOG
Inertial Grade	< 0.005	< 0.01	RLG/FOG
Strategic Grade	< 0.0003	< 0.001	RLG/FOG

2.4 Recent IFOG Development

In order to enhance the performance of the IFOG sensor, it is essential to continually push the boundaries of its development and explore novel approaches. To this end, UNICAMP has been actively engaged in theoretical and experimental research of IFOG systems since 1997, as discussed in the previous chapter. The most recent work regarding the system development was concluded by Bacurau in 2016 [15], and its results are the basis of this work, as the experimental IFOG setup is the same.

Bacurau's IFOG design was able to significantly reduce the electronics complexity when compared to the previous project [14], eliminating a series of electronic devices such as: analog switches, direct digital synthesizers (DDS), one analog-to-digital (AD) and one digital-to-analog (DA) converter, one processing unit and active filters. Table 2.2 shows a direct comparison between those two versions. This design was able to achieve the best performance throughout the history of IFOG development inside UNICAMP. Its ARW was measured as $5.4 \cdot 10^{-4}\ ^{\circ}/\sqrt{\mathrm{h}}$ and bias instability as $1.9 \cdot 10^{-3}\ ^{\circ}/\mathrm{h}$, comparable to most commercially available high-end IFOGs at the time.

Table 2.2 – Comparison between the most recent IFOG design in UNICAMP and the previous one.

	Previous design	**Bacurau's design**
Processing Units	2 (1 CPLD and 1 ARM7)	1 (ARM M4F)
AD Converters	2 (24 bits $\Sigma\Delta$)	1 (24 bits $\Sigma\Delta$)
DA Converters	3 (one 16 bit and two 10 bits)	2 (one 16 bits and one 20 bits)
Active Filters	4	0
DDS	1	0
Analog Switches	4	0
PCB Area	89 cm²	62 cm²

His work also contributed to future improvements in IFOGs design by proposing a theoretical noise model, that accounts for optical and acquisition circuits noise, which can be used to convert input voltage noise spectral density to ARW. This model can be used to find an optimal modulation depth that maximizes signal-to-noise ratio (SNR). It is also useful to evaluate bottlenecks (optical and electronics) in the IFOG design with respect to the noise parameters.

Finally, some improvement points were identified in his work, such as the intensity modulation within the phase modulator (MIOC). This is a relatively unaddressed topic in the literature, and existing proposed suppression methods can be of difficult implementation [27].

2.4.1 Intensity Modulation

Intensity Modulation, also referred to as Residual Intensity Modulation (RIM) or Residual Amplitude Modulation (RAM), is an effect present in $LiNbO_3$-based phase modulators, such as the MIOC employed on most IFOG designs. These kinds of phase modulators provide, along with the desired phase shift over the lightwave, an undesired change of its intensity that is also proportional to the applied voltage. On IFOGs, this can induce errors in demodulation results, degrading the sensor performance [28, 29].

The RIM can be divided into a sum of a linear and a non-linear component, as discussed in [27], where linear RIM is mostly related to changes in the waveguide's refractive index caused by the modulation voltage [19], while non-linear is due to light that is coupled into the MIOC substrate, reflected at its bottom facet, and partially coupled back to the output fiber, which can result in interference between the guided light and the re-coupled beam (Figure 2.7) [27]. This effect originates from the manufacturing and constructive parameters of the MIOC. RIM is typically characterized during the device manufacturing process and is stated on the datasheet as a maximum relative intensity change [30].

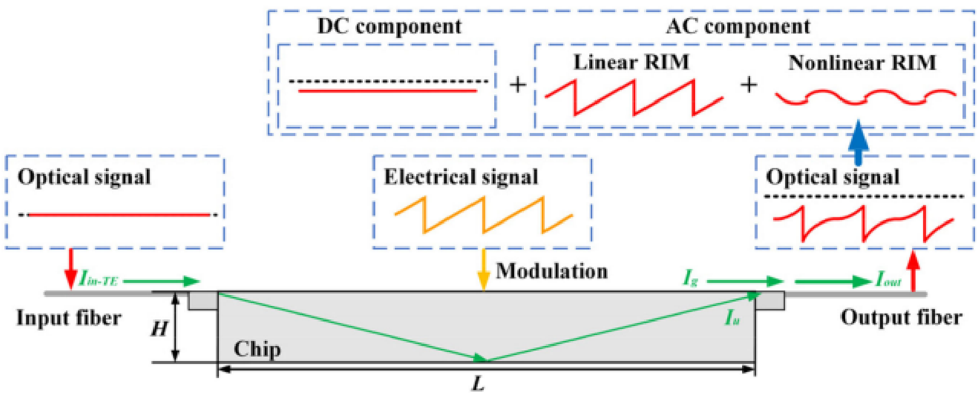

Figure 2.7 – Schematic diagram of the output intensity of the MIOC with modulation applied. I_{in} and I_{out} are the input and output intensities of the MIOC; I_g and I_u are the intensities of the guided and stray that reach the output port and re-couple into the output fiber of the MIOC, respectively. The decrease in the DC component is due to the loss of the MIOC itself and the losses at the input and output coupling points [27].

In 2020, researchers proposed a surface treatment to be done at the MIOC substrate by coating it with an anti-reflective layer [27]. This is shown to be an effective way to mitigate RIM, although it does not completely remove the effect, and requires a change in the manufacturing process of the modulator. In 2021, the same group of researchers presented mathematical modeling of linear and non-linear RIM, and simulations showing its degrading effect on all-digital FOGs output [31]. It reveals that RIM leads to large sudden changes in the sensor output during the closed loop feedback ramp reset, which can result in a bias and scale factor error of two orders of magnitude and one order of magnitude, respectively, depending on the MIOC characteristics.

An algorithm for RIM compensation in IFOGs was proposed in [29] based on the measurement of each individual MIOC branch light intensity dependency with applied voltage. A mathematical model on how each branch RIM coefficient affects the demodulated IFOG output is proposed, enabling software compensation of the effect. It is reported that, through simulation, RIM increases the output bias standard deviation, meaning it should also increase the sensor ARW. This method requires the modulator characterization to be done before the IFOG optical assembly.

2.4.2 IFOG Noise Modeling

As discussed in Section 2.3, IFOG noise specification is typically presented in ARW: a measurement of the angle standard deviation, resulting from mathematically integrating the gyroscope angular speed output that is affected by random noise processes. Applications that require precise measurements at short sampling times to sense high frequencies for compensation [32], or which need to evaluate and calibrate inertial navigation equipment [33], can require ARW to be lower than 10^{-5} order of magnitude. Therefore, understanding the noise sources that are most relevant to the IFOG design and modeling it has been a relevant research topic.

Typically, IFOG noise sources are divided into optical and electronic sources. The most relevant optical noise sources are shot and excess photon noise (also referred to as relative intensity noise). The transimpedance amplifier feedback resistor thermal noise has been considered the most relevant electronic source [34, 33]. Generally, other noise sources aren't considered on models because they come from imperfections in the manufacturing process of the system optics and electronics, and can be reduced through better design and processes. However, in practical IFOGs implementations, they are still relevant to the design, as discussed in [15], which shows how acquisition circuit noise sources, such as AD quantization and transimpedance amplifier (TIA) operational amplifier internal noise can contribute to overall system noise.

Photon shot noise arises from the quantum nature of photons; they are quantized and discrete, arriving independently onto the detector, resulting in random fluctuations in photon-electron conversion over time. Shot noise cannot be entirely avoided by technical means, as it is inherent to any signal arriving at the photodetector. Shot noise power is proportional to the square root of the average intensity over the detector [33]. Therefore, increasing optical source power should increase the signal-to-noise ratio (SNR) with respect to this noise. Examples of how this noise affects closed-loop IFOG output signal can be found in [34, 33, 35, 15].

Relative intensity noise (RIN) comes from the random beating amongst all the frequency components within a broadband spectrum source [35]. RIN power is proportional to the optical source power, meaning that SNR is not affected by the increase in optical power. Modeling of this noise source over IFOGs output signal can be found in [34, 33, 35, 15].

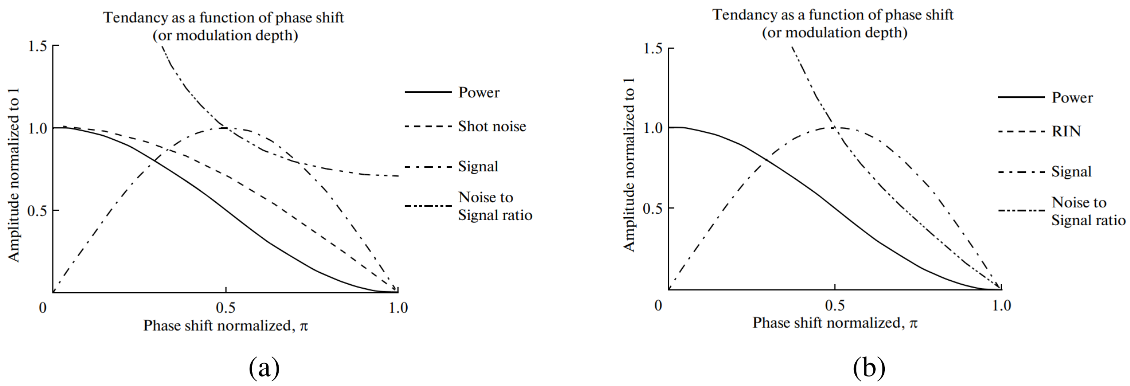

Figure 2.8 – Optical noises SNR on IFOGs. (a): Shot Noise; (b): Relative intensity noise. [33].

The thermal noise (or Johnson-Nyquist noise) is white noise that results from the motion of electrons in resistors. It depends on the resistor value over which the noise is measured at a temperature T, the Boltzmann constant, and the measurement bandwidth. As the transimpedance feedback resistor is typically large to set the gain for the low optical signal, and directly at the system output, its noise contribution is significant.

Theoretically, SNR increases as the transimpedance gain increases, thus improving the IFOG noise performance for higher resistor values. However, in practical implementations of the IFOG electronics, there is an optimal resistor value that is limited by the ADC full-scale range and the required bandwidth for the TIA lowpass filter in order to stabilize the signal for proper conversion during modulation (as shown in Figure 3.7). Discussion on how to set this optimal gain is found in [15].

Due to the optical noise characteristics, shot noise is considered to be the theoretical noise reduction limit [33], as RIN can be suppressed. Techniques to reduce RIN on FOGs have been proposed in the literature, such as employing two detectors and electronic subtraction of the noise [36], or through optical subtraction [37], without the need to redesign the system electronics. The latter work shows a significant improvement in the gyroscope ARW, from $1.4 \cdot 10^{-3}\ {}^{\circ}/\sqrt{\mathrm{h}}$ to $0.35 \cdot 10^{-3}\ {}^{\circ}/\sqrt{\mathrm{h}}$, before and after RIN subtraction, respectively.

It can be seen in Figures 2.8a and 2.8b how the SNR is affected by both optical shot and relative intensity noises with respect to the modulation depth of an IFOG. It should be noted that increasing the modulation depth sets the bias of the sensor output closer to $180°$, decreasing the light power at the detector (as explained in Section 2.2).

Simulations done in [34] show the ARW behavior with increasing optical power and modulation depth for an IFOG with 4300 m coil length, 0.2 m coil diameter, 1550 nm source wavelength, and 1.4 A/W detector responsivity. Figure 2.9 depicts the simulated ARW response using a noise model that considers only optical and the feedback resistor thermal noise. It can be seen that increasing optical power yields diminishing returns with respect to the ARW increase. This "saturation" like characteristic of the ARW in relation to the optic power is due to the SNR becoming independent from the incoming optical power. In those simulations, it happens when RIN becomes the dominant noise source, and increasing the modulation depth is prone to improve performance.

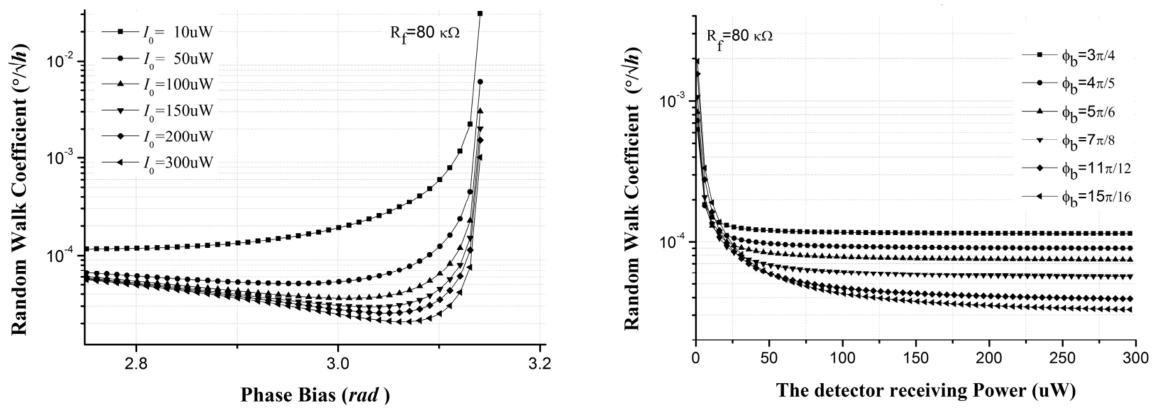

(a) (b)

Figure 2.9 – ARW noise-model simulation results. (a): ARW in respect to modulation depth for different incident optical powers; (b): ARW in respect to optical power. [34].

Discussion on different noise optimization and models are also found in recent publications [38, 39, 40, 41, 42], denoting the interest in pushing even further the IFOG performance. In [39, 42], ARW improvement is achieved by employing techniques to increase the detected optical power while suppressing RIN. In [41], a closed loop scheme has been proposed to set the optimal modulation depth with respect to ARW by minimizing RIN contribution to the gyroscope noise. According to [3], RIN suppression techniques are one of the main approaches to achieve better accuracy in high-precision FOGs. Still, RIN can only be suppressed until other noise sources become greater than it.

Finally, in [15] a noise model that includes most of the electronic noise sources is presented. It is shown how different acquisition circuit noise can predominate over RIN for higher modulation depths, and it is discussed how increasing the optical power source can improve the performance. Therefore, it is clear that being able to evaluate the sensor noise contributors individually is mandatory to improve IFOG designs.

2.5 Chapter Round-Up

In this chapter, we have seen the necessary foundation needed to understand how the Interferometric Fiber Optic Gyroscope works. We introduced the basics of the Sagnac Effect and how we are able to take advantage of it in order to build an IFOG. Then, we explained the main techniques employed on an All-digital IFOG design, as they are the same being used in this work. Finally, a brief review of the most recent works done in our university and of the main topics addressed in this work was presented. This knowledge will be used throughout Chapters 3 and 4.

3 SYSTEM DESIGN AND IMPROVEMENTS

Based on the information presented in Chapter 2, this chapter describes one of the key aspects of this project: the construction and behavior description of the novel all-digital IFOG embedded system. Here will be discussed the main electronics circuits that were employed, their role in the system, and the importance of timing and synchronization in the design. The idea of this chapter is to make the reader familiar with the overall functioning and handling of the developed all-digital IFOG, therefore contributing towards the understanding and future research on the topic.

3.1 Overall System Design

The IFOG electronic circuitry is mainly designed to convert the optical signal into an electric one, sample it, and process it. Moreover, it is also designed to control the modulation levels and, in closed-loop IFOGs, be able to drive the modulator in order to keep the interferometer output on a fixed, zero rotation, point. Therefore, the next sections were divided into three fundamental elements to ease the system design understanding: the IFOG optics, the acquisition circuit, and the modulation circuit.

It is important to note that this new system design is an update based on a previous electronic project that was already developed for this IFOG. This previous design has every circuit on a single, standalone printed-circuit-board (PCB), integrated with an ARM Cortex M4F, 80 MHz microcontroller as the processing unit. More details on this work can be found at [15]. The circuits for acquisition and modulation from this previous work were used as a base and upgraded. The improvements are discussed in the relevant sections to follow.

3.1.1 IFOG Optics

Before we begin to describe each one of the aforementioned elements in more detail, it is important to pay attention to the IFOG optical circuit characteristics. As in any instrumentation design, there are some constraints due to the application of the system. Here, most of those constraints when designing the electronics are in respect to the optics, to ensure proper timing when modulating and sampling the signal.

Parameters such as the light source wavelength, light propagation time (which is directly proportional to the coil length as described in Chapter 2), and MIOC half-wave voltage (V_π) are the most relevant to hardware and embedded software design. The latter is a specification found in the MIOC datasheet that describes its induced phase shift with respect to the voltage applied, being the voltage that corresponds to a π rad phase shift. The way each parameter affects the design will be discussed in more detail over sections 3.1.2.1, 3.1.2.2, and 3.1.2.3.

Table 3.1 – UNICAMP IFOG Optics Parameters.

Source λ [nm]	Propagation Time [μs]	MIOC V_π [V]	Scale Factor [s]
1300	6.8	3.54	3.04

The optical source employed in the developed system is a 1 mW SLED with an output wavelength centered at 1300 nm, while the interferometer (optical fiber coil) length is approximately 1.4 km, resulting in a propagation time of around $6.8\ \mu$s. Both the acquisition and modulation circuits have to be able to process the generated data in this given time. Lastly, the employed MIOC half-wave voltage is equal to 3.54 V.

Finally, as shown in Chapter 2, a combination of both optical source and interferometer parameters affects the Optical Scale Factor of the IFOG. This parameter is used to convert phase shift (measured through light intensity at the photodetector) into angular speed sensed by the interferometer and is equal to 3.04 s in our design.

Table 3.1 summarizes the optical parameters of the developed IFOG. Both the interferometer and the SLED source are depicted in Figure 3.1.

3.1.2 IFOG Embedded Electronics

We will now describe the key aspects of the design with respect to hardware and software. In order to make it more helpful for the reader, this section was broken into three parts: acquisition circuit, modulation circuit, and system timing and synchronization.

3.1.2.1 Acquisition Circuit

The acquisition circuit is a fundamental part of the system's operation. Its main functions are to transduce the light signal from the interferometer into a voltage signal, amplify it, condition it, and convert it from analog to digital signal for further processing. In order to

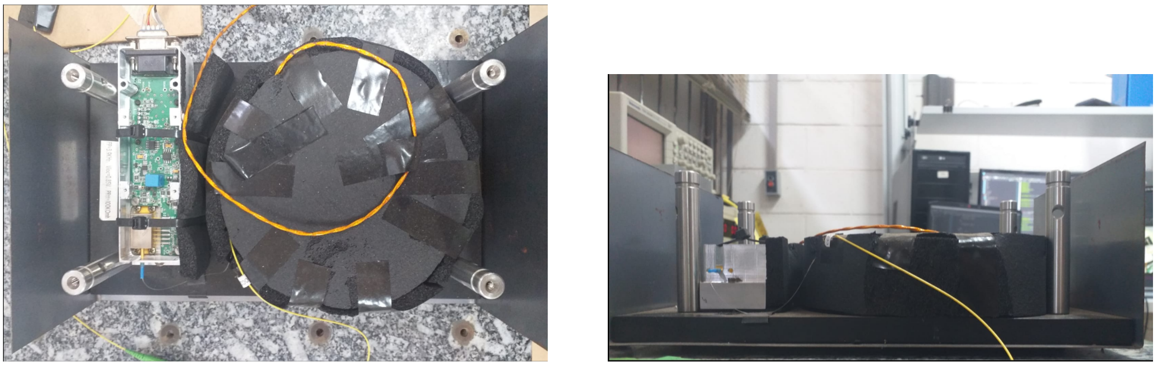

(a) (b)

Figure 3.1 – IFOG optical assembly. SLED source and interferometer covered with a thermal insulation material. (a); Top view; (b) Side View. Total assembly dimension is 260 x 160 x 100 mm.

do so, the light signal is converted into a current signal by a photodiode and then converted into a voltage signal, amplified and conditioned through a transimpedance amplifier. Finally, an analog-to-digital converter performs signal conversion for subsequent digital processing. Some of the most important electronics aspects of this circuit are:

- The photodiode, which is responsible for converting the optical signal into current. The photodiode must respond in the emission range of the optical assembly light source (1300 nm - as presented in Section 3.1.1). The photodiode employed in this project has a responsivity of 0.9 A/W in this range;

- An operational amplifier configured as a “transimpedance amplifier”, which will convert the photodiode’s current signal into voltage. This op-amp was chosen based on its low noise characteristics (in voltage and current), as well as its high “gain-band product”. This last parameter is of great importance because, in precision instrumentation systems such as this one, the necessary gain is generally very high since the light signal that reaches the photodetector is in the order of tens of microwatts. The op-amp used in this project is the OPA2356 (Texas Instruments), in differential configuration, which ensures greater robustness against interference in the electronic signal. The final transimpedance gain of the amplifier circuit is $2 \cdot 10^5\ \Omega$.

  A typical transimpedance amplifier configuration is depicted in Figure 3.2, and Equation 3.1 describes its voltage output.

$$V_{out} = I_{in} \cdot R_f, \tag{3.1}$$

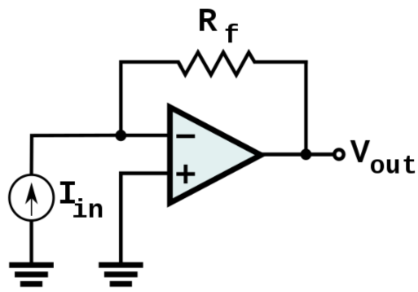

Figure 3.2 – Schematic illustration of a simple transimpedance amplifier.

where V_{out} is the voltage at the output of the circuit. In addition, R_f is the feedback resistor across the output and the inverting input, I_{in} is the current going through R_f (produced by the photodiode). Equation 3.1 shows that the gain is set by the feedback resistor. On a differential amplifier design, the total signal gain is doubled by the differential configuration, as shown in Figure 3.3.

- An analog-to-digital converter (ADC) capable of performing the conversion within the transit time constraint, with resolution and noise characteristics suitable for the project, is required. The original design uses the ADS1672 (Texas Instruments), a 24-bit ADC capable of performing conversions in up to 5.5 μs.

As an update to the acquisition circuit, the AD converter used was replaced by its most recent version available (ADS1675 - Texas Instruments), which is capable of performing conversions in up to 3.6 us, while the previous one was limited to 5.5 us, an improvement of 34%. Thus, this circuit can be used to acquire signals from interferometers with shorter propagation time, considering the usual techniques of signal modulation and demodulation. This is favorable as the new embedded system can be used with a wider range of optical assemblies.

Table 3.2, below, summarizes the acquisition circuit's most relevant parameters. Figure 3.3 depicts the electronic schematic for this circuit.

Table 3.2 – Acquisition Circuit Parameters.

Photodetector Responsivity [A/W]	Conversion Time (Old) [μs]	Conversion Time (New) [μs]
0.9	5.55	3.625

Note that, in Figure 3.3, the TIA signal output has a DC offset of 2.5 V, as required by the ADC datasheet [43]. It is also noticeable that this ADC has a full-scale range of $\pm$ 3 V.

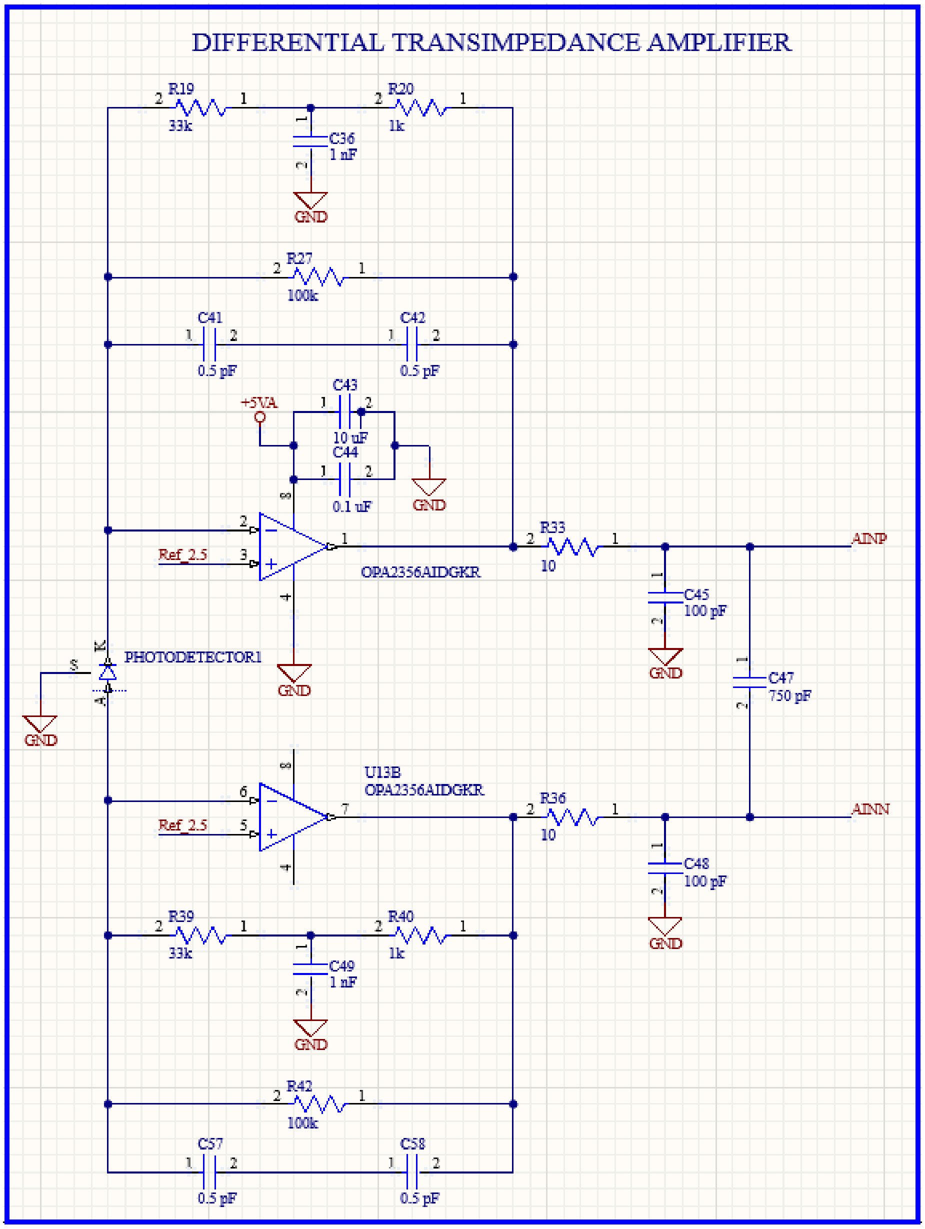

Figure 3.3 – Acquisition circuit electronic schematic.

3.1.2.2 Modulation Circuit

The modulation circuit's main role in the system is to enable optical signal phase control. In order to do so, the circuit must output a controllable voltage to drive the MIOC. This can be achieved by employing digital-to-analog converters (DAC) and multiple operational amplifiers.

Important parameters of the MIOC are its wavelength compatibility (1300 nm on the developed IFOG), and its half-wave voltage ($V_\pi = 3.54$ V). V_π is the voltage which, when applied to the MIOC terminals, produces a π rad phase difference between both propagating lightwaves. This last parameter, along with the maximum modulation circuit output voltage, will determine the IFOG modulation span.

In the circuit's final design, two DACs are employed in order to enable precise modulation voltage control. The main one is a 16-bit converter (AD5543 - Analog Devices), used to set the modulation voltage levels. There is also a 20-bit DAC (DAC1220 - Texas Instruments) that controls AD5543 V_{REF}. This DAC is exclusively employed to enable a precise 2π control during IFOG operation. AD5543 is a current output multiplying-DAC (MDAC), capable of producing both positive and negative voltages through the circuit presented in Figure 3.4, which has an output voltage described by Equation 3.2.

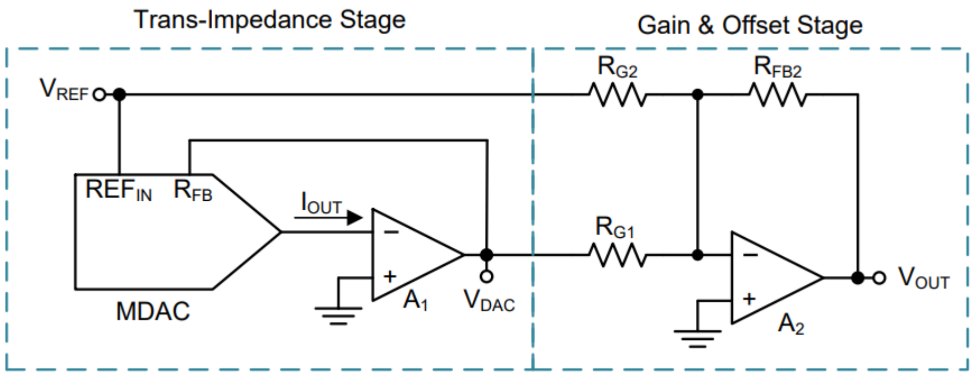

Figure 3.4 – MDAC four-quadrant scheme [44].

$$Vout(CODE) = \left(\frac{R_{FB2}}{R_{G1}} * \frac{V_{REF} * CODE}{2^{bits}}\right) - \left(\frac{R_{FB2}}{R_{G2}} * V_{REF}\right) \tag{3.2}$$

Equation 3.2 shows the MDAC output voltage for a given digital code in terms of the circuit (depicted in Figure 3.4) resistors. On our modulation circuit, this output is set to a range of ± 2.5 V.

A final op-amp is employed to produce a full-differential voltage output and set a final gain stage. This differential driver is the LMP8350 (Texas Instruments). Figure 3.5 depicts the modulation circuit schematic of our IFOG.

An important characteristic of all the employed op-amps throughout this circuit schematic, besides low-noise specifications, is the high slew-rate. Slew-rate is a parameter that depicts how fast the op-amp is capable of swinging its output, usually given in V/μs. This is a relevant parameter because the duration between voltage transitions on the modulator output is seen as spikes on the IFOG acquisition circuit, and the signal is sampled only after the output stabilizes.

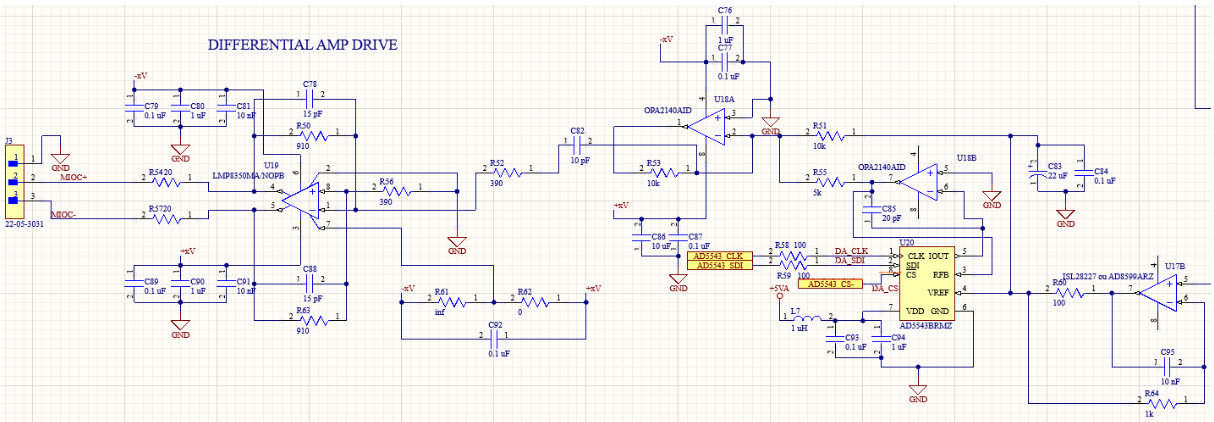

Figure 3.5 – Modulation circuit schematic.

In relation to the previous electronics, the modulation circuit was updated to be supplied with voltages between ±15 V (limited to ±5 V on the past design). This should improve the MIOC modulation span which, as a result, improves the IFOG full-scale range when operating in closed-loop.

Appendix A describes an important calibration procedure for the modulation circuit. High-resolution images of all the electronic designs can be found at the end of this document, in Annex A and Annex B, depicting the Analog board schematic and Digital board schematic, respectively.

3.1.2.3 System Timing and Synchronization

Correct timing and synchronization between signals play a crucial role in the performance and accuracy of the IFOG system. As explained in Chapter 2, in order to ensure a proper two-level square-wave modulation of the optical signal, the MIOC has to be driven at the interferometer's proper frequency. Then, the signal has to be sampled when the interferometer output is stable. Finally, the embedded system has to be able to compute the demodulation sequence before the next sample is ready, or else the operation will be desynchronized. In this All-Digital IFOG design, every signal timing is handled by hardware timers and triggers, therefore being independent of the processor unit.

The base time of the system is defined by the modulation circuit. A hardware timer is used to generate a pulse-width-modulated (PWM) signal with a period equal to the IFOG propagation time, which is connected to the 16-bit DAC chip select (CS) input. When this input is strobed by the PWM, the DAC will produce an output based on the last read input code that was sent through SPI. Figure 3.6 shows the modulation circuit output along with the CS signal.

Note that both DAC and ADC start signals are timed with a period of $\approx 6.8\ \mu$s, which is the employed interferometer propagation time τ.

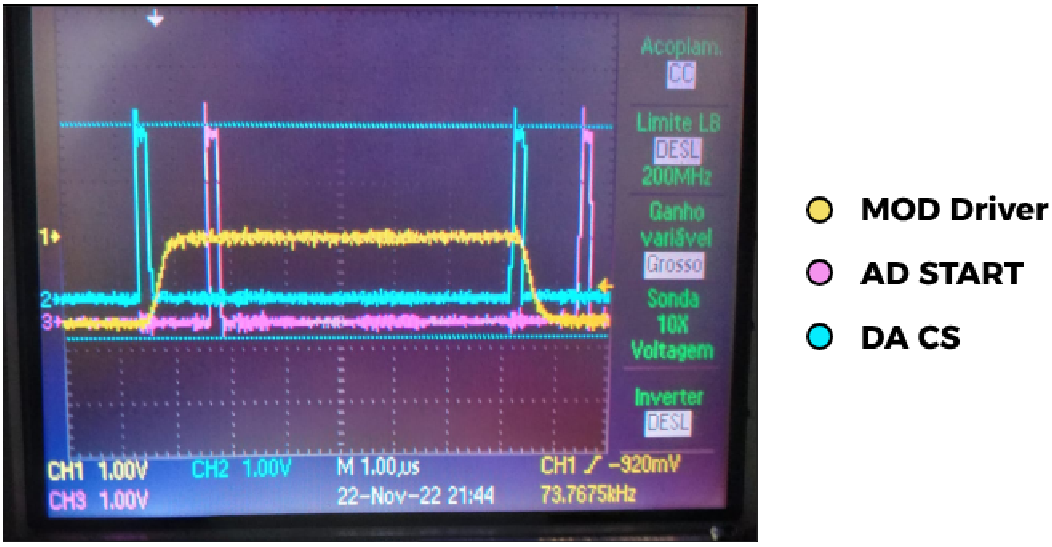

Figure 3.6 – Modulation timing signals. Modulation circuit output (yellow); DAC CS signal (blue); ADC conversion start signal (pink).

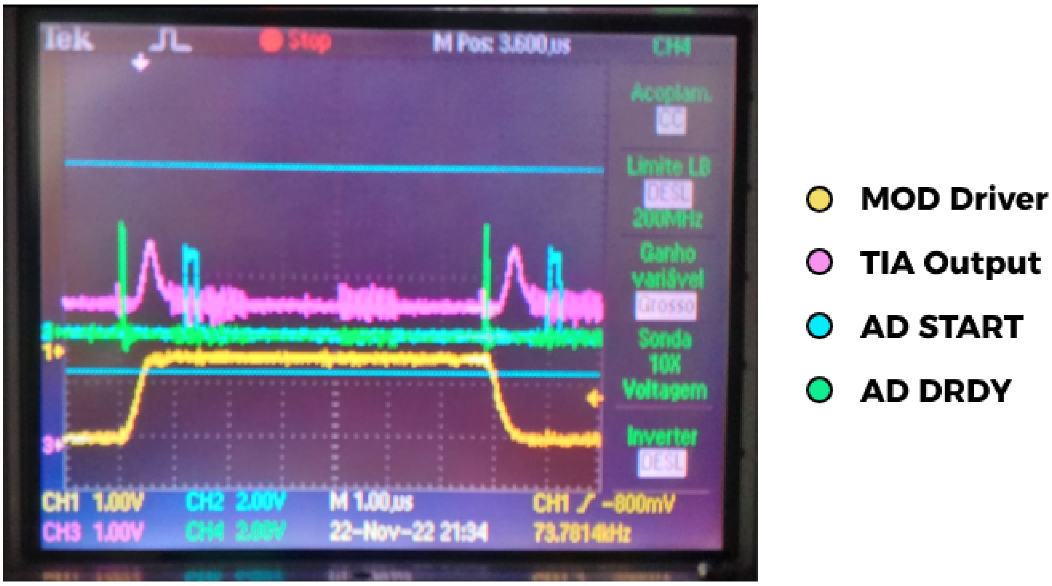

Figure 3.7 – Acquisition timing signals. Modulation circuit output (yellow); TIA output (pink); ADC conversion start signal (blue); ADC data ready signal (green).

This modulation change is seen at the interferometer output as a voltage swing across the acquisition circuit, depicting that, for a brief moment, the interfering waves went through constructive interference, outputting maximum optical power. This behavior was also explained in Chapter 2. Note that it takes a few hundred nanoseconds for the signal to become stable due to the TIA low-pass RC filter and op-amps slew-rate.

When the signal is stable again, we need to start the ADC sampling and conversion. To time and synchronize this with the modulation process, we make use, again, of hardware timers to generate another PWM signal. This PWM is also generated with a period equal to the interferometer propagation time, but it is slightly delayed from the modulation PWM through internal hardware triggering from the microcontroller. This delay ensures that the sampling will only occur when the signal is stable, as shown in Figure 3.7.

Finally, when the ADC is done converting a sample, it signals the microcontroller via a "data ready" (DRDY) pin. The microcontroller will then start the process to read this sample, process it, compute the next modulation step, and write it to the DAC. Every data transmission to both acquisition and modulation circuits is done through the Serial-Peripheral-Interface (SPI) protocol. Figure 3.8 shows both transmissions timing.

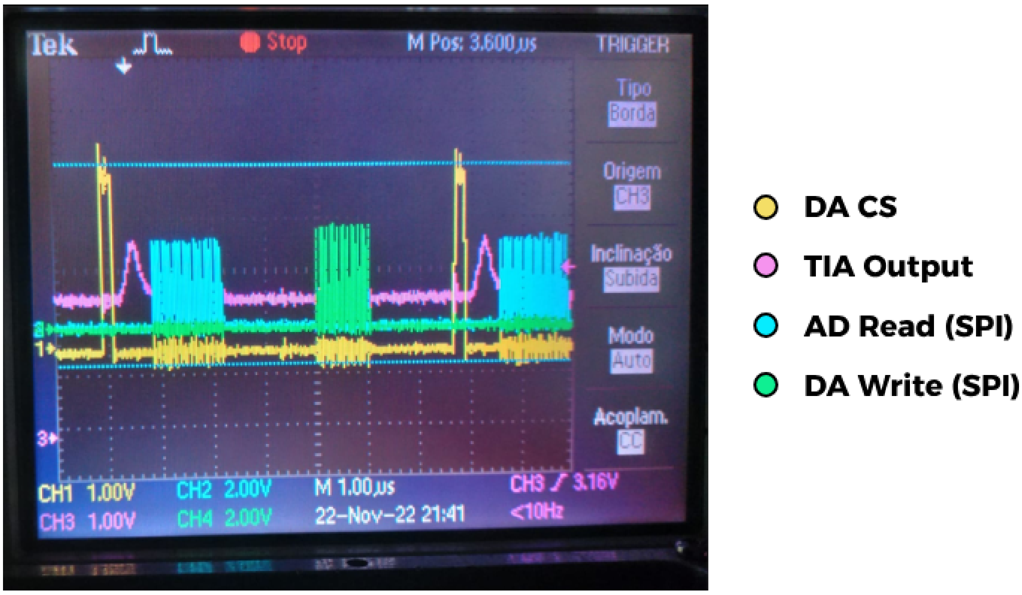

Figure 3.8 – SPI communication timing signals. DAC CS signal (yellow); TIA output (pink); ADC read transmission (blue); DAC write transmission (green).

3.1.3 New PCB Design and Microcontroller

Besides the improvements already described over the past few sections, such as improved conversion time and modulation range, there are design and processing unit updates as well. These changes were made in order to make our IFOG embedded system more suitable for different kinds of applications, more flexible, and easier to maintain.

Firstly, a major PCB design change was made: in contrast with the previous PCB (Figure 3.9), which includes all circuits (digital and analog) on a single board, we have separated them into two different PCBs, shown in figures 3.10a and 3.10b. The main purpose of having separate PCBs for digital handling, and analog acquisition/modulation circuits is to enhance system modularity. Both digital and analog boards have a *PC/104* connector, a special kind of connector designed to enable a stack-up arrangement of boards, as shown in Figure 3.11.

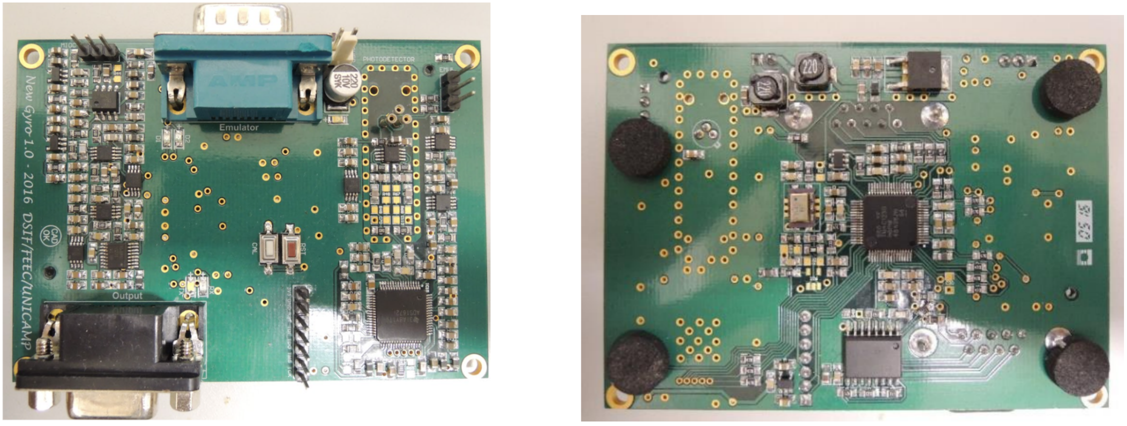

(a) (b)

Figure 3.9 – Previous PCB design. (a): Top view; (b): Bottom view. Dimensions are equal to 92 x 76 mm.

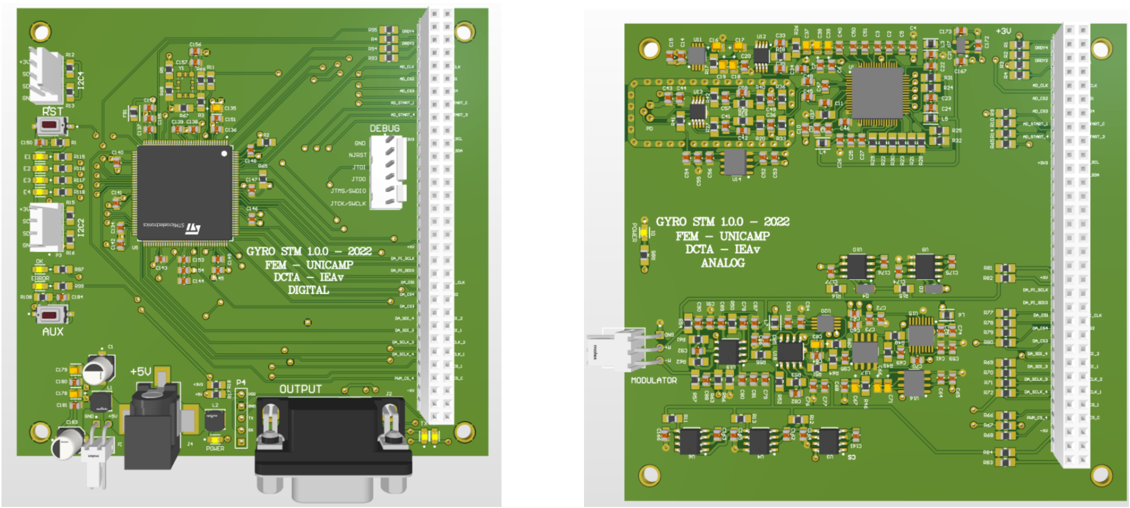

(a) (b)

Figure 3.10 – New modular PCB design. (a): Top view of the digital design board; (b): Top view of the analog design board. Dimensions of each board are equal to 100 x 95 mm.

This kind of design was conceived because each analog board is capable of handling both modulation and acquisition of a separate IFOG optical system, while a single digital board was designed to be able to handle the control and communication with up to four analog boards. Therefore, with this updated version, our embedded system should be able to employ a single processing unit to handle a 3-axis gyroscope system, commonly used in higher-grade navigation applications.

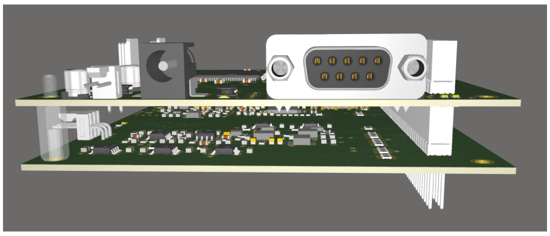

(a)

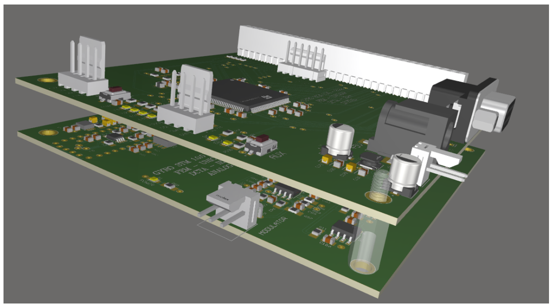

(b)

Figure 3.11 – Stack-up assembly example of two boards, one digital (above) and one analog (below). (a): Front view of the assembly; (b): Isometric view of the assembly.

The microcontroller is in charge of generating every signal described in the past sections, handling communications and processing all acquired data, as well as handling any data transmission to an external environment. Considering this, in order to enable this new design, the microcontroller was also updated to a more powerful one. A STM32H745ZIT6 (STMicroelectronics), a dual-core microcontroller composed of an ARM Cortex M7 capable of running at 480 MHz, and one Cortex M4F (240 MHz), was employed. In comparison with the previous design, the 480 MHz core is six times faster than the previous microcontroller, ensuring a higher instruction execution speed. This improvement in speed, along with higher peripheral availability, allows this new multi-axis system approach.

Embedded software development was anticipated to some extent through the use of a development kit based on the same microcontroller chosen for the new design (NUCLEO-144 STM32H745ZIT6). Then, by overriding the previous PCB signals with external wiring, we were able to control and implement the IFOG embedded code on the new platform. Figure 3.12 shows the overridden PCB.

In order for this external wiring to work, all data transmission lines (SPI) speeds had to be halved to avoid data corruption. Apart from that, no performance issues were noticed, as the system yielded the same ARW of $5.4 \cdot 10^{-4}\ ^{\circ}/\sqrt{\mathrm{h}}$ upon testing.

Throughout this work, even though acquired, the electronic components were not delivered in time to enable the complete assembly of this new design. Still, old gyroscope electronics PCBs from previous works were disassembled, and their equivalent components were used to build a total of two digital and two analog boards. Figures 3.13 and 3.14 show both sets of boards.

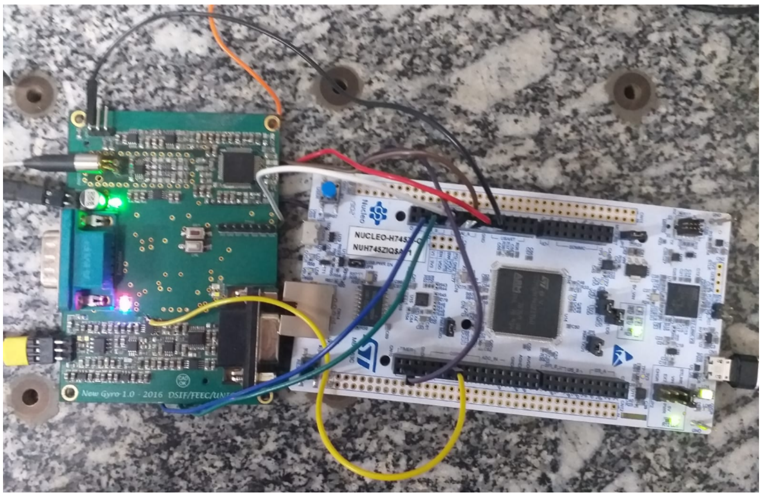

Figure 3.12 – New microcontroller development kit (right) overriding the previous electronics (left).

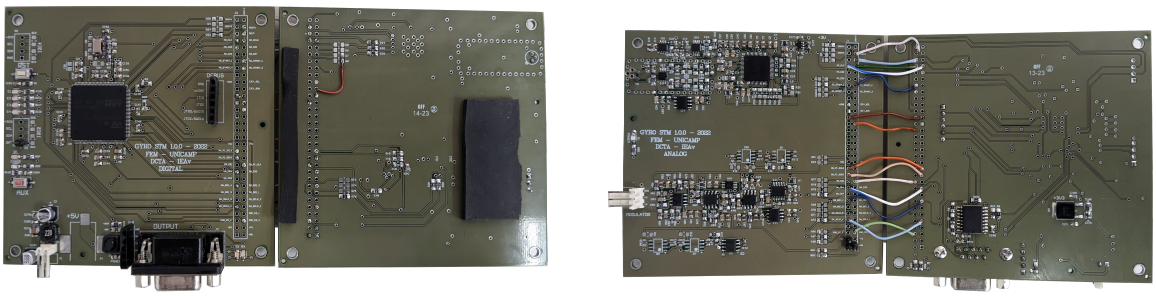

(a) (b)

Figure 3.13 – Assembled digital and analog board. (a): Front view of the digital and back view of the analog boards. (b): Back view of the digital and front view of the analog boards.

Figures 3.15 and 3.16 depict all the SPI communication timing signals generated by the new design. It can be noted that the ADC read transmission is completed on the dead-time between AD conversions (between AD Start and AD DRDY), which minimizes crosstalk from the high-speed digital signal to the analog part.

The first set of boards (3.13) were assembled in order to ease hardware testing, as the second (3.14) is stacked through soldered rigid wires, and not a connector. The lack of a connector difficulties the multiple-stacking assembly during the prototyping phase. Hence, this new hardware was not tested while controlling multiple boards at once. However, the embedded software that generates the control signals for multiple boards was developed, and its transmission signal timing can be seen in Figure 3.17.

All of the transmission signals depicted in Figure 3.17 are generated by a different SPI peripheral of the microcontroller. This means that there is no need for time multiplexing to handle separate transmissions, thus adding an insignificant amount of processing time when

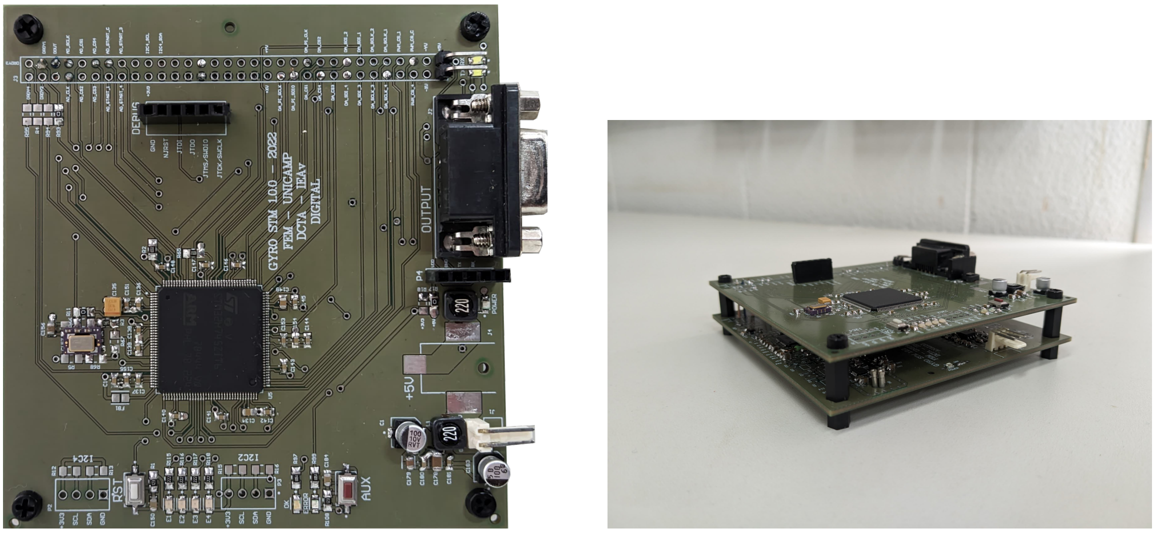

(a) (b)

Figure 3.14 – Assembled digital and analog board in a stack-up manner. (a): Top view of the assembly. (b): Isometric view of the assembly.

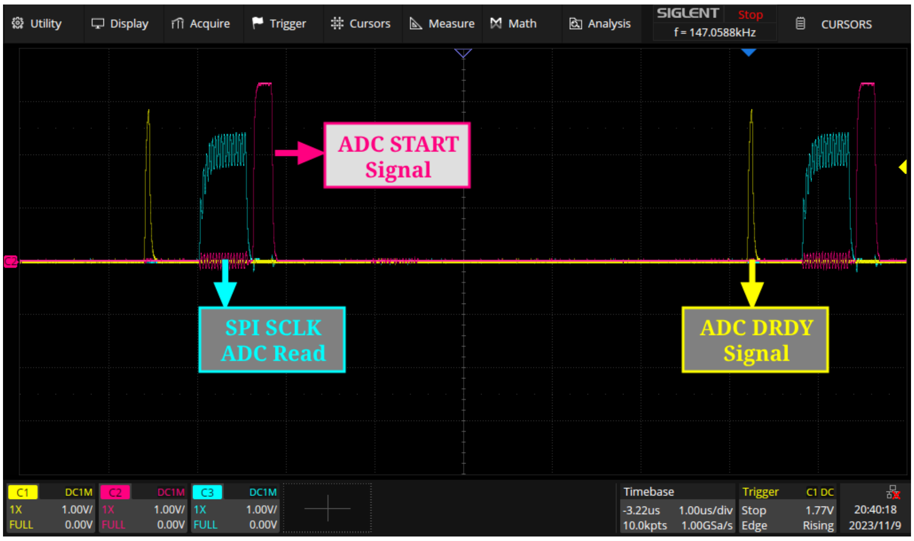

Figure 3.15 – New PCB design communication timing signals. ADC read transmission.

compared to a single analog board handle routine. Therefore, the system should be able to handle data processing in time when multiple analog boards are employed together.

An experiment to assess the ARW from both the first and second set of boards was conducted. The interferometer was kept stable over a workbench on our laboratory, subjected only to Earth's rotation. The two-level two-stage modulation ([15]) in an open-loop scheme with a modulation depth of 150° was employed; data was sampled at approximately 1 kHz in the embedded system and further processed through a digital low-pass filter with a cutoff frequency equal to 5 Hz. ARW was computed through Allan Variance [25], and the results are presented in Table 3.3.

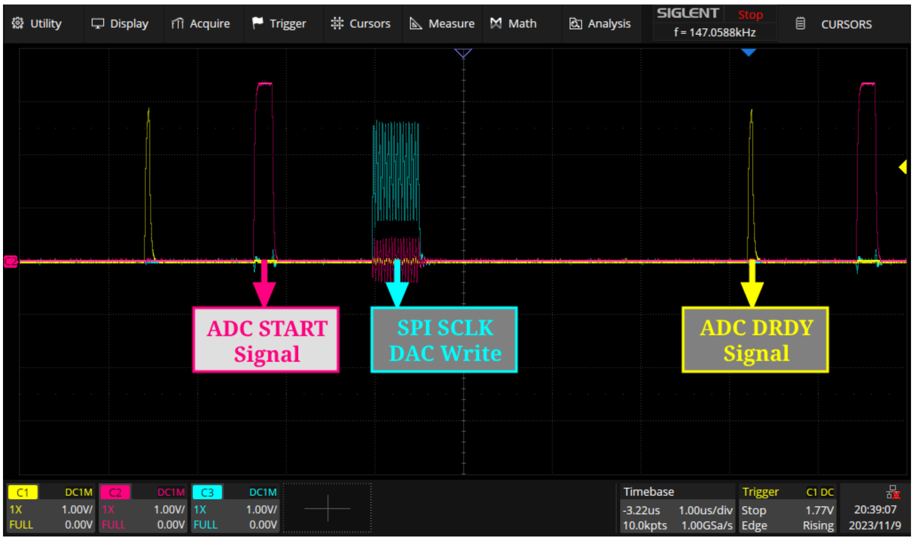

Figure 3.16 – New PCB design communication timing signals. 16-bit DAC write transmission.

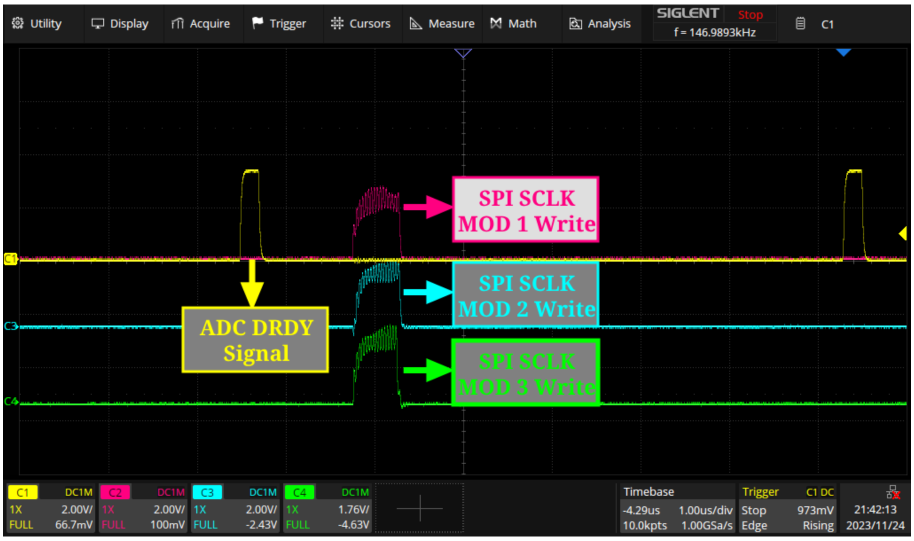

Figure 3.17 – New PCB design transmission signal for handling 3 analog boards modulator driver writes simultaneously. ADC DRDY signal is used for oscilloscope triggering and can be ignored.

Table 3.3 – ARW comparison between previous and new PCBs design.

PCB Design	**ARW** $^\circ/\sqrt{\mathrm{h}}$
Previous PCB	$5.4 \cdot 10^{-4}$
New PCB 1	$7.9 \cdot 10^{-4}$
New PCB 2	$7.0 \cdot 10^{-4}$

It is noticeable that both newly designed boards present a higher ARW value when compared to the previous design. Yet, the sensor performance is still good enough to remain at the top performing grade for gyroscopes presented in Table 2.1. This higher ARW is mainly due to increased electronic noise in the acquisition circuit, which will be discussed in the next chapter.

Finally, with an overview of the overall functional scheme of our IFOG embedded system, Figure 3.18 depicts a more detailed version of the IFOG schematic presented in Chapter 2 (Figure 2.6).

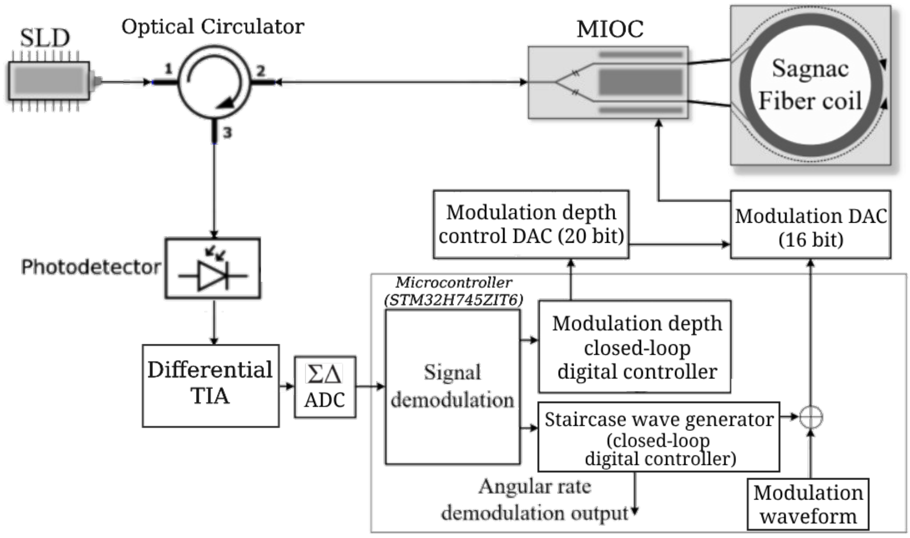

Figure 3.18 – Detailed schematic of an IFOG optics and embedded system. Adapted from [45].

3.2 Chapter Round-Up

In this chapter, it was shown how the physics behind the working principle of an IFOG, presented in Chapter 2, is accounted for the embedded systems design, along with an overview of the key electronic circuits role and behavior. It also presented some improvements to both acquisition and modulation circuits, processing unit, and a new PCB design that allows for a modular, multi-axis sensor arrangement. Lastly, the new design performance was compared to the previous one.

4 EXPERIMENTAL RESULTS

The previous chapter provided an overview of the employed IFOG embedded system and highlighted some of the key aspects of its implementation. In this chapter, the aforementioned system will be used to investigate an unaddressed issue known as Intensity Modulation, and a compensation technique is proposed. Moreover, discussion of an improvement to the IFOG noise model developed by Bacurau in [15] is proposed: the addition of the modulation circuit as one of the noise sources. Also, experimental validation of this model is discussed.

4.1 MIOC Intensity Modulation

As described in Chapter 2, the Multi-functional Integrated Optical Chip (MIOC) is an optoelectronic device used to shift the phase of a passing lightwave proportionally to an applied voltage while serving as a Y-coupler and a polarizer. Ideally, this kind of device should only provide phase shift, but there is also an amplitude dependency of the passing beam when in operation, characterized during the fabrication and stated on datasheets [30], known as Intensity Modulation. Even though this dependency is commonly under tenths of a percent over the total optical power, the changing voltage over the MIOC during the IFOG modulation leads to an undesired optical power fluctuation. Those are then read at the output as Sagnac phase shift, resulting in a noisier measurement in closed-loop IFOGs.

In 2016, Bacurau [15] was able to measure the Intensity Modulation amplitude on the MIOC employed in this project by applying a voltage ramp that spans the entire modulation circuit range using the IFOG electronics. He then estimated how this effect should translate to a sensed rotation at the output. His results were reproduced, using a transimpedance gain of $134 \cdot 10^3$ Ω, and are shown in Figures 4.1 to 4.4.

In order to convert this effect to rotation, we assume that each demodulated phase of the optical signal is affected by a scaling factor F, starting with 1, increasing for positive voltages on the driver, and decreasing with negative voltages, as shown in Figure 4.2. This is reasonable to assume since it represents the relative change of the optical signal according to the voltage across the MIOC terminals.

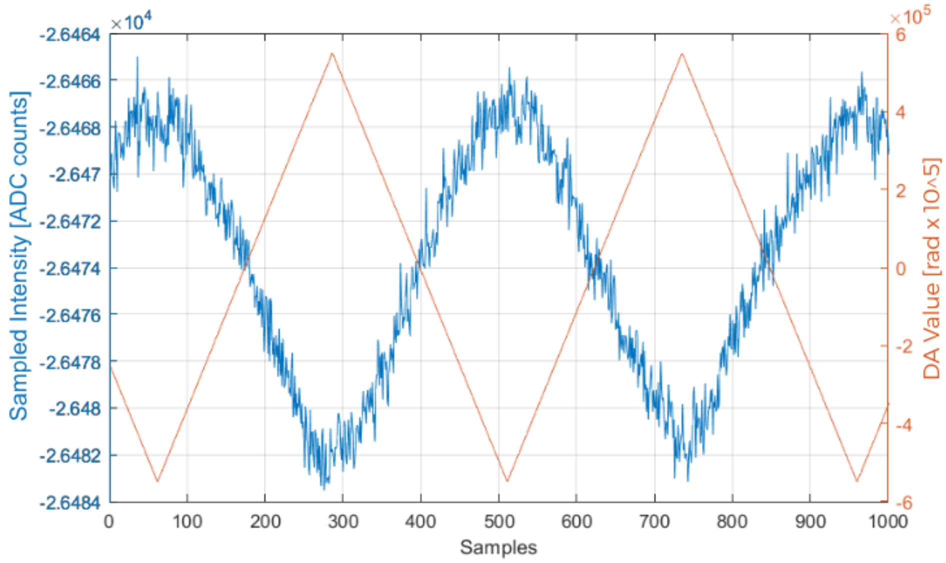

Figure 4.1 – Intensity Modulation measurement. Blue: digitized optical signal; Orange: Modulation Circuit Output.

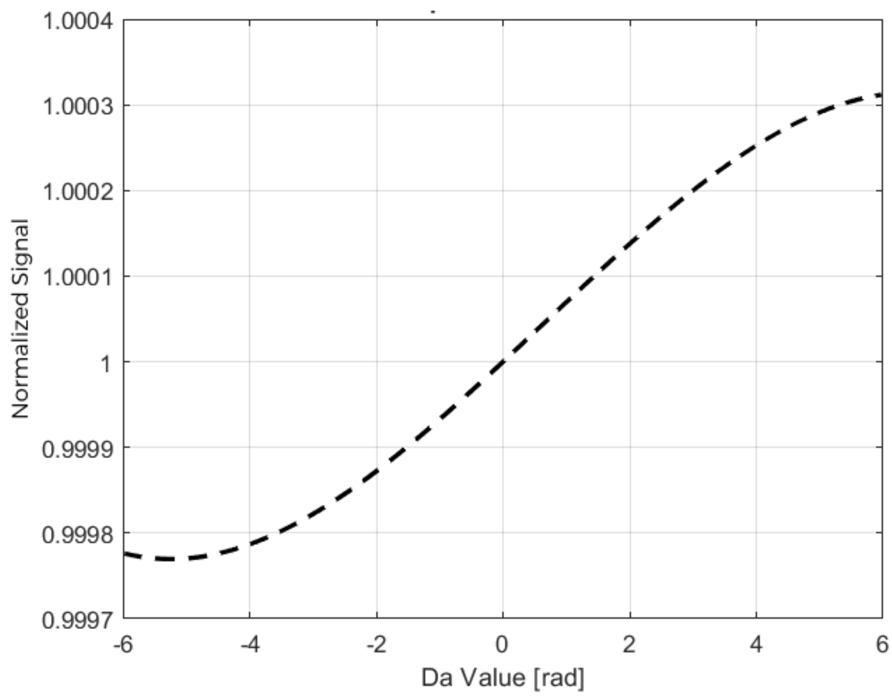

Figure 4.2 – Normalized measurement. Intensity Modulation over the full-range of the modulation circuit.

4.1.1 Original Modeling Approach

At first, we assumed that this factor F was the direct measurement result (Figure 4.2) from the modulator ramp experiment (Figure 4.1). As depicted in Figure 4.3 and Equation 4.1, each modulated phase undergoes an intensity change, being scaled by a different factor that is dependent on the MIOC input voltage.

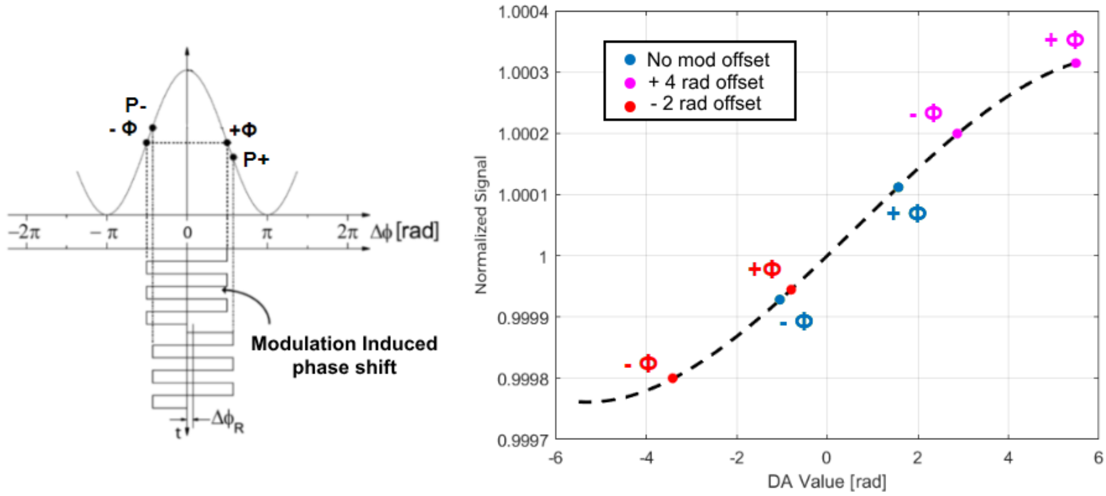

Figure 4.3 – Intensity Modulation factor for each phase considering a two-level $\pm 150°$ modulation. Each color represents both phases (ϕ_+ and ϕ_-) at different modulation offsets.

Figure 4.3 shows the intensity scale factor relative to a square-wave modulation on three different operation points of the MIOC employed. Note that each two sets of points represent a positive modulation phase step and a negative modulation phase step, which are subtracted from each other to obtain a value proportional to the angular speed. Equation 4.1 represents this process considering the effect of intensity modulation:

$$Sagnac^* = (F_+P_+) - (F_-P_-), \tag{4.1}$$

where F_+ and F_- are the scaling factors taken on ϕ_+ and ϕ_-, respectively, according to Figure 4.3; P_+ and P_- are the measured signals for each modulation step sample, according to Figure 4.3. And $Sagnac^*$ is the output "rotation" signal measured, before circuit gain and optical scale factor.

Then, by assuming a two-level modulation in an open-loop setup, we can compute the expected sensor output on any MIOC operation point, leading to the output depicted in Figure 4.4, after considering TIA circuit gain and optical scale factor. Note that this is the expected output (in $°/h$) only due to the Intensity Modulation effect.

One can see that the Intensity Modulation should dominate the output signal. Instead, when in operation, no significant effect is seen in any operation point (as later shown in Figure 4.9). This leads us to a revised model, discussed below.

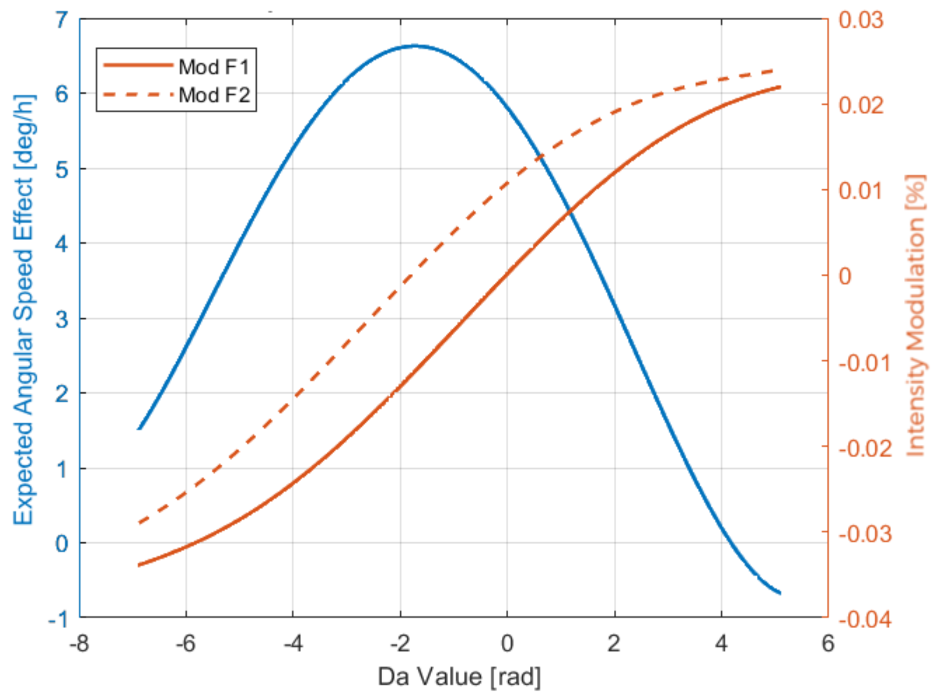

Figure 4.4 – Expected rotation at the output due to intensity modulation (blue). Intensity modulation scaling factor.

4.1.2 New Modeling Approach

If we take a look at the IFOG modulation timing diagram depicted in Figure 2.3 of Chapter 2, it is noticeable that a fundamental point is missing in the aforementioned model: when modulating, each acquired phase has to go through two voltage steps on the MIOC, into the interferometer and out. Taking this into account, the curve shown in Figure 4.2 actually depicts F^2, as the measurement was done through a DC ramp, causing the arriving lightwave at the photodetector to go through and back the MIOC at the same voltage level. Then, the curve that more correctly describes this scaling factor for each voltage is depicted in Figure 4.5.

Now, considering a square-wave modulation and open-loop setup, as each phase is measured after going through a voltage corresponding to ϕ_+ (or ϕ_-) and back through ϕ_- (or ϕ_+), the resulting scaling factor F_+ (or F_-) should be the same. This is because $F_+ = F(\phi_+)F(\phi_-)$ and $F_- = F(\phi_-)F(\phi_+)$, so $F' = F_+ = F_-$. Figure 4.6 shows the resulting factor F'.

The expected effect over the measured signal, in this scenario, then becomes:

$$Sagnac^* = (F'P_+) - (F'P_-) = F'(P_+ - P_-) \tag{4.2}$$

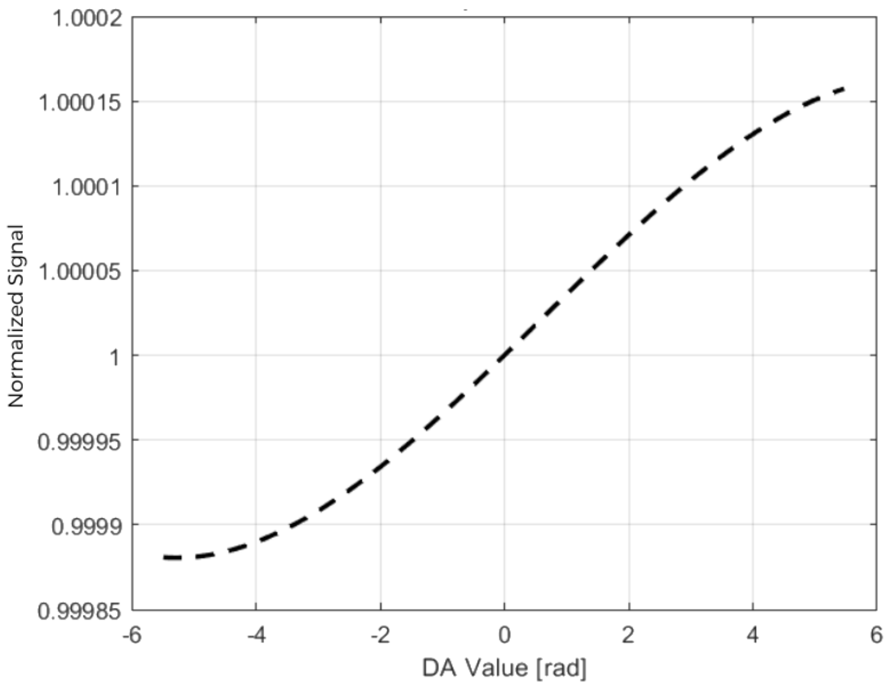

Figure 4.5 – Normalized measurement. Intensity Modulation over the full range of the modulation circuit. Computed through the new approach.

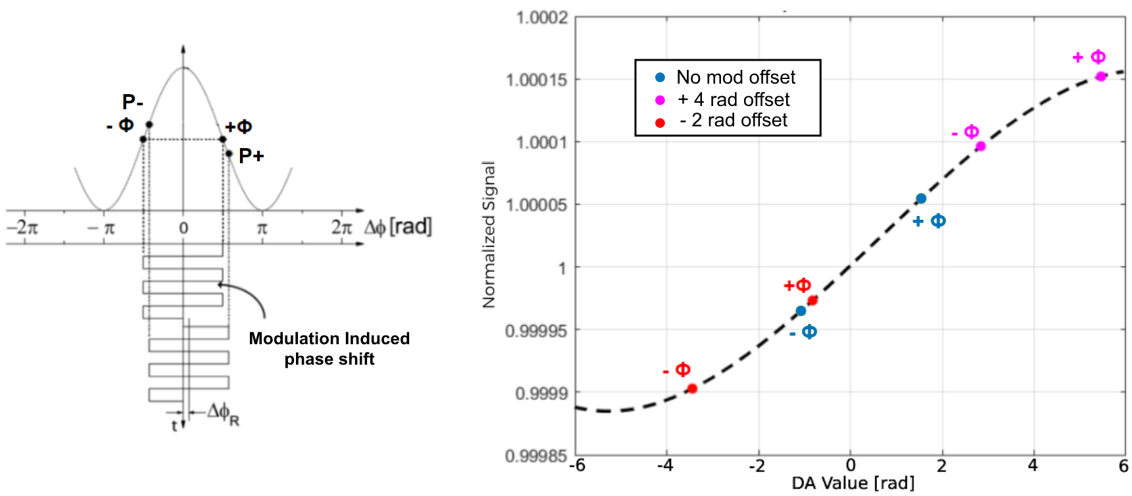

Figure 4.6 – Intensity Modulation factor for each phase considering a two-level $\pm 150°$ modulation. Each color represents both phases (ϕ_+ and ϕ_-) at different modulation offsets. Computed through the new approach.

In order to validate this model, the following experiment was done: instead of a DC voltage ramp, the modulator was set to output a square-wave while varying its DC offset across the whole modulator circuit output range. Then, we monitored a single phase (e.g., only P_+) at the output, and after normalizing the result, we can compare it using the model above (equation

4.2). Figure 4.7 shows a comparison between the new model and this experiment.

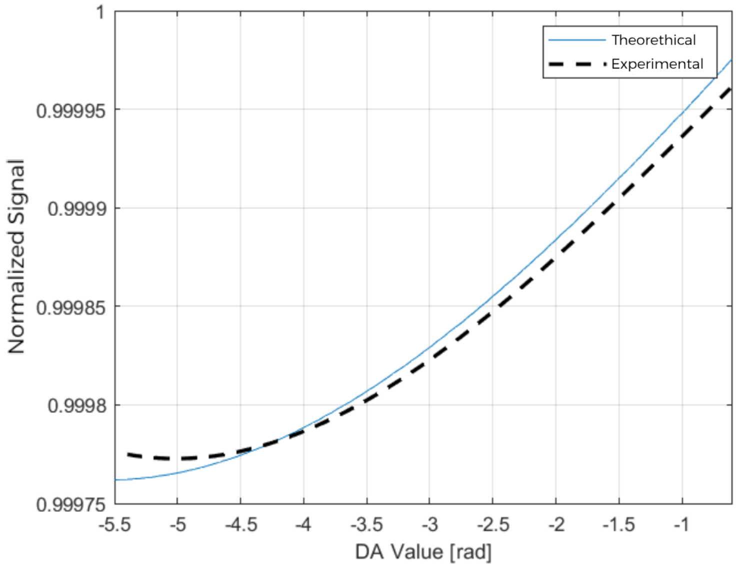

Figure 4.7 – Close-up comparison between experimental and new theoretical model.

It is clear that the resulting factor F and its effect are better represented by this approach, as will be presented below.

4.1.3 Software Compensation

Sections 4.1 and 4.1.2 described how we are able to accurately measure and quantify the optical intensity changes due to the phase modulator applied voltage. This enables us to account for it during acquisition and compensate it via software on the embedded systems runtime. We can use the polynomial fit presented in Figure 4.5 to describe the Intensity Modulation factor with respect to the applied voltage. Since everything is managed on the embedded software, we are able to keep track of the voltage steps and acquired phases while computing the Intensity Modulation modeled factor through the polynomial and using it to compensate for the real one.

As the same electronics can be used to measure the Intensity Modulation curve (Figure 4.1), we foresee a self-calibrating IFOG system with respect to this undesired effect. The overall steps in order to do so are:

- Characterize the Intensity Modulation curve through the ramp method, described at the beginning of Section 4.1;
- Take the obtained curve square root;

- Compute a polynomial fit of sufficient order to describe the signal (in the example it was used 3rd order polynomial fit);
- Follow the model discussed in 4.1.2 to find the compensating factors;
- Multiply the corresponding factor to the acquired sample.

Figures 4.8 and 4.9 show how each phase (P_+ and P_-) of the acquired signal is affected by Intensity Modulation, with and without software compensation of the effect, and the resulting rotation for both scenarios. Each phase is represented by a different color.

Figure 4.9 shows both compensated and uncompensated rotations when the IFOG is sensing Earth's angular speed (around $5.8\ ^\circ/\mathrm{h}$ in the measurement site location). It seems that both plots are superimposed, and that is due to the intensity modulation factor F' contribution to be on the order of $10^{-3}\ \%$, as Figure 4.7 shows.

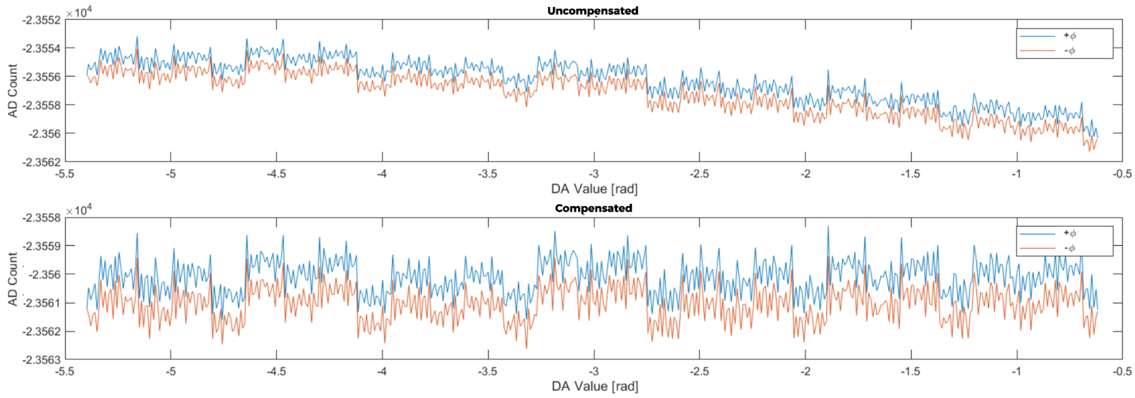

Figure 4.8 – Individual phases (P_+ and P_-) affected by Intensity Modulation. Uncompensated (above) and compensated (below).

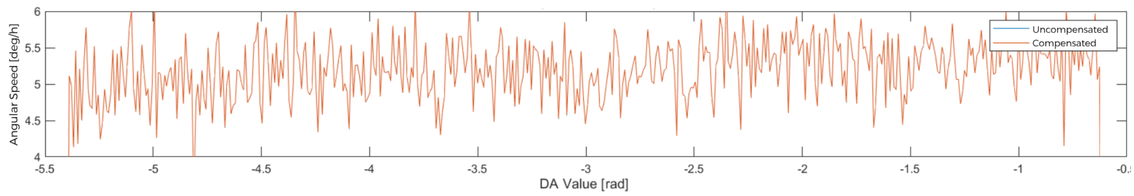

Figure 4.9 – Rotation computed using Figure 4.8 data. Uncompensated (blue) and compensated (red) - superimposed.

When considering an IFOG operating in closed-loop mode, the overall Intensity Modulation contribution to the signal remains as low as for the open-loop analysis depicted above. The only real concern is when the modulator is performing a 2π reset, which can cause two phases to be affected by significantly different factors, leading to an error in the measurement such as the one depicted in Figure 4.4. Since most real-world IFOG navigation applications are set on low-speed environments, resets are expected to be not so frequent between measurements. Even so, one way to avoid this problem is to skip and not use these phases right after resetting when demodulating on the software side.

The same concept applies to the feedback ramp amplitude. If the ramp value becomes high enough, two consecutive phases would also be affected by significantly different factors, leading to the same kind of error on measurements before the 2π reset. However, as the ramp value is proportional to the sensed speed, this is also not expected to happen in most application scenarios.

4.2 IFOG Noise Model Improvements

The current noise model for this kind of IFOG electronics was proposed by [15], who set the foundations by describing the main noise sources on the system, how they combine, and how to translate them into the gyroscope ARW, mainly focusing on the optical and acquisition circuit noises. Furthermore, in this work, we included another source of noise that was not being considered: the modulation circuit. We will start by briefly showing how the modulation circuit noise can affect the output signal, contributing to overall system noise, and then add it to the IFOG Noise-Model. Lastly, we will discuss a series of experiments to validate the proposed model.

As described in Chapter 2, it is clear how phase modulation plays a big part in the IFOG working principle. Given that, the following analysis will be conducted assuming a two-level square-wave modulation, as it was previously established as one of the most effective techniques on our gyroscope while being the basis of this work. However, this analysis can also be applied to IFOGs that employ more than two modulation levels. Moreover, we are also assuming a closed-loop operation.

4.2.1 IFOG Sensibility to Modulation Circuit Noise

Since the modulation circuit outputs a voltage that is proportional to the desired optical signal phase shift, we need to understand how the voltage noise is converted to a modulation error which, in turn, is sensed as a phase shift error. Then, we can convert this to a voltage error that will be read by the acquisition circuit. This noise will be added to the model proposed in [15], allowing us to observe how it impacts the gyroscope ARW. The following Equation (4.3) uses the MIOC half-wave voltage (V_π) to convert voltage noise at the modulation driver output (η_m) to phase-shift noise (η_m).

$$\eta_m\left[\frac{\text{rad}}{\sqrt{\text{Hz}}}\right] = \pi\frac{\eta_m\left[\text{V}/\sqrt{\text{Hz}}\right]}{V_\pi[\text{V}/\pi\ \text{rad}]}. \tag{4.3}$$

Equation 4.3 describes the IFOG modulation phase noise that comes from the modulator circuit. The IFOG response depends on the modulation-induced phase shift, and we can evaluate its voltage output at the acquisition circuit using Equation 4.4, as follows:

$$V_m = R\frac{I_0}{2}[1 + cos(\Delta\phi_s + \phi_m + \phi_R)], \tag{4.4}$$

where R is the TIA resistor value, I_0 is the maximum photocurrent generated by the photodiode (which is dependant on optical source power and photodiode responsivity), $\Delta\phi_s$ is the phase shift due to the Sagnac Effect (proportional to the sensed rotation), ϕ_m is the phase shift induced by the modulator output, and ϕ_R is the phase shift due to the ramp, also coming from the modulator when in closed-loop operation.

Now, since we are making this analysis based on a closed-loop operation, it is reasonable to assume that $\Delta\phi_s + \phi_R \approx 0$. Then, we can find the IFOG sensibility to changes on a single modulation phase (s_{mod}) by differentiating the previous equation with respect to ϕ_m:

$$s_{mod} = \frac{\Delta V_m}{\Delta\phi_m} \approx R\frac{I_0}{2}sin(\phi_m) \quad \left[\frac{\text{V}}{\text{rad}}\right]. \tag{4.5}$$

Finally, we combine equations 4.3 and 4.5 to achieve an equation that translates any noise coming from the modulator driving circuit to a voltage noise that is referred to as acquisition circuit, as shown in Equation 4.6.

$$\eta_M\left[\frac{V}{\sqrt{Hz}}\right] = s_{mod}\cdot\eta_m \quad \left[\frac{\text{V}}{\text{rad}}\right]\left[\frac{\text{rad}}{\sqrt{\text{Hz}}}\right], \tag{4.6}$$

where η_M represents the sum of the modulation circuit noise sources referred to as the acquisition circuit. This enables us to use this term as an additional noise source on Bacurau's model, which already considers the optical and acquisition circuit sources.

Note that the final η_M is also multiplied by $\sqrt{2}$. This is because the modulation noise contributes twice in each modulation step, as the desired phase shift between the light waves is only possible between two modulation steps. Section 2.2.1 explains this dynamic modulation. Finally, the full equation that describes the noise model is:

$$\eta_{\Delta V} = \sqrt{2}\eta_V = \sqrt{2} \cdot \sqrt{(\eta_O^2 + \eta_A^2 + (\sqrt{2}\eta_M)^2)} \quad \left[\frac{\mathrm{V}}{\sqrt{\mathrm{Hz}}}\right], \tag{4.7}$$

where η_O represents the sum of optical noise sources, including *shot noise* and *excess photon noise* from the photodetector; η_A represents the sum of acquisition circuit noise sources, including *thermal noise* from the resistors, analog-to-digital converter *quantization* and *input noise*, and TIA op-amp *voltage* and *current input noise*; η_M represents the sum of modulation circuit noise sources, which will be discussed in the following sub-sections; at last, $\sqrt{2}$ is a term due to the sum of two uncorrelated noise-sources, as the desired signal is calculated from two samples after the two-level square-wave modulation.

Then, we use Equation 4.7 at Bacurau's IFOG noise spectral density to ARW model, shown in Equation 4.8. Here, every source is considered to have a white noise distribution.

$$ARW\left[\frac{deg}{\sqrt{h}}\right] = \frac{10800}{\pi}\frac{\eta_{\Delta V}\ [\mathrm{V}/\sqrt{\mathrm{Hz}}]}{s\ [\mathrm{V/rad}]\ F_s\ [\mathrm{s}]}, \tag{4.8}$$

where F_s is the optical scale factor of the IFOG (as explained on Chapter 2), and s is the IFOG sensibility to small rotations, depicted in Equation 4.9:

$$s = \frac{\Delta V_m}{\Delta \phi_s} \approx R\frac{I_0}{2}\sin\phi_m \quad [\mathrm{V/rad}], \tag{4.9}$$

where I_0 is the maximum photocurrent generated at the photodiode (proportional to the light source power), R is the transimpedance feedback resistor, and ϕ_m is the modulation depth.

4.2.2 Modulation Circuit Noise Sources

As shown in Section 3.1.2.2, the modulation circuit is mainly composed of a DAC and three amplifying stages: two to convert the current output from the DAC to a voltage between ±2.5 V, and a final, fully differential amplifier for a differential voltage output that drives the MIOC. It is important to note that the following analysis will not take into account noise originating from the reference voltage source, as it was considered to be less dominant than the other sources.

Starting on the DAC, *quantization noise* is one of the most dominant noise sources of the circuit, being the noise due to the error in conversion from digitally represented analog values to voltage values. It can be depicted as:

$$DA_Q = \frac{\frac{V_{out}}{2^N}}{\sqrt{12}} \quad (\mathrm{V_{RMS}}), \tag{4.10}$$

where V_{out} is the maximum output voltage of the modulator driver (after every gain stage), and N is the DAC number of bits. Therefore, increasing the resolution of the DAC decreases quantization noise.

Thermal noise is another dominant source on the circuit. On the DAC internal architecture, the R-2R ladder and the feedback resistor are the main contributors to thermal noise, and their values can be found in the device datasheet. Meanwhile, every other resistor that is used to set the gains of the subsequent amplification stages is also contributing to this source. Thermal noise spectral density is depicted as:

$$\eta_{TH} = \sqrt{4kT_kR} \quad \left[\frac{\mathrm{V}}{\sqrt{\mathrm{Hz}}}\right], \tag{4.11}$$

where k is the Boltzmann Constant $(1.380658 \cdot 10^{-23}\mathrm{J/K})$; T_k is the temperature in Kelvin; and R is the resistor value.

Lastly, every op-amp has voltage input noise described in their datasheet, being carried on throughout each subsequent amplifying stage. Those noise sources were also considered in the analysis. Many examples of DAC and op-amp noise modeling can be found in the literature, such as [44, 46, 47]. Finally, the total modulation circuit noise spectral density can be calculated as:

$$\eta_m = \sqrt{\left(\frac{{DA_Q}^2}{\Delta f} + \eta_D^2\right)} \quad \left[\frac{\mathrm{V}}{\sqrt{\mathrm{Hz}}}\right], \tag{4.12}$$

where DA_Q is the DAC quantization noise (in V_{RMS}) and Δf is its operation bandwidth; η_D represents the combination of all electronic noise from the modulation driver circuit, accounting for the different stage amplifications of op-amps input noise and resistors thermal noise. Combining equations 4.12 and 4.3, and then using Equation 4.5, we get the desired value of η_M (resultant noise in the acquisition circuit).

Figures 4.10 and 4.11 show simulation results considering the previous and updated noise-to-ARW model, respectively. It is clear how the modulation circuit noise is being modeled as one of the dominant noise sources in this design. The ARW measured with the experimental setup, with modulation depth equal to $150°$, and using the Allan Variance method is equal to $5.4 \cdot 10^{-4}\ °/\sqrt{\mathrm{h}}$. The theoretical ARW computed through the previous simulation, at the same modulation depth, was $4.3 \cdot 10^{-4}\ °/\sqrt{\mathrm{h}}$, and through the updated simulation was $5.5 \cdot 10^{-4}\ °/\sqrt{\mathrm{h}}$.

It can be seen that, in both noise model simulations, all noise sources reach around the same level of contribution when close to the $150°$ modulation depth. This is due to the major

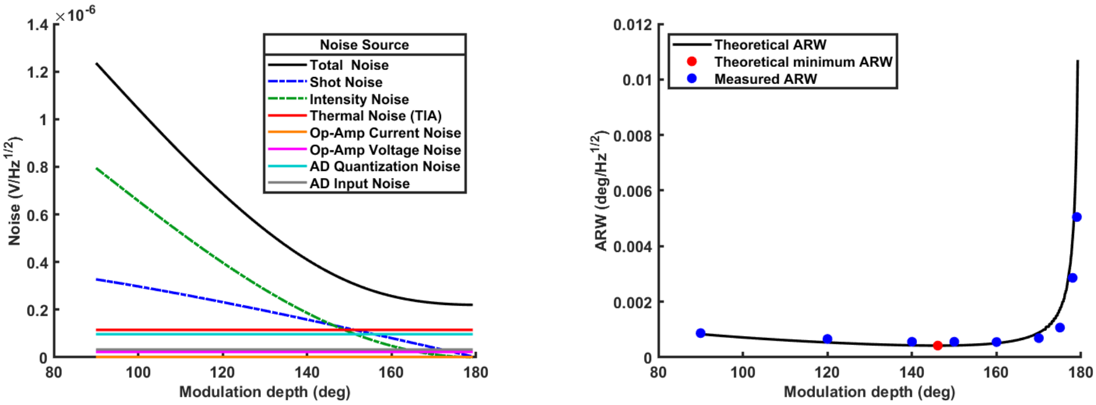

(a) (b)

Figure 4.10 – Noise model simulation before including modulation circuit noises. (a): IFOG Noise Spectral Density with respect to modulation depth. (b): Theoretical and Experimental IFOG ARW comparison.

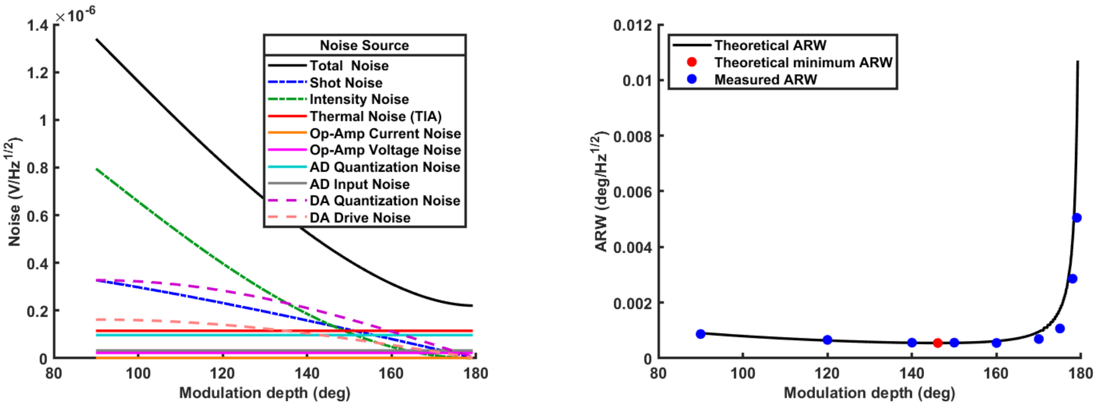

(a) (b)

Figure 4.11 – Noise model simulation after including modulation circuit noises. (a): IFOG Noise Spectral Density with respect to modulation depth. (b): Theoretical and Experimental IFOG ARW comparison.

contributor (optical noise) becoming less relevant as incoming optical power on the photodetector decreases. Therefore, the optimal modulation depth for both cases, depicted as the red marker in Figures 4.10b and 4.11b, is close to $146°$ for both the previous and new model.

Moreover, these simulations show that we can decrease the gyroscope ARW by increasing the optical source power, while also increasing the modulation depth. As optical power increases, SNR will improve with respect to shot noise (Section 2.4.2), and the optical noise will predominate further with respect to the other noise sources. Then, the optimal modulation depth should move closer to $180°$.

Finally, one should notice that the new model (Figure 4.11) shows that theoretical ARW values are higher than the experimentally obtained ones. This indicates that the approach taken to describe the modulator circuit noise is not entirely correct. To investigate and understand the cause of this behavior, experiments that are described in the next section were performed. As it will be shown, this disparity between model and experimental data is due to the fact that not every noise source is accurately described as a white noise source.

4.2.3 Modulation Circuit Noise Analysis

To assess the modulation circuit noise behavior, an experiment consisting of truncating DAC bits was done, and it shows that it takes a significant amount of truncated bits to affect the IFOG ARW. Modulation depth was kept at $150°$. This is an unexpected result when looking at the noise model that includes DA quantization noise (Figure 4.11), as for each reduced bit the quantization noise should be doubled, as Equation 4.10 shows. The analysis presented in Figure 4.11 indicates that DAC quantization noise should predominate over the other sources at this modulation depth.

Table 4.1 – IFOG ARW when zeroing DAC bits.

DAC number of bits	ARW $°/\sqrt{\mathrm{h}}$
16	0.00054
15	0.00054
14	0.00054
13	0.00054
12	0.00055
11	0.00055
10	0.00061
9	0.00079
8	0.00129

These results show that noise in the modulation chain of the IFOG system must be addressed in a different manner from those directly in the system acquisition chain. In fact, we can see through a discrete closed-loop IFOG model (adapted from [45]), depicted in Figure 4.12, where the modulation noise sources are introduced in the signal chain.

Figure 4.12 model represents the IFOG sensing rotational speed as the input $X(z)$, and the interferometer's optical scale factor as the proportional gain K_s. Then, the signal representing the interferometer's response on closed-loop $E(z)$ goes through the acquisition signal chain. K_{pd} represents the photodiode responsivity and the TIA gain that converts $E(z)$ into volts, and the ADC acquisition is the proportional lag unit $K_{AD}Z^{-1}$. Lastly, $D(z)$ is the angular rate demodulation integrator, that outputs the sensor signal $Y(z)$.

The feedback loop represents the staircase wave ramp generator as the integrator, followed by a proportional lag $K_{DA}Z^{-1}$ unit representing the modulator driving circuit, and, finally, the phase modulator (MIOC) is represented by a proportional differential unit $K_Y(1 - Z^{-1})$.

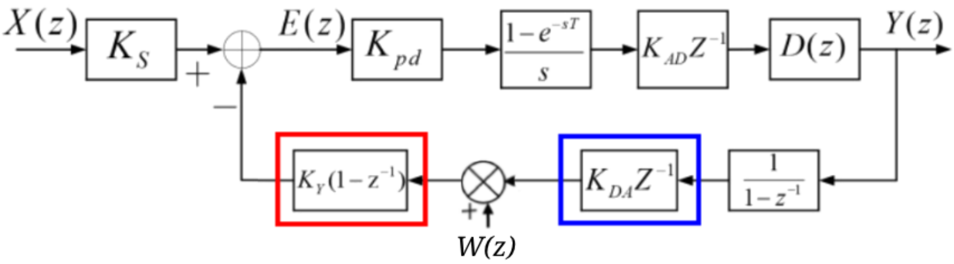

Figure 4.12 – Discrete closed-loop IFOG model. The blue block represents the modulator driver. The red block represents the MIOC as a proportional differential unit.

Electronic noise (including quantization noise) in the modulation circuit driver is introduced between the red and blue blocks (signal $W(z)$), as they are at the output of the modulator driver circuit. With this, the noise at this output gets differentiated before being added to the other noises in the acquisition chain, which causes a "noise shaping" effect. For white noise, this leads to a noise spectrum that rises with high frequency (known as "purple" or "violet" noise), depicted in Figure 4.13.

In our IFOG implementation, the signal is sampled at approximately 74 kHz, then multiple samples are averaged, bringing the sampling bandwidth down closer to 1 kHz, and the signal is further processed through a digital lowpass filter. This leads to a low contribution of the modulation circuit noise over the gyroscope output, as most of the noise power is contained in the high frequencies of the spectrum that were cut from the signal of interest.

An experiment was carried out to assess this "noise shaping" behavior in the data outputted by the IFOG system. Data was acquired in closed-loop operation with a modulation depth of $150°$, using a two-level two-stage modulation scheme, with a lowpass filter of approximately 300 Hz. The DAC was truncated to a different number of bits to increase its quantization noise, and the measurement spectral density was monitored. Figure 4.14 shows the results from this experiment, and it can be seen that, when the modulation circuit noise is sufficiently high, a slope appears in the data spectrum analysis (Figure 4.14b).

Another approach that leads to the conclusion of the small contribution from the modulation circuit noise comes from Lefèvre [5]. He claims that "phase defects" generated by

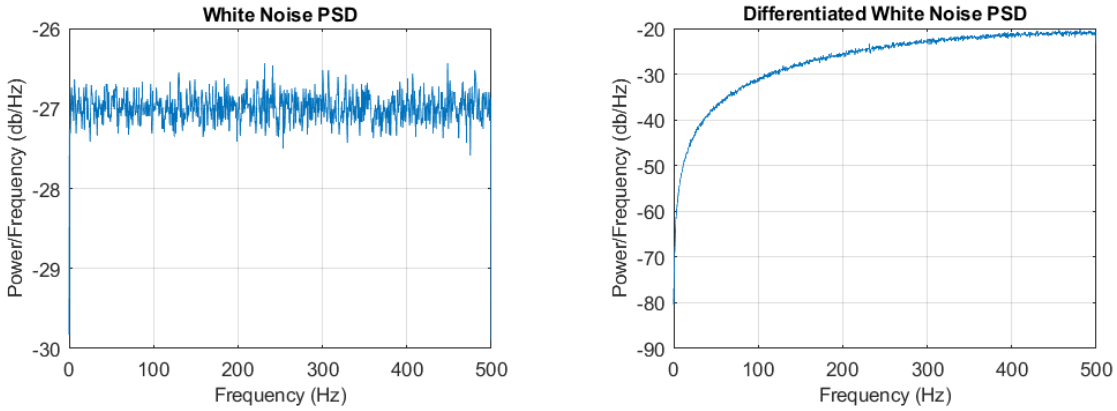

(a) (b)

Figure 4.13 – Noise shaping process simulation. (a): White noise spectrum. (b): Differentiated white noise spectrum.

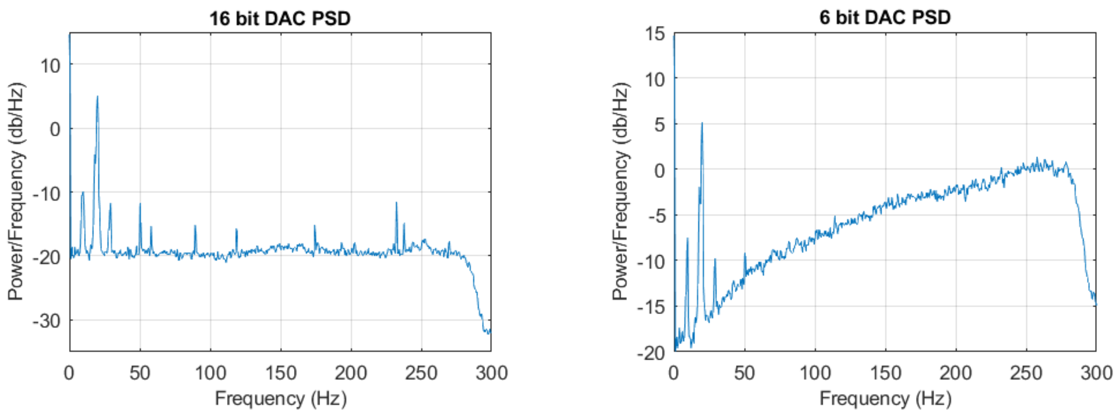

(a) (b)

Figure 4.14 – Noise shaping process experiment. (a): 16 bit DAC data. (b): 6 bit DAC data.

the modulation driver are canceled out during the IFOG phase modulation process. Below, we will present an analysis based on this assertion that enables us to account for a noise reduction factor in our noise model.

The dynamic phase modulation is the process responsible for generating the optical phase difference that causes the IFOG output signal to behave like Figure 4.15 when a two-level modulation is employed. The phase difference that corresponds to each of the voltage levels at the TIA output signal is obtained through the difference between two phase steps on the modulator, delayed of a propagation time τ.

$$\Delta\phi_M = \phi_{m(\tau)} - \phi_{m(\tau+1)}. \tag{4.13}$$

We can think of any modulation phase difference $\Delta\phi_M$ as a sum of an ideal phase step ϕ_i and a phase defect (or error) due to noise ϕ_d. Then, the phase difference can be described

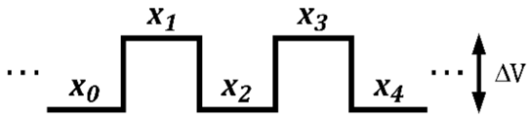

Figure 4.15 – Signal outputted by the IFOG acquisition circuit during two-level square-wave modulation.

as:

$$\Delta\phi_M = \Delta\phi_i + \Delta\phi_d. \tag{4.14}$$

Finally, as with any phase modulation, the noisy phase difference is given through the delay of τ due to the interferometer. Hence:

$$\Delta\phi_d = \phi_{d(\tau)} - \phi_{d(\tau+1)}. \tag{4.15}$$

In operation, the IFOG output signal is averaged over N samples at the embedded system firmware. In order to get a signal level change (such as x_n in Figure 4.15), phase difference between two modulation steps is required. Therefore, in order to compute N samples of the desired output (which is the difference between x_n and x_{n+1} in Figure 4.15), the light waves have to go through the phase modulator in $2N$ different modulation states, due the dynamic modulation. Thus, the average phase defect is given by:

$$\begin{aligned} < \Delta\phi_d >&= \frac{[(\phi_{d(\tau)} - \phi_{d(\tau+1)}) + (\phi_{d(\tau+1)} - \phi_{d(\tau+2)}) + ... + (\phi_{d(\tau+N-2)} - \phi_{d(\tau+N-1)}) + (\phi_{d(\tau+N-1)} - 0)]}{2N} \\ < \Delta\phi_d >&= \frac{\phi_{d(\tau)}}{2N}. \end{aligned} \tag{4.16}$$

The modulation noise distribution can be estimated by evaluating the standard deviation of the modulation defect:

$$Var(< \Delta\phi_d >) = \frac{(\sigma_m)^2}{4N^2}. \tag{4.17}$$

$$Std(< \Delta\phi_d >) = \frac{(\sigma_m)}{2N}. \tag{4.18}$$

Here, we can see that, due to the interferometer delay, most of the phase defects due to noise $\phi_{d(\tau+i)}$ will cancel out over the averaging process. This renders a final noise distribution that has its amplitude divided by a factor of N. The noise spectral density can be computed by dividing the resulting standard deviation by the averaged signal Nyquist bandwidth B.

However, this last approach has to be validated as well, experimentally or through simulation. Future works with respect to this are expected, as this should enable modulation circuit noises to be accounted for in our noise-to-ARW model. Finally, it can be concluded from both the "noise shaping" and the Lefèvre approaches that in typical IFOG implementations, in which high bandwidth is not a concern, lower resolution DACs can be employed for phase modulation.

In the next section, we will present experimental validation for the other electronic noise sources as well as the optical ones. Unlike modulation noise, these sources are directly at the acquisition signal chain and are not affected by the modulator noise shaping process. Hence, it is reasonable to assume that their white noise distribution approximation holds valid for most of these sources.

4.2.4 Validating the Noise Model

In order to validate the theoretical noise model, we propose a series of experiments to compare the behavior of each noise source with respect to the model, analyzing each one separately, when possible. We will use the IFOG embedded system to evaluate the voltage noise at the output of the acquisition circuit, as each sample obtained represents a digitized voltage signal that contains this noise.

To estimate the overall noise contribution, we compute the root-mean-square (RMS) value of the AC component of the sampled signal over a window of 3 s during acquisition on the embedded system. In order to evaluate only the AC component, we subtract from the computed RMS value the signal average over the same window (an estimate of the DC component).

Then, the final RMS value provides a measurement of the AC amplitude over the signal - considering that after demodulation, most of the noise in the output is white noise [15]. Therefore, this measurement represents an approximation to the mean noise value distributed across the bandwidth of the desired signal. Finally, with the white noise assumption, the noise spectral density of the measurement can be computed by dividing the RMS value by the acquisition bandwidth. RMS is computed through:

$$RMS(x[n]) = \sqrt{\frac{1}{N}\sum_{n} x^2[n]}, \tag{4.19}$$

where $x[n]$ represents the discrete data array over which the RMS value is being computed, and N is the total number of samples used to compute it.

In the following subsections, we will present preliminary results of our investigations on ADC noise, overall noise on the acquisition circuit, and insights on our modulation circuit noise modeling. The IFOG embedded system itself will be used to evaluate the different noise sources' behavior. The main goal is to verify, correct, and validate the proposed noise model, by validating the noise sources (or group of noise sources) independently. Lastly, every set of measurements was done using the previous PCB design except when otherwise mentioned.

4.2.4.1 RMS to ARW Conversion

Firstly, we will evaluate how well the RMS computed through the embedded system describes the sensor ARW. To assess this, we measured the RMS value of the output on different modulation depths, with the gyroscope on a stationary workbench, only sensing Earth's rotation. Then, we converted RMS to noise spectral density by dividing the computed value by the acquired signal bandwidth. In this experiment, the signal was processed through a digital lowpass filter with a 5 Hz cutoff frequency. Figure 4.16 depicts the result of this experiment, after converting the RMS to ARW.

The ARW value computed through this experiment, for a modulation depth of $150°$, is equal to $5.2 \cdot 10^{-4}\ °/\sqrt{\mathrm{h}}$, comparable to the $5.4 \cdot 10^{-4}\ °/\sqrt{\mathrm{h}}$ measured through the Allan Variance method. With this, we can conclude that measuring the RMS value is, in fact, a reasonable approximation to overall system noise and use it for the noise-model evaluation.

4.2.4.2 ADC Quantization Noise

It can be seen through the noise model simulation Figures (4.10 and 4.11) that the ADC quantization noise is one of the most dominant noise sources. According to the employed ADC datasheet, this converter should be able to provide up to 16 noise-free bits under ideal conditions [43]. This can be affected by many external sources, such as voltage reference noise, clock jittering, power supply noise, and poor PCB design [48].

A usual experiment to verify this parameter is to short-circuit the ADC inputs and monitor its output code in software. This will quantify the ADC internal noise during conversion. The output code should be stable up until a specific number of bits, meaning that they are

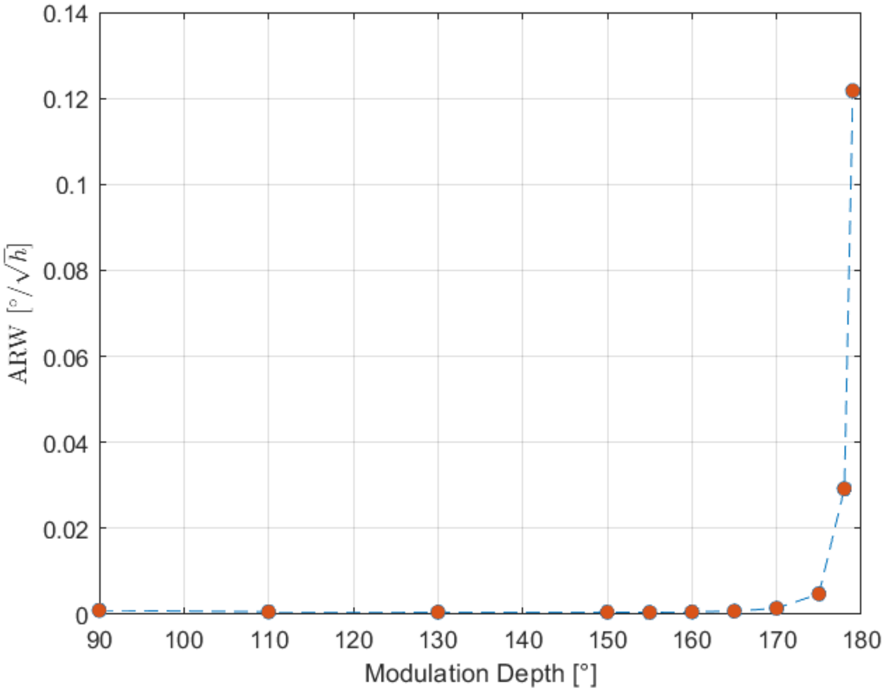

Figure 4.16 – Experimental RMS noise evaluation. Converted IFOG output signal RMS to ARW in respect to modulation depth.

unaffected by peak-to-peak noise, and those are the noise-free bits. This experiment was done to test our design. It was noticed that the number of noise-free bits was, in fact, 15 bits; one less than the datasheet specification. This means that there are improvements to be made to the PCB design, as the noise floor at the ADC input is higher than expected.

To assess the degrading effects of a lower-resolution AD converter, an experiment was done by truncating, via software, the ADC bits. The modulation depth was kept at $150°$ and the sensor ARW was monitored. The results from this experiment are shown in Table 4.2. It can be seen that minimal changes occur until 15 bits. This can be explained by the higher-than-expected AD input noise predominating over quantization noise, as the free noise resolution is, in fact, 15 bits. This table also shows the ARW estimate from the noise-to-ARW model simulation.

Table 4.2 – IFOG ARW when truncating ADC bits.

ADC number of bits	**ARW** $^\circ/\sqrt{\mathrm{h}}$	**ARW Estimate** $^\circ/\sqrt{\mathrm{h}}$
16	0.00054	0.00042
15	0.00055	0.00054
14	0.00066	0.00084
13	0.00092	0.00150
12	0.00173	0.00300

It can be noted that the error between the experimental ARW and the model estimate increases as the number of truncated bits gets higher. This indicates that modeling quantization noise as a white noise source is not completely accurate.

4.2.4.3 Overall Electronic Noise

In order to investigate noise at the acquisition circuit, we kept the optical source powered off, maintaining the photodiode connected to the circuit input, allowing us to measure the amplifier circuit noise at the ADC. Following the noise model simulation results, the feedback resistor thermal noise is the highest contributor noise source at the acquisition circuit, along with ADC quantization noise. Therefore, we were able to increase the feedback resistor (R_f) value at the TIA while monitoring the output to analyze the acquisition circuit's electronic noise behavior.

With the optical source powered off, the embedded firmware was programmed to sample data in the same manner as in the IFOG operation condition, with a sampling frequency of approximately 1 kHz, applying a 5 Hz low-pass filter. Data was acquired for distinct TIA resistors values ($33\ \text{k}\Omega$, $100\ \text{k}\Omega$, $220\ \text{k}\Omega$), therefore with different expected thermal noise contributions. The RMS value of the measured voltage was computed, and the result was divided by the square root of the corresponding signal bandwidth to compute the approximate noise spectral density value. This bandwidth was considered to be equal to the digital filter cutoff frequency (5 Hz).

To ensure that the RMS value is correctly computed and that it is a reasonable representation of the noise power in the acquired signal, this value was compared to the square root of the signal's power spectral density (PSD) integral. It was noted that the relative difference between both results was in the order of 0.03%, meaning that, in fact, the computed RMS is a good representation of the noise over the acquired signal.

Finally, to ensure that most of the noise power is comprehended in the filter bandwidth, it was found through the PSD that the bandwidth interval that contains 99% of the signal power is from 0 to 5.8 Hz, approximately. Figure 4.17, below, depicts this.

Table 4.3 shows the comparison between the expected theoretical and experimentally obtained values for different feedback resistor values. Theoretical noise is computed as the sum of thermal noise (from the feedback resistor), ADC quantization noise, and op-amp voltage and current noises, following the model used to compute the simulation.

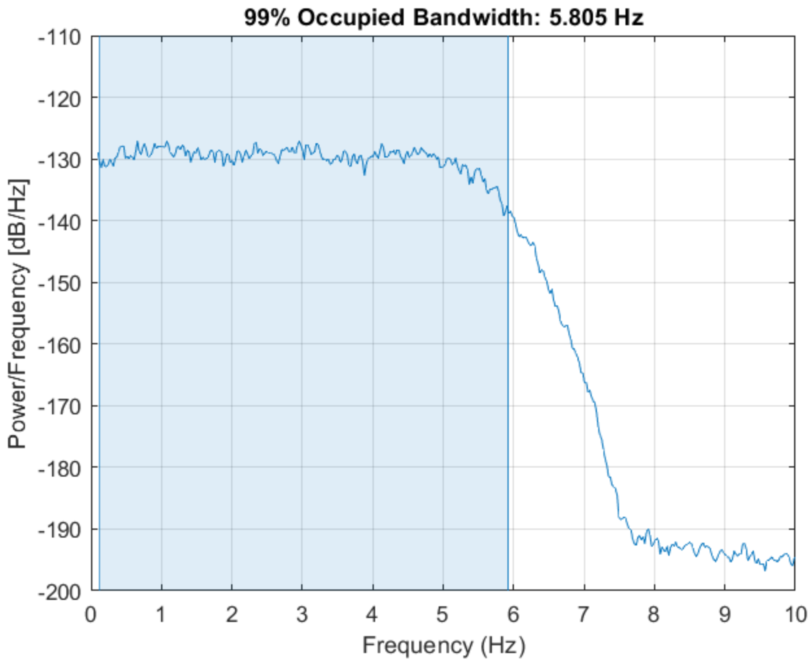

Figure 4.17 – Example of the Power Spectral Density (PSD) of a signal. The highlighted area contains 99% of the signal power. X axis ranges from 0 to 50 Hz (Nyquist Frequency), but is limited to 10 Hz to aid visualization.

Table 4.3 – Electronic Noise Spectral Density (previous PCB design).

TIA Resistor Values [Ω]	33 k	100 k	220 k
Experimental [$\mu\mathrm{V}/\sqrt{\mathrm{Hz}}$]	0.184	0.256	0.358
Theoretical [$\mu\mathrm{V}/\sqrt{\mathrm{Hz}}$]	0.176	0.218	0.283
Experimental/Theoretical	1.046	1.164	1.265

In the employed IFOG implementation, a $100\ \mathrm{k}\Omega$ feedback resistor is employed. In this experiment, higher resistor values were employed in order for the thermal noise to predominate over the other electronic noise sources (ADC quantization and op-amp noises). Results show that electronic noise is well described by our noise model, however, it can be noticed that the error between the model and experimental data rises as we increase the TIA resistor (R_f) value.

The same experiment was repeated with the new PCB design and the results are shown in Table 4.4. Comparing these results with the previous PCB design shows that the overall electronic noise in the acquisition circuit is slightly higher in the new design. Moreover, it can be noted by analyzing Figure 4.10 that, when electronic noise predominates, increasing it should lead to a proportional ARW increase.

The overall increase in electronic noise can be explained by: (1) sub-optimal PCB layout; (2) lack of power supply filtering on the analog board, as the supply rails are only filtered at the connector input in the digital board. These are the most likely causes, as the components employed to assemble the new PCBs are the same as those used in the previous design assembly.

Table 4.4 – Electronic Noise Spectral Density (new PCB design).

TIA Resistor Value [Ω]	100 k
New PCB 1 [μV/$\sqrt{\text{Hz}}$]	0.368
New PCB 2 [μV/$\sqrt{\text{Hz}}$]	0.325

The relative electronic noise increase with respect to the previous design (for the same R_f value) is approximately 1.44 (1.27 for the second board). Hence, the relative increase in ARW should be around the same, yielding $7.7 \cdot 10^{-4}$ $^\circ/\sqrt{\text{h}}$ (and $6.8 \cdot 10^{-4}$ $^\circ/\sqrt{\text{h}}$). Table 3.3 shows that experimental data exhibits a slightly higher ARW value when compared to the aforementioned theoretical analysis. This small difference between theoretical and experimentally obtained data is expected to be caused by external interferences, as data was acquired with the IFOG in a non-ideal environment. As the optical assembly is the same in all tests, optical noise contribution is expected to remain equal.

4.2.4.4 Optical Noise

In order to measure optical noise (shot and intensity noise), the same IFOG acquisition circuit was used, meaning that electronic noises cannot be separated from the optical noises on the acquired signal. Nevertheless, optical noise dominates over electronic noise when the optical power is sufficiently high, as discussed in Chapters 2 and 4. Arriving optical power at the photodetector can be varied by changing the modulation depth of the IFOG square wave modulation scheme.

Therefore, the same methodology from the electronic noise measurements was repeated. The optical source was powered on, and the feedback resistor of the TIA was kept the same throughout all of the measurements, with the corresponding value of $33\ \text{k}\Omega$, in order to avoid voltage saturation of the acquisition circuit op-amp. Modulation depth was set to different values in order to achieve distinct optical powers and, therefore, overall signal noise.

Theoretical noise is computed as the sum of optical shot and intensity noise, and electronic thermal, AD quantization, and op-amp noises. Table 4.5 compares both theoretically computed and experimentally obtained noise spectral density for different modulation depths.

It is noticeable that experimentally obtained results are higher than the theoretically computed ones and that the error between the model and experimental data increases with mod-

Table 4.5 – Optical Spectral Noise Density Comparison.

Modulation Depth [deg]	10	30	40	50
Optical Power [μW]	18.46	17.35	16.42	15.28
Experimental [$\mu V/\sqrt{Hz}$]	0.963	0.921	0.910	0.875
Theoretical [$\mu V/\sqrt{Hz}$]	0.807	0.763	0.726	0.680
Experimental/Theoretical	1.19	1.21	1.25	1.28

ulation depth. The latter is expected as sensitivity is also being increased (for ϕ_M between $0°$ and $90°$), and data was acquired through the interferometer, therefore, the resulting signal is more susceptible to external interference.

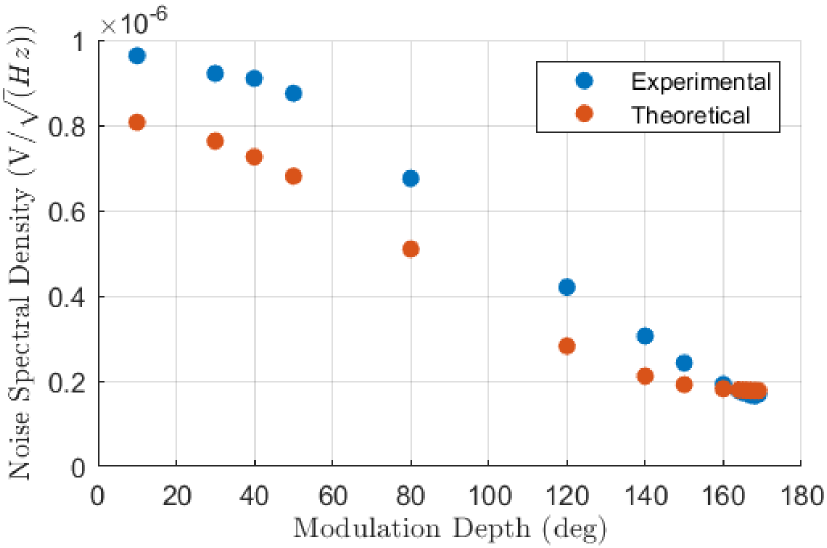

Figure 4.18 – Optical noise data. Experimental and theoretical optical noise spectral density with respect to modulation depth.

Figure 4.18 depicts optical noise spectral density behavior with respect to the modulation depth for $0 < \phi_M < 180°$. It is noticeable that the error between experimental and theoretical computed values increases as the system sensitivity is increased, and decreases as modulation depth is sufficiently high. When electronic noise sources overcome the optical ones and become the main contributor (ϕ_M between $160°$ and $170°$), the relative error is minimal, indicating that electronic noise is well estimated. This result, along with the low disparity between the theoretical and measured ARW, shown in Figure 4.10b, indicates that optical noise is underestimated in our model. One possible cause is that the optical noises model used in our simulation may be slightly different depending on the light source used and the degree of polarization [49].

In conclusion, the experimental ARW data shows similar behavior to the theoretical model, which indicates that the model is describing well the gyroscope ARW, even though it is not completely accurate. Both results from the electronic and optical noise validation show that they are underestimated in the theoretical analysis. To further investigate how small changes to our modeled noise sources' spectral density values alter our model, we present in Appendix B an interactive application that allows for real-time corrections and assessment of the main noise contributors' effects on the IFOG ARW.

4.3 Chapter Round-Up

In this chapter, we have seen a new approach to the Intensity Modulation problem. An improved explanation of the phenomenon was provided, as well as a solution and software routine to compensate for it. Moreover, we discussed how the modulation circuit voltage noise is seen at the acquisition circuit after affecting the optical signal, and why it has to be addressed in a different manner than other noise sources. Finally, experimental validation and discussion over some of the most relevant characteristics of the noise model were provided, including the voltage noise to ARW conversion, acquisition circuit noise, and optical noises.

5 CONCLUSIONS AND FUTURE PERSPECTIVES

We have come a long way since the ancient seafarers who relied on celestial observations and external references to be able to find orientation and navigate. Nowadays, advanced sensors to track position, speed, and acceleration, such as accelerometers and gyroscopes, enable us to embed a self-contained inertial navigation system (INS) that is capable of performing this task. Still, the need for better-performing sensors (mostly gyroscopes) capable of continuously keeping accurate track for longer periods is of great interest to the community. In particular, the development of this kind of sensor in our country (Brazil) has become mandatory to establish independence in terms of military and aerospace dominance. To this end, this project has a more practical character, in which we aimed for a novel design, better suited for INS applications, investigated through a new approach a phase modulator (MIOC) intrinsic issue, and discussed improvements over a general noise model for IFOGs that can be used for further design enhancements.

From a technical point of view, this work presented design fundamentals, construction guidelines, and a novel instrumentation project that provides great insight into all-digital IFOG embedded system implementations, particularly of the one developed in this work. All of these combined are of great value to support further investigations from our research group. The presented final design is modular and has multi-axis sensing capabilities through a single processing unit. Through careful component selection and PCB design techniques, this novel design is still among the top-performing grades for this kind of sensor, achieving an ARW of $7.0 \cdot 10^{-4}\ ^\circ/\sqrt{\mathrm{h}}$.

Employing a modern microcontroller along with advanced peripheral usage techniques in its firmware programming are key aspects that enable this design approach, as minimal processing unit workload is required. This upgrade also eases maintenance and better supports future developments when compared to the previous project. With a better ADC, the new design has an 34% faster conversion time, meaning it can sample gyroscopes with lower propagation time (less optical fiber length), which allows for a more compact structure. Also, the higher modulation voltage span enables closed-loop operation at higher speeds before 2π resetting becomes too frequent (which degrades performance), improving the sensor's full-scale range.

Although designed, the new electronic project has yet to be fully tested. The shortage in electronic components availability due to the recent COVID-19 pandemic, combined with delays in international import processes and shipping, prevented the manufacturing completion. Even so, we were able to salvage components from previous versions of PCBs and assemble two different sets of the new design, testing the embedded firmware to most of its extent. Future works should be easily able to implement and experiment with the full multi-axis assembly, given the already developed firmware from this work.

We've also investigated a performance degrading effect intrinsic to $LiNbO_3$ phase modulator constructions that, to the best of our knowledge, is relatively unaddressed in the literature. A deep understanding of the IFOG dynamic modulation scheme made possible the measurement and quantification of the Intensity Modulation effect. We propose a novel approach to identify and compensate for this effect that differs from literature mainstream approaches as it allows for a self-calibrating system that does not require external characterization of the phase modulator, relying on the IFOG acquisition circuit itself, and can be implemented on already existing IFOG systems as a firmware update. Our approach has been tested through simulation (with real data) and shows great potential to address this problem.

Finally, we presented validation and discussion on improvements on our IFOG noise-to-ARW model. It is clear that being able to accurately describe the major noise contributors of this system is a trending topic in the literature, as it is mandatory to push its performance even further. To this extent, we have modeled how modulation circuit electronic noise sources contribute towards degrading the gyroscope performance. We concluded that it has to be addressed in a different manner than the other contributors of the system, as the noise is "shaped" into high frequencies. To the best of our knowledge, none of the literature has presented the modulation noise source contribution nor an analysis of its behavior on the system.

We've also experimentally measured the major electronic and optical noise sources of our IFOG, comparing the absolute noise spectral density values with the theoretical modeled ones. These results allowed us to conclude that electronic noise is better estimated than optical noise. Still, our noise-to-ARW model presents a good estimate of the noise contributors and theoretical ARW, allowing for bottleneck assessment in terms of overall system design. From this model, we can also estimate the optimal modulation depth that minimizes the ARW, as well as its improvement with increasing optical source power. Thus, it is clear that the noise model provides a useful tool for improving IFOGs design, and validating as well as improving it is of great value to future research.

Nevertheless, we believe that instrumentation is a long-term, iterative task. Hence, the system documentation and techniques description provide a solid basis for future developments and experiments. In the future, we hope to see the extent of an optimized IFOG system fully developed in national territory and its application on high-end inertial navigation systems. The implementation of the multi-axis design should aid the development in this direction.

BIBLIOGRAPHY

1 AUBET, M. E. **The Phoenicians and the West Politics - Colonies and Trade**. 2nd. ed. [S.l.]: Cambridge University Press, 1987. ISBN 0521795435.

2 SZáZ, D.; HORVáTH, G. Success of sky-polarimetric viking navigation: Revealing the chance viking sailors could reach greenland from norway. **Royal Society Open Science**, Royal Society Publishing, v. 5, 4 2018. ISSN 20545703.

3 SONG, N.; XU, X.; ZHANG, Z.; GAO, F.; WANG, X. Advanced interferometric fiber optic gyroscope for inertial sensing: A review. **Journal of Lightwave Technology**, Institute of Electrical and Electronics Engineers Inc., 2023. ISSN 15582213.

4 PASSARO, V. M.; CUCCOVILLO, A.; VAIANI, L.; CARLO, M. D.; CAMPANELLA, C. E. Gyroscope technology and applications: A review in the industrial perspective. **Sensors (Switzerland)**, MDPI AG, v. 17, 10 2017. ISSN 14248220.

5 LEFEVRE, H. C. **The Fiber-Optic Gyroscope**. 3rd. ed. [S.l.: s.n.], 2022. ISBN 9781630818623.

6 ARMENISE, M. N.; CIMINELLI, C.; DELL'OLIO, F.; PASSARO, V. M. **Advances in gyroscope technologies**. [S.l.]: Springer-Verlag Berlin Heidelberg, 2010. v. 9783642154935. 1-117 p. ISBN 9783642154942.

7 SILVEIRA, V. **Laboratório reduz gargalo espacial**. 2011.

8 MENDELSON, J.; VINCENT, F.; RYAN, S. G.; BANDER, F. A.; COOK, T.; NELSON, A. J. **Toward the Heavens Latin America's Emerging Space Programs A Report of the CSIS Americas Program and Space Initiatives**. 2009.

9 ALMEIDA, J. C. J.

Técnicas de Processamento de Sinais em Girômetros a Fibra Óptica para Sistemas de Navegação Inercial, 1996.

10 RODRIGUEZ, R. B. G.

Uma Nova Técnica de Detecção de Sinais de Girósco pio a Fibra Óptica usando "Zero crossing" com Clock Síncrono, 1999.

11 FERREIRA, E. C.

Nova Técnica de Processamento de Sinais de Girômetro a Fibra Óptica para Sistemas de Navegação Inercial, 2001.

12 WATANABE, R. H.

Estudo e compensação da deriva térmica, estabilidade do fator de escala e linearização de um circuito de condicionamento e processamento de sinais de girômetro interferométrico a fibra óptica, 2009.

13 MELO, F. F.

Estudo e Projeto de um Sistema Eletrônico de Processamento de Sinais de Girômetros a Fibra Óptica com Modulação Dinâmica., 2009.

14 SPENGLER, A. W.

Técnica de condicionamento e processamento de sinais para girômetros a fibra óptica com malha fechada óptica, 2014.

15 BACURAU, R. M.

Projeto e Implementação de um Sistema Eletronico para Giroscópios Interferométricos a Fibra Óptica de Malha Fechada, 2016.

16 SAGNAC, G. L'ether lumineux demontre par l'effet du vent relatif d'ether dans un interferometre en rotation uniforme. **Proceedings of the USSR Academy of Sciences**, v. 157, p. 708–710, 1913.

17 VALI, V.; SHORTHILL, R. W. Fiber ring interferometer. **Appl. Opt.**, Optica Publishing Group, v. 15, p. 1099–1100, 5 1976. Disponível em: <https://opg.optica.org/ao/abstract.cfm?URI=ao-15-5-1099>.

18 MICHELSON, A. A.; GALE, H. G. The effect of the earth's rotation on the velocity of light. **Nature**, v. 115, p. 566, 1925. ISSN 1476-4687. Disponível em: <https://doi.org/10.1038/115566a0>.

19 CHEN, C.-L. **Foundations for Guided-Wave Optics**. [S.l.: s.n.], 2005. ISBN 9780471756873.

20 LEFEVRE, H. C.; BERGH, R. A.; SHAW, H. J. All-fiber gyroscope with inertial-navigation short-term sensitivity. **Opt. Lett.**, Optica Publishing Group, v. 7, p. 454–456, 9 1982. Disponível em: <https://opg.optica.org/ol/abstract.cfm?URI=ol-7-9-454>.

21 LEFEVRE, H. C.; GRAINDORGE, P.; ARDITTY, H. J.; VATOUX, S.; PAPUCHON, M. Double closed-loop hybrid fiber gyroscope using digital phase ramp. In: . Optica Publishing Group, 1985. p. PDS7. Disponível em: <https://opg.optica.org/abstract.cfm?URI=OFS-1985-PDS7>.

22 LEFEVRE, H. C.; MARTIN, P.; GAIFFE, T. P.; GRAINDORGE, P.; BOUDEC, G. L.; MORISSE, J.; SIMONPIETRI, P.; TAUFFLIEB, E. M.; VIVENOT, P.; ARDITTI, H. J. Latest advances in fiber optic gyroscope technology at photonetics. In: DEPAULA, R. P. (Ed.). SPIE, 1994. v. 2292, p. 156 – 165. Disponível em: <https://doi.org/10.1117/12.191830>.

23 WANG, W.; WANG, J.; ZHAO, Z. Method to control the gain in modulation chain of closed-loop fiber optic gyroscope with periodical biasing modulation. **Optical Engineering**, v. 51, p. 4401, 6 2012.

24 CHEN, S.; CHENG, J.; GAO, W. A phase modulation method for improving the scale factor stability of fiber-optic gyroscope. In: . [S.l.: s.n.], 2008. p. 37–42.

25 IEEE Standard Specification Format Guide and Test Procedure for Single-Axis Interferometric Fiber Optic Gyros. **IEEE Std 952-1997**, p. 1–84, 1998.

26 ALLAN, D. W. Statistics of atomic frequency standards. **Proceedings of the IEEE**, v. 54, p. 221–230, 1966.

27 LIU, J.; ZHANG, C.; ZHENG, Y.; SONG, J.; GAO, F.; YANG, D. Suppression of nonlinear residual intensity modulation in multifunction integrated optic circuit for fiber-optic gyroscopes. **Journal of Lightwave Technology**, Institute of Electrical and Electronics Engineers Inc., v. 38, p. 1572–1579, 3 2020. ISSN 15582213.

28 WANG, D.-Y.; SHENG, F. Residuary intensity modulation of the phase modulator in ifog and its measurement. v. 34, p. 26–29, 6 2007.

29 POGORELAYA, D. A.; SMOLOVIK, M. A.; STRIGALEV, V. E.; ALEYNIK, A. S.; DEYNEKA, I. G. An investigation of the influence of residual amplitude modulation in phase electro-optic modulator on the signal of fiber-optic gyroscope. In: . [S.l.]: Institute of Physics Publishing, 2016. v. 735. ISSN 17426596.

30 TRIPATHI, U. S.; DIXIT, N.; KAUL, A. N.; GUPTA, A. K. **Multifunction Integrated Optic Chip for FOG**. 2007.

31 ZHANG, C.; LIU, J.; ZHANG, Z.; ZHENG, Y.; XU, X.; SONG, J. Analysis of the influence of residual intensity modulation in the multifunction integrated optic circuit on fiber-optic gyroscopes performance. **IEEE Sensors Journal**, Institute of Electrical and Electronics Engineers Inc., 2021. ISSN 15581748.

32 KANTSIPER, B. L.; RAY, J. C.; HUNT, J. W.; STRIKWERDA, T. E. **Autonomous Avoidance of Structural Resonances on the STEREO Mission**. 2007.

33 PATUREL, Y.; HONTHAAS, J.; LEFèVRE, H.; NAPOLITANO, F. One nautical mile per month fog-based strapdown inertial navigation system: A dream already within reach? **Gyroscopy and Navigation**, v. 5, p. 1–8, 1 2014. ISSN 20751087.

34 GU, H.; LI, S.; WANG, F.; ZHANG, H. Random noise study of the digital closed-loop fiber optic gyroscope. In: . [S.l.]: SPIE, 2013. v. 8914, p. 891402. ISBN 9780819497833. ISSN 1996756X.

35 CULSHAW, B. The optical fibre sagnac interferometer: An overview of its principles and applications. In: . [S.l.]: Institute of Physics Publishing, 2006. v. 17. ISSN 13616501.

36 MOELLER, R. P.; BURNS, W. K. 1.06-m all-fiber gyroscope with noise subtraction. **Opt. Lett.**, Optica Publishing Group, v. 16, p. 1902–1904, 12 1991. Disponível em: <https://opg.optica.org/ol/abstract.cfm?URI=ol-16-23-1902>.

37 GUATTARI, F.; CHOUVIN, S.; MOLUçON, C.; LEFèVRE, H. A simple optical technique to compensate for excess rin in a fiber-optic gyroscope. In: . [S.l.: s.n.], 2014. p. 1–14.

38 MORRIS, T. A.; ZAWADA, A. N.; GARCIA, D.; WHEELER, J. M.; DIGONNET, M. J. F. Optimization of the angular random walk in laser-driven fiber-optic gyroscopes. **IEEE Sensors Journal**, v. 22, p. 2205–2212, 2 2022. ISSN 1558-1748.

39 ZHANG, H.; CHEN, X.; SHU, X.; LIU, C. Angular random walk improvement of a fiber-optic gyroscope using an active fiber ring resonator. **Opt. Lett.**, Optica Publishing Group, v. 44, p. 1793–1796, 4 2019. Disponível em: <https://opg.optica.org/ol/abstract.cfm?URI=ol-44-7-1793>.

40 GAO, W.; WANG, Z.; WANG, G.; MIAO, W. Angular random walk improvement of resonator fiber optic gyro by optimizing modulation frequency. **IEEE Photonics Journal**, v. 11, p. 1–13, 2019. Disponível em: <https://api.semanticscholar.org/CorpusID:199058952>.

41 KONG, L.; ZHANG, C.; ZHENG, Y.; CHEN, H. Self-adaptive suppression of the excess relative-intensity-noise in fiber optic gyroscopes. **IEEE Sensors Journal**, Institute of Electrical and Electronics Engineers Inc., 2022. ISSN 15581748.

42 QIN, X.; ZHANG, C.; XU, H.; LI, L.; ZHENG, Y. Angular-random-walk reduction for fiber optic gyroscopes using light-intensity switching. **Journal of Lightwave Technology**, p. 1–12, 2023. ISSN 0733-8724. Disponível em: <https://ieeexplore.ieee.org/document/10256114/>.

43 TEXAS INSTRUMENTS. **4MSPS, 24-Bit Analog-to-Digital Converter datasheet (Rev. D)**. ADS1675 datasheet, Dec. 2008 [Revised Aug. 2010].

44 MEJIA, E.; DUKE, K.; KOMMARAJU, N. **TI Precision Designs: Verified Design ±10V 4-Quadrant Multiplying DAC**. 2013. Disponível em: <www.ti.com>.

45 ZHANG, J.; LI, H.; XIN, J.; ZHU, L. Modeling and simulation of digital closed-loop fiber optic gyroscope based on sigma-delta modulation. In: . [S.l.]: SPIE-Intl Soc Optical Eng, 2023. p. 106. ISBN 9781510663312. ISSN 1996756X.

46 KARKI, J. **Analysis of fully differential amplifiers**. 2000.

47 RENESAS, I. **Understanding Noise in the Signal Chain**. 2017.

48 LIZON, B. **Fundamentals of Precision ADC Noise Analysis**. 2020.

49 SHIN, S.; SHARMA, U.; TU, H.; JUNG, W.; BOPPART, S. A. Characterization and analysis of relative intensity noise in broadband optical sources for optical coherence tomography. **IEEE Photonics Technology Letters**, v. 22, n. 14, p. 1057–1059, 2010.

50 DOLLEVEDO, G. A. **IFOG Noise-to-ARW Simulation App**. [S.l.]: GitHub, 2023. <https://github.com/GiacomoAD/IFOG-noise-to-arw.git>.

APPENDIX A – MODULATOR DRIVER GAIN ADJUSTMENT

Adjusting the modulator driving circuit gain is essential to optimize the modulation span of the IFOG, as well as to ensure the circuit will be able to output the minimum voltage required by the employed modulation technique. Therefore, in this appendix, we will discuss this adjustment procedure, both in hardware and firmware, that the two-level two-stage modulation scheme (which is the employed technique of the developed IFOG) requires. However, the following discussion should be enough to enable the setup for any other technique.

A.1 Required Voltage Span

First of all, it is important to notice that the modulation span is tied to the MIOC half-wave voltage. The voltage produced by the circuit will be converted to phase-shift following the expression:

$$\Delta\phi = \frac{V_M \cdot \pi}{V_\pi}, \tag{A.1}$$

where V_M is the output voltage (in V) produced by the modulator, V_π is the MIOC half-wave voltage (in V/π rad), and $\Delta\phi$ is the resulting phase-shift in radians. Through Equation A.1, one can see how the total modulation span, in radians, is, in practice, limited by the driver output voltage.

Considering the IFOG operating in closed-loop mode, it is ideal to get the highest possible output voltage from the modulation circuit driver. This is because a higher voltage span (and thus a higher modulation span) allows for higher speed assessment, as 2π resets should take longer to happen; and frequent resets can increase the output noise (Section 2.2.1).

When taking the modulation technique into account, there is a minimum voltage span that is necessary in order to enable its application. In particular, the developed IFOG employs a two-level two-stage modulation scheme [15], meaning that the driving circuit needs to be able to produce a minimum voltage that corresponds to a phase-shift of $2\pi - \phi_M$ radians (where ϕ_M is the modulation depth) in open-loop operation. In closed-loop operation, the reset has to be taken into account, therefore, the total minimum voltage should correspond to:

$$V_{min} = V(2\pi - \phi_M) + V(2\pi) \quad [V], \tag{A.2}$$

where $V(\phi)$ is the voltage that corresponds to a phase-shift of ϕ.

Particularly, in the developed IFOG, the voltage output is given through a differential driver, and the optimal modulation depth is around $150°$. Hence, the output is better described as:

$$V_{min} = \pm \frac{V(210°) + V(360°)}{2} \quad [V]. \tag{A.3}$$

Finally, taking into account that the employed MIOC V_π is 3.54 V, and by combining equations A.3 and A.1, our driver has to be able to output a minimum voltage of ± 5.6 V.

Next, the modulation circuit equations will be briefly discussed along with the gain adjustment procedure.

A.2 Modulation Circuit Equations

The whole modulation circuit is based on two digital-to-analog converters: a 20-bit DAC and a 16-bit DAC. The former is used to enable a fine output voltage adjustment by controlling the reference voltage input of the 16-bit DA, and it is mainly responsible for the "2π" control loop. The latter is responsible for setting the modulation depth and managing its control loop.

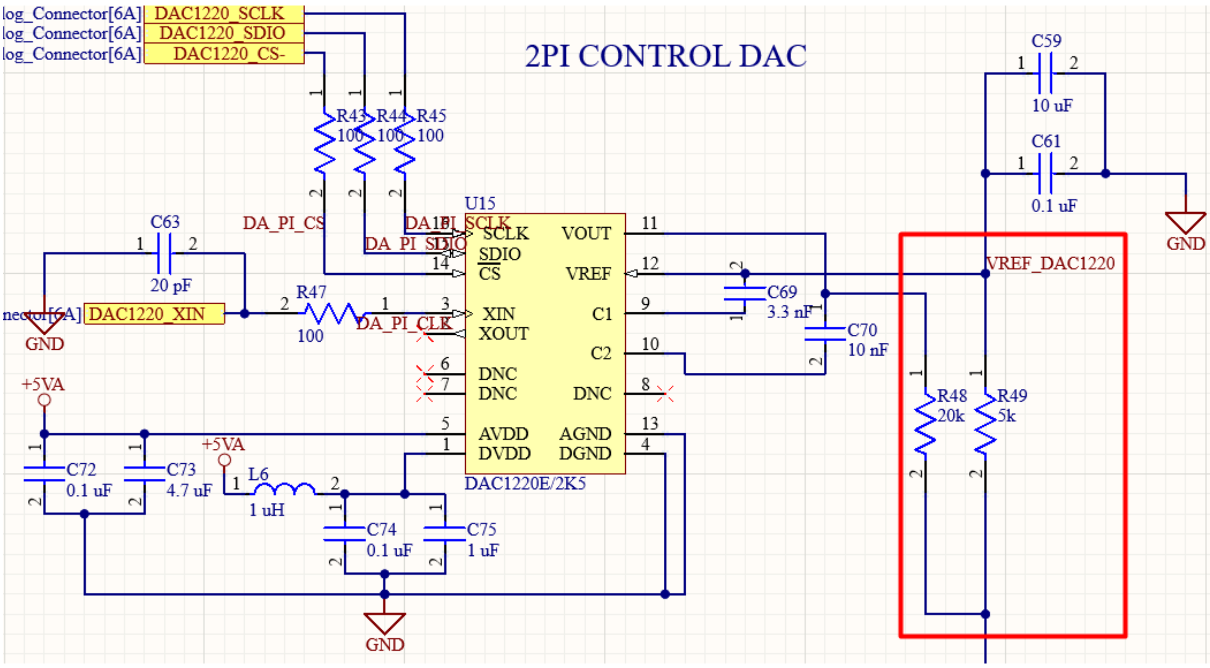

Figure A.1 – 2 Pi Control 20-bit DAC circuit schematic. The red rectangle highlights the output section of the DAC.

Figure A.1 depicts the 20-bit DAC circuit schematic. It was designed to enable a 1 V voltage span control between 2 and 3 V at the output. This can be found by solving Kirchhoff's

Current Law for R48 and R49, knowing that its ends are connected to an op-amp (acting as a buffer) input, as;

$$\frac{V_{R48}}{4R} = -\frac{V_{R49}}{R} \quad => \quad V_{R48} = 4V_{R49}. \tag{A.4}$$

Here, V_{R48} is equal to the difference between DAC1220 V_{out} ($0 \leq V_{out} \leq 5$ V in the developed circuit) and the voltage V at the buffer input (therefore the 16-bit DAC V_{REF16} input); V_{R49} is equal to the difference between DAC1220 V_{REF20} (2.5 V in the developed circuit), and the voltage at the buffer input V. Therefore, using equation A.4, the voltage at the buffer input V is described by:

$$V_{REF16} = V = 2 + \frac{V_{out}}{5}, \quad 0 \leq V_{out} \leq 5 \tag{A.5}$$

Next, the 16-bit DAC (AD5543) circuit is designed to output a voltage that spans from $-V_{REF16} \leq V \leq V_{REF16}$ V, and this output voltage is fed through a fully-differential amplifier with a gain stage. This final gain stage is depicted in Figure A.2, where the gain is set by the combination of resistors R_{50} and R_{52} on the inverting input branch and, symmetrically, resistors R_{63} and R_{56} on the non-inverting input branch. The gain Av is described by:

$$Av = \frac{R_{50}}{R_{52}} = \frac{R_{63}}{R_{56}}. \tag{A.6}$$

In the circuit depicted in Figure A.2, the Av is equal to $2.\overline{333}$. Also, V_{REF16} maximum value is equal to 3 V. This means that the theoretical maximum output of the driver, under these conditions, is approximately 7 V.

Finally, having discussed the circuits involved in generating the MIOC driving voltage, the gain setting procedure will be discussed in the next section.

A.3 Gain Setting Procedure

To ensure proper gain setting, one should adjust the final stage resistors in order to provide the widest voltage span at the output according to the employed fully-differential driver. In the developed IFOG, the employed op-amp is the LMP8350, capable of outputting a voltage of around 9 V when supplied with ± 5 V. This means the theoretical gain can be further increased in respect to the ones shown at the circuit design schematic.

The first step to correctly set the gain is to ensure the 20-bit DAC is outputting its maximum value. This can be done via firmware, by writing the value that corresponds to 0xFFFFF through the SPI bus. 16-bit DAC reference voltage (V_{REF16}) should be now set to its maximum value.

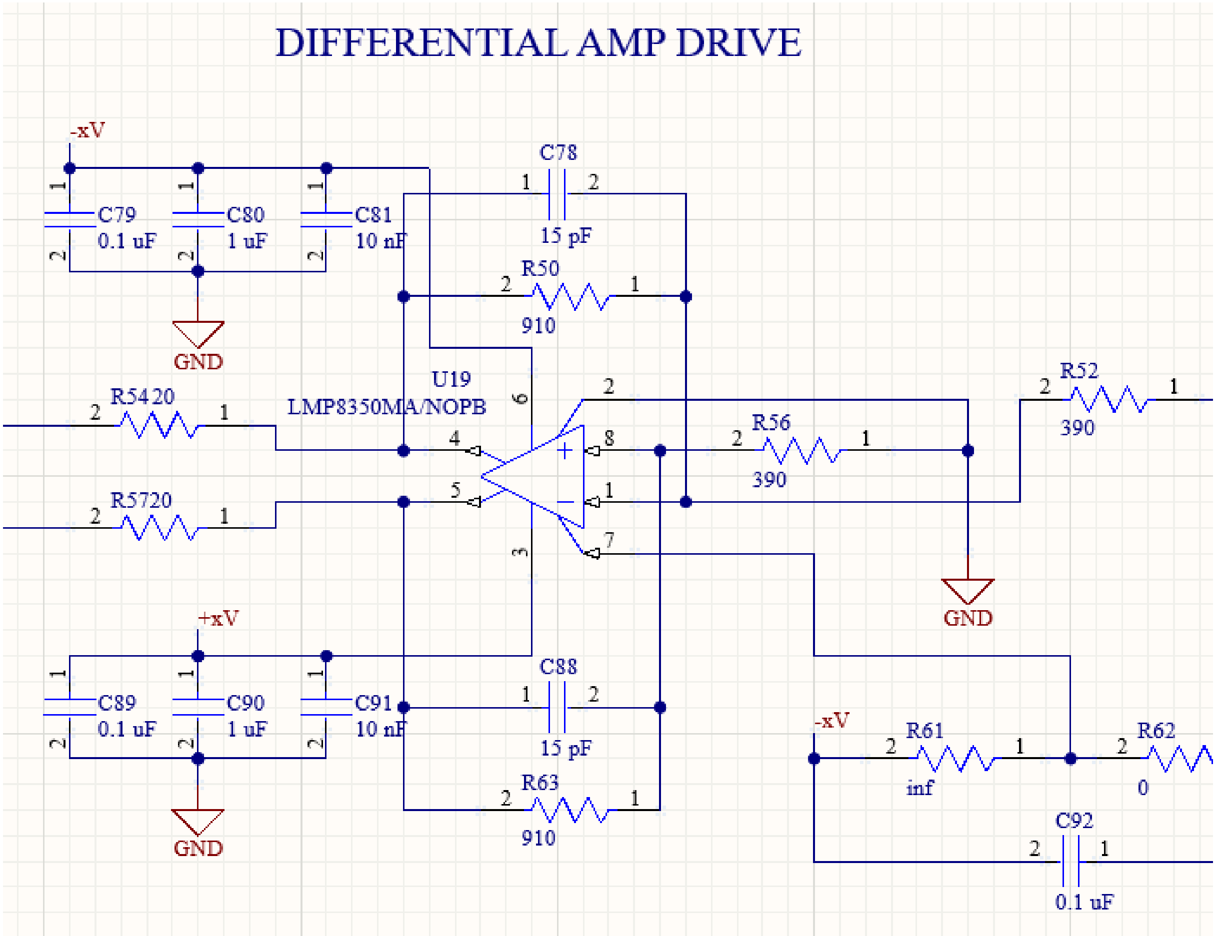

Figure A.2 – MIOC Driver final gain stage through a fully-differential amplifier.

Then, the maximum value should be written to the 16-bit DAC as well, through another SPI write with the value of 0XFFFF. With both DACs at their maximum output setting, one can start adjusting the final stage gain resistor values in order to reach the maximum output voltage of the driver.

Finally, with the maximum gain set on hardware, the firmware must be adjusted to ensure proper writing to the phase modulator. In order to do this, the 20-bit DAC is set to half of its maximum output by writing the value of 0x7FFFF via SPI bus. Then, the 16-bit DAC should be set to both its maximum (0xFFFF) and mininum (0x0) value, and the driver output voltage must be recorded for both cases. At last, at the firmware, the sum of both of these values is used as the DAC voltage limit along with the MIOC half-wave voltage in order to find the conversion between the desired phase modulation value and digital write value to the DAC.

APPENDIX B – INTERACTIVE NOISE MODEL

In this appendix, we will briefly present an interactive noise model application that computes the overall system electronic and optical noise, as well as the noise-to-ARW conversion, following the model proposed by Bacurau in [15] and discussed in Chapter 4. The idea of this application is to serve both as a didactic tool, enabling an easy and visual representation of how each noise source alters the gyroscope performance, and as an auxiliary tool in order to make small adjustments in our noise model. Figure B.1 shows the application interface.

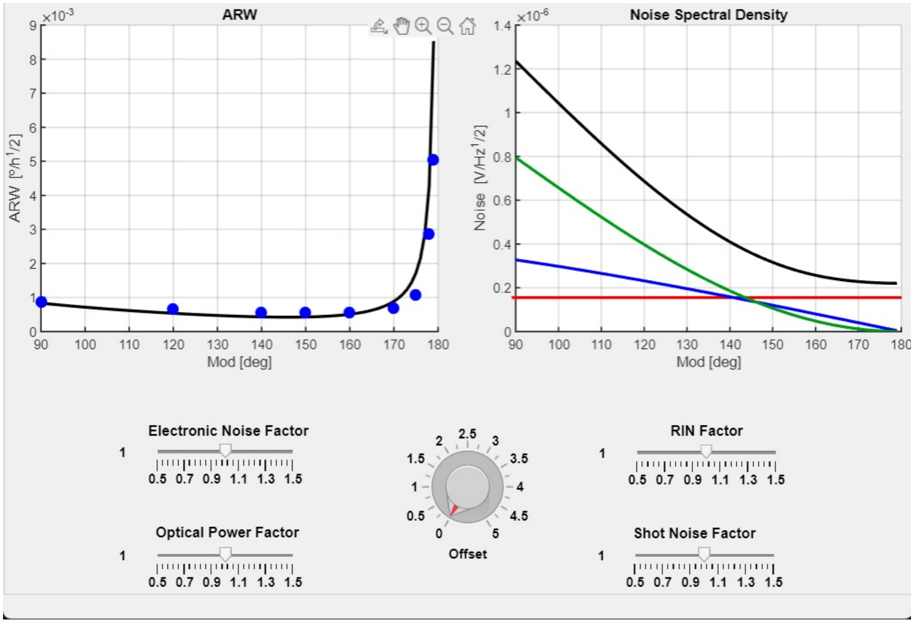

Figure B.1 – Interactive noise model application user interface.

The current version of the application enables the user to increase (or decrease) a multiplying factor that changes the values of the electronic noise (red line), the optical RIN (green line), and the optical shot noise (blue line). The optical source power can also be increased or decreased by a multiplying factor. Finally, our experimental ARW data is also displayed in the ARW plot as blue dots, and this data can also be corrected with an x-axis (modulation depth) offset factor.

This tool can be found at [50] as a standalone Windows application.

ANNEX A – ANALOG BOARD ELECTRONIC SCHEMATIC

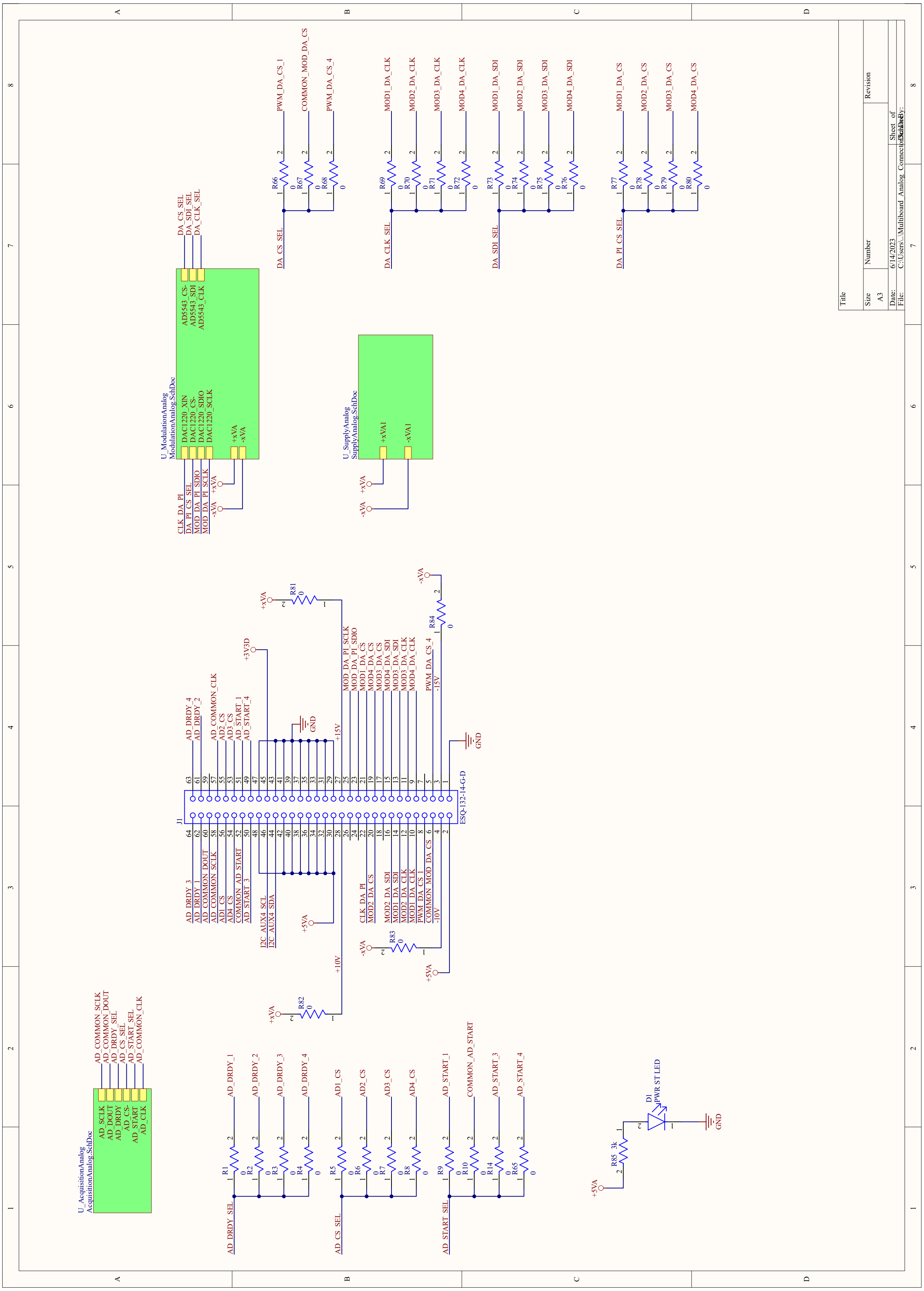
U_AcquisitionAnalog
AcquisitionAnalog.SchDoc
U_ModulationAnalog
ModulationAnalog.SchDoc
U_SupplyAnalog
SupplyAnalog.SchDoc
J1
ESQ-132-14-G-D
AD_DRDY_SEL
AD_CS_SEL
AD_START_SEL
DA_CS_SEL
DA_CLK_SEL
DA_SDI_SEL
DA_PI_CS_SEL
GND
+5VA
+xVA
-xVA
+3V3D
D1
PWR ST LED
Title
Size
A3
Number
Revision
Date:
6/14/2023
File:
Sheet of
Drawn By:

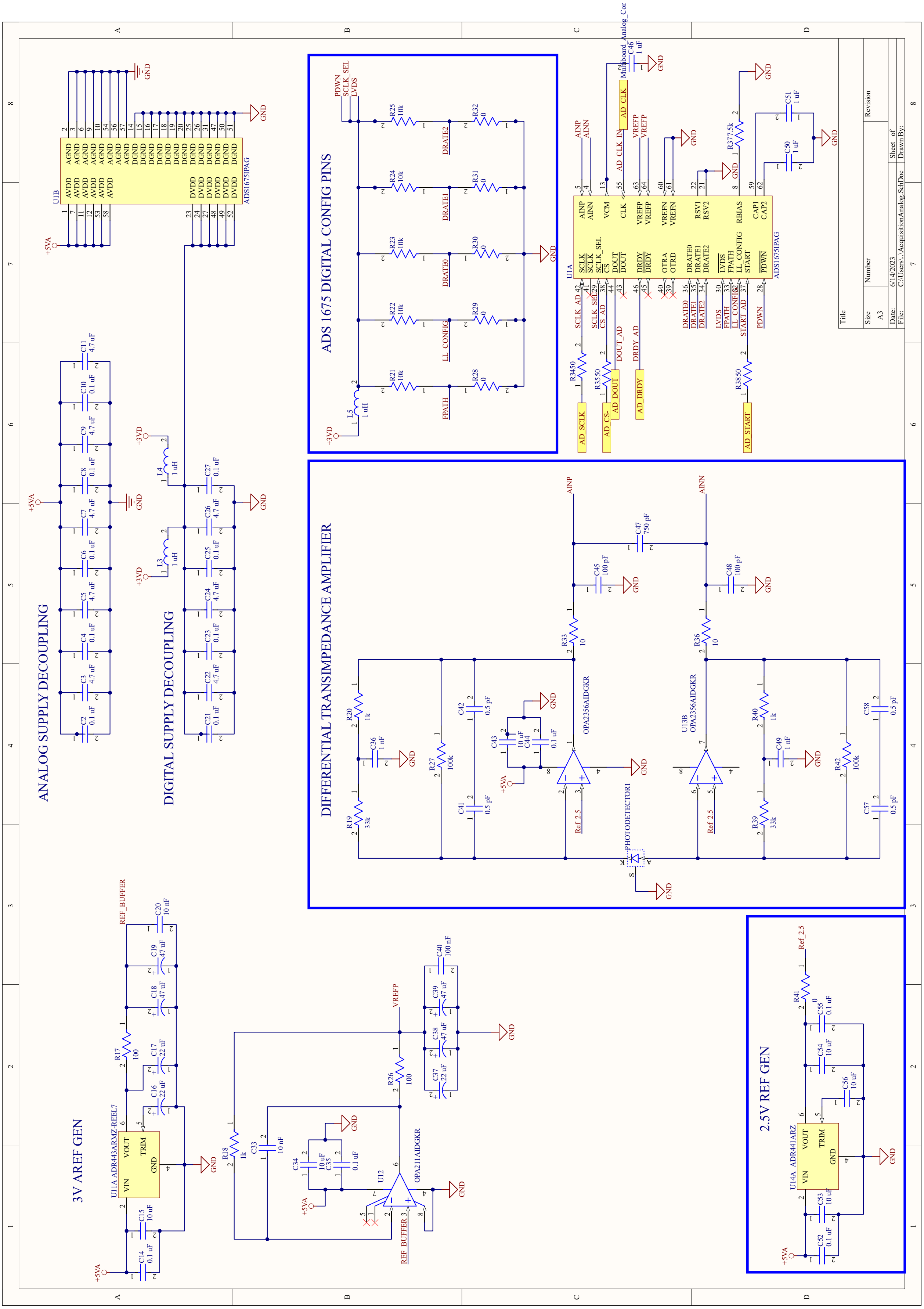
ANALOG SUPPLY DECOUPLING
DIGITAL SUPPLY DECOUPLING
ADS 1675 DIGITAL CONFIG PINS
DIFFERENTIAL TRANSIMPEDANCE AMPLIFIER
3V AREF GEN
2.5V REF GEN
U1B
ADS1675IPAG
U1A
OPA2356AIDGKR
PHOTODETECTOR1
U11A ADR443ARMZ-REEL7
OPA211AIDGKR
U14A ADR441ARZ
Title
Size
A3
Number
Revision
Date:
6/14/2023
File:
C:\Users\..\AcquisitionAnalog.SchDoc
Sheet of
Drawn By:

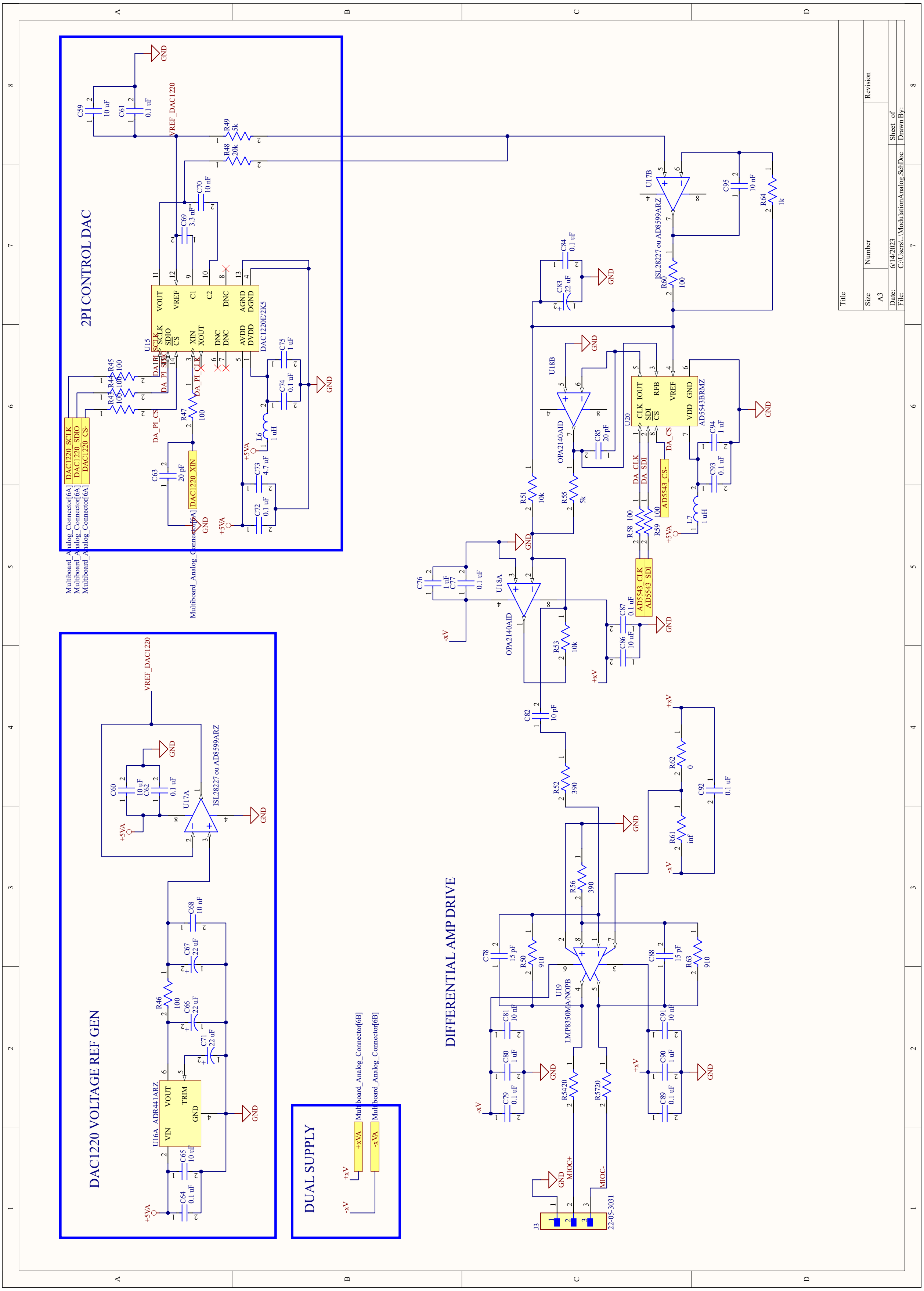
2PI CONTROL DAC
DAC1220 VOLTAGE REF GEN
DUAL SUPPLY
DIFFERENTIAL AMP DRIVE
DAC1220E/2K5
AD5543BRMZ
OPA2140AID
ISL28227 ou AD8599ARZ
LMP8350MA/NOPB
U16A ADR441ARZ
22-05-3031
Title
Size
A3
Number
Revision
Date: 6/14/2023
File: C:\Users\..\ModulationAnalog.SchDoc
Sheet of
Drawn By:

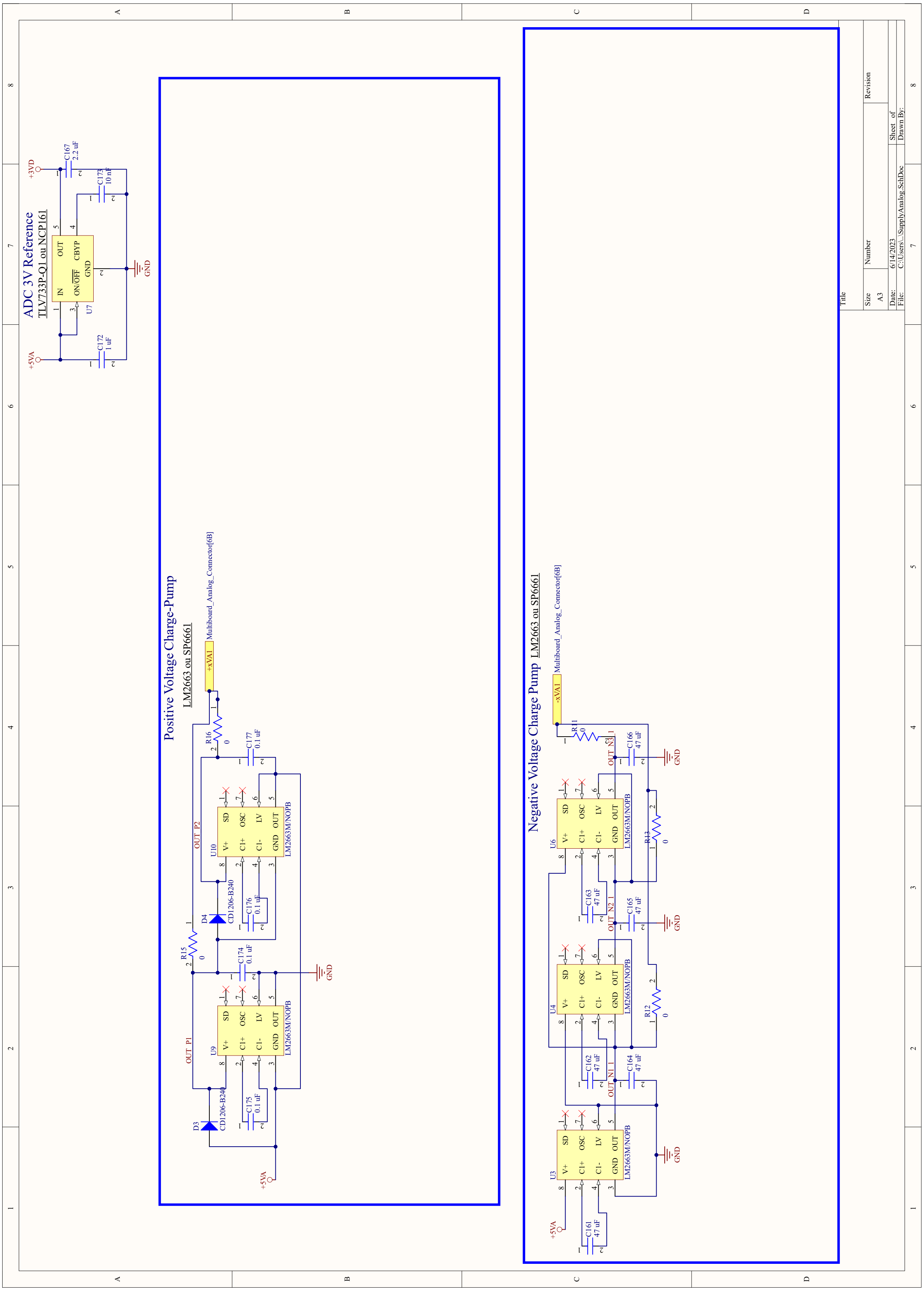
ADC 3V Reference
TLV733P-Q1 ou NCP161
Positive Voltage Charge-Pump
LM2663 ou SP6661
Multiboard_Analog_Connector[6B]
Negative Voltage Charge Pump
LM2663 ou SP6661
Multiboard_Analog_Connector[6B]
Title
Size
A3
Number
Revision
Date: 6/14/2023
File: C:\Users\..\SupplyAnalog.SchDoc
Sheet of
Drawn By:

ANNEX B – DIGITAL BOARD ELECTRONIC SCHEMATIC

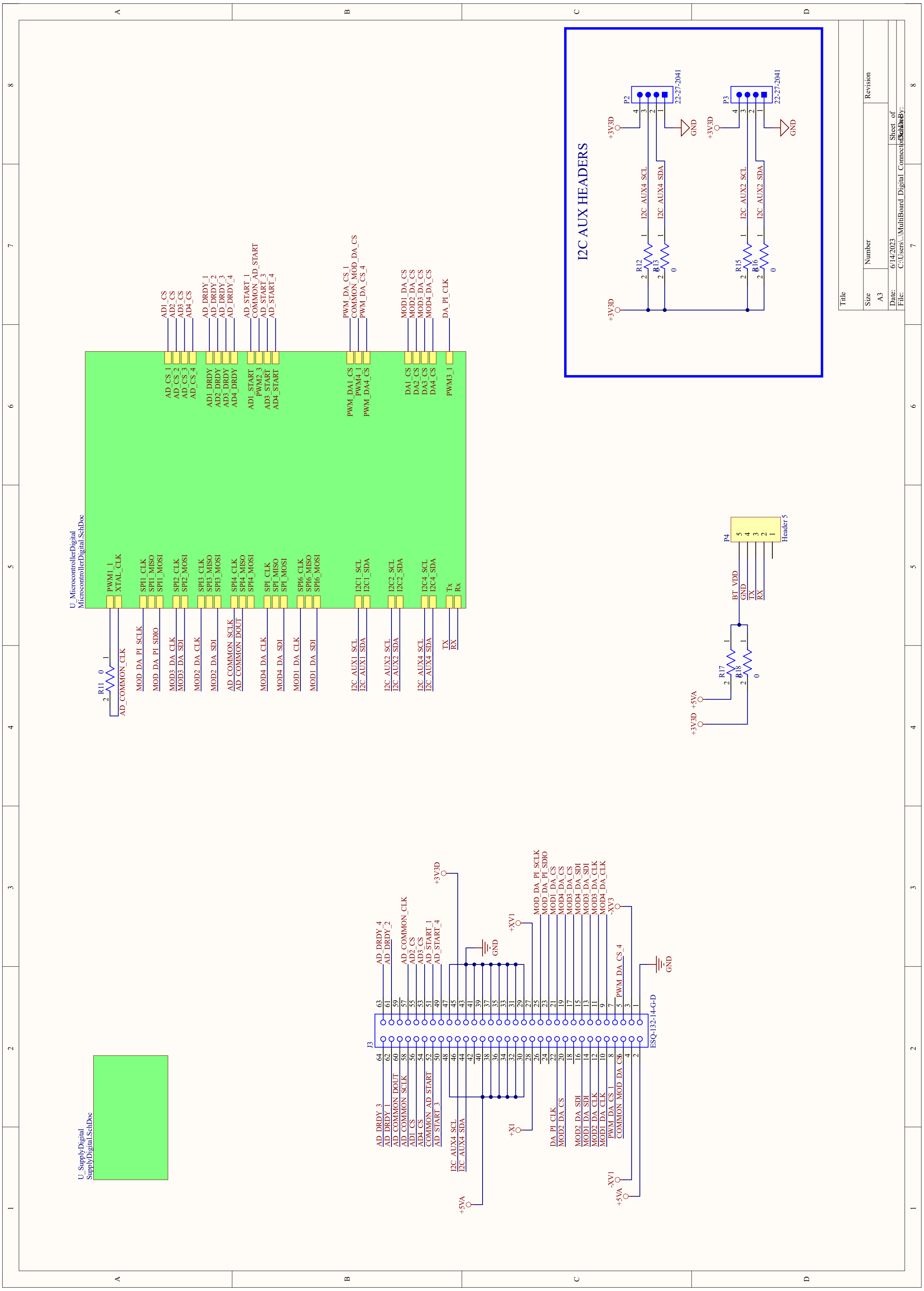
I2C AUX HEADERS
U_MicrocontrollerDigital
MicrocontrollerDigital.SchDoc
U_SupplyDigital
SupplyDigital.SchDoc
P2
22-27-2041
P3
22-27-2041
P4
Header 5
J3
ESQ-132-14-G-D
R11
R12
R13
R15
R16
R17
R18
+3V3D
+5VA
GND
+XV1
-XV1
+X1
-XV3
I2C_AUX4_SCL
I2C_AUX4_SDA
I2C_AUX2_SCL
I2C_AUX2_SDA
BT_VDD
GND
TX
RX
AD_COMMON_CLK
PWM1_1
XTAL_CLK
Title
Size
A3
Number
Revision
Date:
6/14/2023
Sheet of
File:
Drawn By:

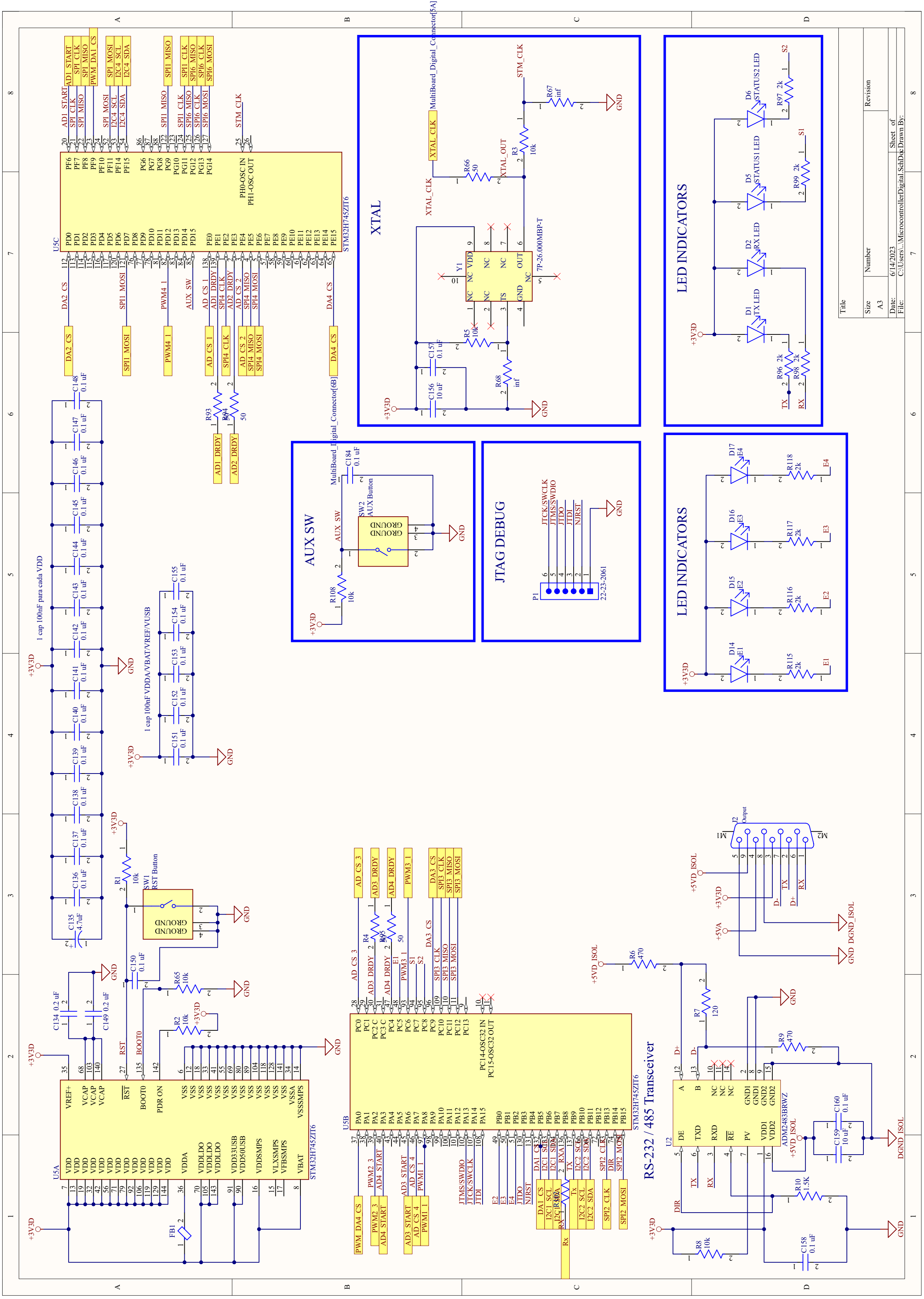
XTAL
AUX SW
JTAG DEBUG
LED INDICATORS
LED INDICATORS
RS-232 / 485 Transceiver
STM32H745ZIT6
1 cap 100nF para cada VDD
1 cap 100nF VDDA/VBAT/VREF/VUSB
Title
Size
A3
Number
Revision
Date: 6/14/2023
File: C:\Users\..\MicrocontrollerDigital.SchDoc
Sheet of
Drawn By:

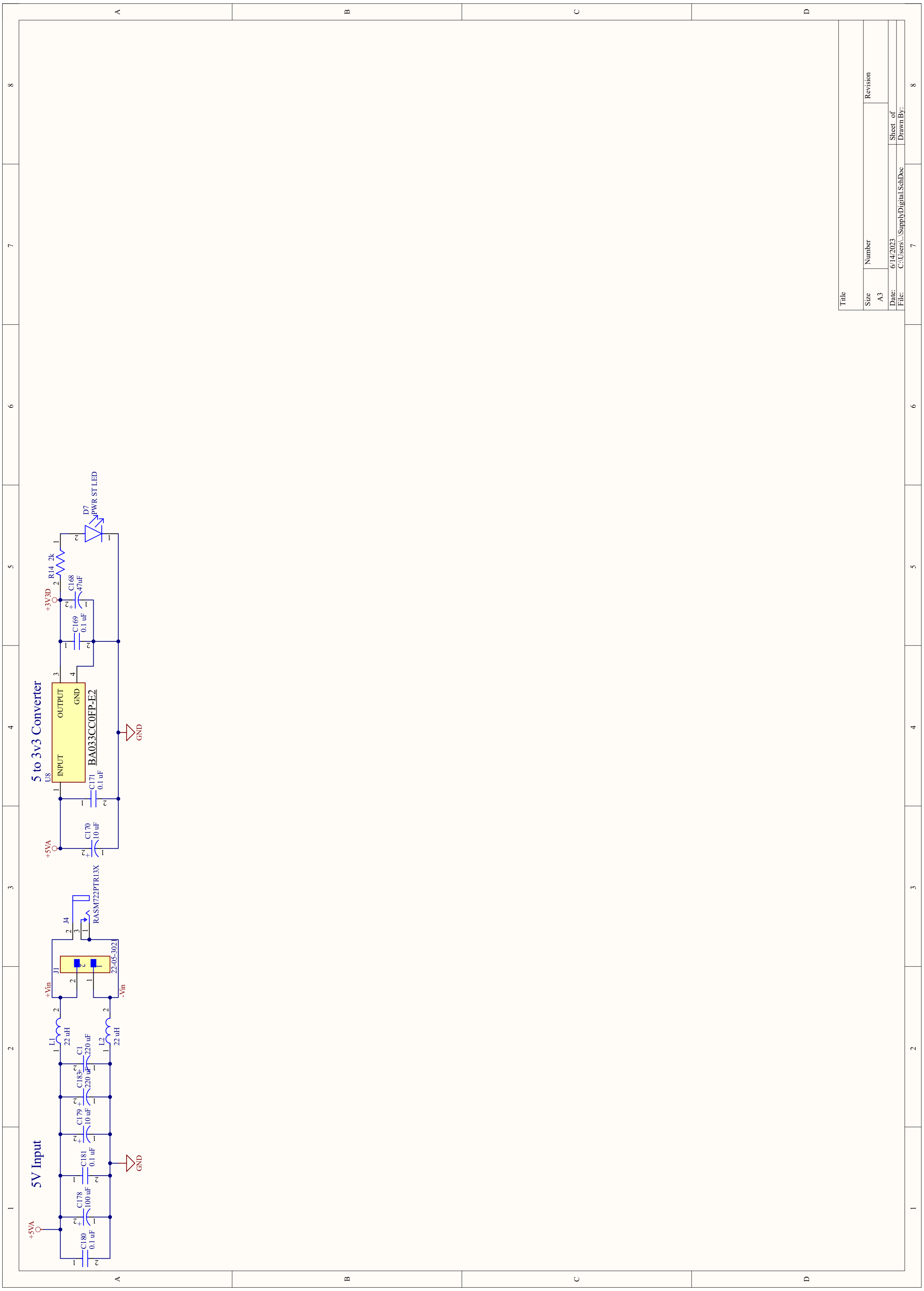
5V Input
5 to 3v3 Converter
+5VA
C180
0.1 uF
C178
100 uF
C181
0.1 uF
C179
10 uF
C183
220 uF
C1
220 uF
L1
22 uH
L2
22 uH
GND
+Vin
-Vin
J1
22-05-3021
J4
RASM722PTR13X
C170
10 uF
C171
0.1 uF
U8
INPUT
OUTPUT
GND
BA033CC0FP-E2
C169
0.1 uF
C168
47uF
+3V3D
R14 2k
D7
PWR ST LED
Title
Size
A3
Number
Revision
Date:
6/14/2023
Sheet of
File:
C:\Users\..\SupplyDigital.SchDoc
Drawn By: